# 1 Introduction

The terahertz (THz) frequency band of 100 GHz up to several THz is located in between the well explored optical frequencies and the microwave or millimeter wave band. Despite increasing research efforts over the last two decades, THz sensing and spectrometer systems are far from being robust and cost effective. This lack of miniaturization is mostly due to bulky laser systems driving these optically generated THz systems. Electronic generation forms like GaAs mixers or GUNN diodes are more compact and smaller in size. However, efficient generation is only possible for the lower THz window.

Sources for higher THz frequencies are spacious far infrared gas lasers or quantum cascade lasers (QCLs), which work best for frequencies at the top end of the THz window (10 THz and above). One of the more versatile techniques to generate pulsed or continuous wave (CW) THz is the use of photoconductive switches (antennas). Optically exciting the gap region of these structures allows for inducing a short current pulse or for the modulation of the electrical current within the antenna of a CW spectrometer. This abrupt or periodic change in current flow emits electromagnetic waves in the THz frequency range. Both generation principles have been studied and investigated thoroughly over the last twenty-five years.

Yet, the development of passive devices for THz applications like waveguides, filters, reflectors and modulators is just in the beginning of being established. Mirrors made out of different kinds of metals, ceramics or different polymers have been analyzed for THz characteristics. Frequency selective surfaces have also been proposed for narrow band mirror designs. Solutions of guiding THz radiation with low loss and negligible dispersion have been based on their counterparts in RF electronics as well as in the optical world. Examples of these cross-over designs are metal planar waveguides which have been demonstrated in various designs, as well as thin metal or polymer wires have been proposed as guiding schemes.

All metallic waveguides rely on propagation of the electrical field through the surrounding matter, which is air in most of the cases. This means that the metallic structure only provides fixed guiding boundaries and is therefore per definition weakly guiding with a low confinement factor. Another downside is the resulting high bending loss through such weak guiding waveguides. Thus, for proper guiding and the ability to tailor the dispersion and confinement, an index guiding scheme is necessary. Polymer based fibers are a perfect alternative for THz waveguiding due to their potential mass production capability and their low absorption in the THz frequencies. In this work, polymer based THz filter and fiber designs are discussed and characterized in detail.

The intended direction of this work was to build up dual or multi-wavelength fiber lasers as a source for continuous wave THz systems based on photomixing. For this

purpose I started writing standard and sampled optical Bragg gratings in telecommunication glass fibers. By using the point-by-point inscription method, the introduction of any arbitrary pattern of refractive index changes into the core was possible. Thus, novel phase-shifted sampled Bragg gratings were written at Macquarie University in order to achieve dual wavelength fiber laser operation [1]. This technique was extended by myself in the polymer fiber regime as well; proving that multi-photon absorption is a powerful tool to induce refractive index modifications in nearly all relevant optical transparent materials [2]. After joining Martin Koch's group, one targeted intension was to further adapt this technique to form THz Bragg gratings in polymer THz fibers. In cooperation with our colleagues at the Danish Technical University (DTU Fotonik) who provided standard THz fibers, several ideas of locally modulating the refractive indexes in microstructured THz fibers were explored: Continuous wave and pulsed ultraviolet (UV) exposure through a metal mask, multi-photon excitation with a line focus scanned in transverse direction through the fiber or even high-power defocused spherical excitation. However, due to the low induced effective refractive index change, the low permitted number of grating periods and undesired coupling to higher order modes, none of these approaches did render any viable results. In the following, a scheme of near field imaging was set up in Marburg to determine electrical field distributions within THz fibers [3]. Simultaneously a new way of fabricating polymer THz filters was investigated and designs were fabricated by me at the facilities at the University of Sydney and Danish Technical University accordingly. This work contributes to the field of THz science and technology by introducing novel polymer filter structures and a new design of THz fibers. These passive devices are both fabricated by using a fiber drawing technique to scale down inscribed patterns in polymer to THz wavelengths.

Moreover, the revolutionary quasi time domain spectrometer (QTDS) approach is further extended by proving its imaging applicability and new system designs by Maik Scheller and me. In the course of that a hybrid continuous wave spectrometer was set up and characterized by myself. Expanding a standard QTDS system with additional continuous wave multimode laser diode with a slightly different center frequency allows for generating tunable inter-diode mixing frequency in the THz range. This novel approach has major potential to accustom various sensing applications.

This thesis is structured in four chapters. Chapter two lays out the fundamentals of THz generation and detection along with the introduction of state-of-the-art THz systems for common time domain spectrometer (TDS) systems and CW spectrometers. The generation and detection principles are discussed in detail and typical system designs are presented.

In the third chapter, the fabrication and design process of polymer photonic crystal THz waveguides is presented. Also, the fiber drawing method which is used for fabricating the novel THz filters presented in chapter four is explained in detail. I developed an

adapted near-field THz TDS system to verify the THz mode field distributions within polymer THz fibers, which are first derived by simulations. In addition, a new approach for improving the confinement and stripping of undesired higher order modes is demonstrated.

Chapter four presents a new polymer filter structure designed by me. The fabrication process scales down inscribed features in a polymer preform by fiber drawing. Thus, it is possible to obtain hole diameters of 200 µm and below, which could not be fabricated by standard mechanical means. The structures are first simulated in collaboration between myself and M. Ahmadi-Boroujeni with the Generalized Multipole Technique (GMT). In a second step, the novel devices are analyzed by a standard pulsed THz TDS system

The last chapter revolves around the novel quasi time-domain spectrometer approach. This CW based generation and detection scheme is presented [4]. I developed in cooperation with the author, a hybrid THz spectrometer and demonstrated general imaging capability [5-7]. A second system approach with an additional multimode laser diode – a dual QTDS spectrometer - is set up by myself, demonstrating that QTDS has the potential for customized low-cost and robust THz systems.

In the last part of my thesis the new results, like first time realization of fiber drawn THz polymer filters, near-field images of novel THz fiber concepts and improved quasi time-domain THz spectrometers are summarized briefly. A detailed list of publications and my personal contributions in co-author papers are given.

# 2 Fundamentals of THz Time Domain and Continuous Wave Systems

The terahertz (THz) gap, sitting between 0.1 and 10 THz, attracted a lot of interest over the last two decades. Beforehand, the atmosphere's opacity to THz radiation and the high absorption in air kept back the incentive to develop sensitive detectors and high-performance emitters for that frequency range. It wasn't until 1984 when Auston et al. [8] demonstrated the first operational pulsed THz system transmitting through air. After that, the development of THz time-domain spectrometers gained momentum mainly due to the fact that femtosecond Ti:Sapphire lasers as generation source for THz waves were developed and became commercially available in the early 90's. These powerful and very stable femtosecond lasers became a versatile tool for analyzing and inspecting numerous materials by THz radiation. With the first imaging system, realized in 1995 by Hu et al. [9], THz technology was on the edge of stepping into real world environments. The enormous potential of THz radiation became apparent over the last decade in many industrial applications like polymer testing [10, 11], quality control for the paper and food industry [12, 13], as well as for safety and security screening [14].

In the mid 90's another optical method of THz generation followed the pulsed systems – the continuous wave spectrometers [15, 16]. These THz systems are based on optical mixing of two laser beams with slightly different emission wavelengths. The so called difference frequency generation (DFG) between two laser lines can be performed inside a nonlinear crystal or in a photoconductive semiconductor. By tuning the two frequencies in respect to each other the radiated THz emission can be adjusted freely.

Both principles are presented and discussed in the following chapter, including the fundamentals of photoconductive semiconductor antennas in a separate subchapter, which are used in all THz systems throughout this thesis.

## 2.1 Terahertz Time Domain Spectroscopy

The principle of a standard time-domain spectrometer is based on the emission and detection of short THz pulses. Typically, these pulses are generated by ultrashort ($10^{-13}$ sec) optical excitation of either a nonlinear crystal for optical rectification, a semiconductor in surface emitter configuration or a photoconductive antenna. The latter method convinces with its easy handling and is used in the majority of THz spectrometers. The semiconductor material used for photoconductive antennas needs to have a shorter carrier life time, which is important for detecting THz radiation, but is also favorable for generating a broadband THz signal. As long as photo carriers are present the incoming electrical THz field induces shift currents, resulting in an average value of the THz field. The shorter the carrier life times the higher the temporal

resolution of the detected THz-induced currents. Typically, low temperature grown gallium arsenide (LT-GaAs) is used as the substrate material for antennas excited by 800 nm lasers, due to its superior carrier capture time. The electrodes and the antenna structures are fabricated on top of the substrate by metal deposition. The typical antenna design comprises a stripline structure [17], but also known are bowtie, dipole(H-structure), log-spiral [15] or log-periodic [18] structures (cf. Figure 1).

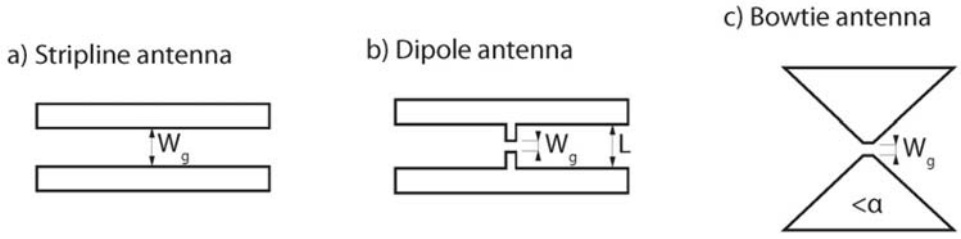


**Figure 1: Antenna structures: a) stripline, b) dipole structure and c) bowtie structure.**

The focused optical excitation generates electron-hole pairs within the photosensitive gap, which are then separated by an applied bias voltage. This carrier acceleration in the associated electric field, to which almost solely electrons contribute, leads to a burst of electric current and hence, an electromagnetic transient is radiated. This picoseconds long radiation contains a plethora of frequency components, ranging up to a few THz. The radiated electric field is proportional to the time derivative of the induced photo current *J(t)*:

$$J(t) = n(t) \cdot e \cdot \mu_e \cdot E_{bias} \tag{2.1}$$

$$E_{THz}(t) \approx \frac{dJ(t)}{dt} \approx \frac{dn(t)}{dt} e\mu_e E_{bias} \tag{2.2}$$

where *n* is the photocarrier density, *e* the electron charge, $\mu_e$ the electron mobility, and $E_{bias}$ the bias electric field. The relation follows the Drude-Lorentz model, which gives the time dependent change in conduction, further described for optically excited, pulsed THz generation by Jepsen et al.[17]. The time dependent change in the carrier density is given by Eq. (2.3), with $\tau_c$as the carrier trapping time and *G(t)* as the intensity dependent carrier generation rate

$$\frac{dn}{dt} = -\frac{n}{\tau_c} + G(t). \tag{2.3}$$

By taking the time dependent average electron velocity *v(t)* into account and the time variant space charge polarization $P_{sc}$[17], one obtains two coupled differential equations(2.3) and (2.5).

$$\frac{dP_{sc}}{dt} = -\frac{P_{sc}}{\tau_r} + nev\,. \tag{2.4}$$

$$\frac{d^2v}{dt^2} + \frac{1}{\tau_s}\frac{dv}{dt} + \frac{ne^2v}{\eta m^* \varepsilon_r} = \frac{eP_{sc}}{\eta m^* \varepsilon_r \tau_r}\,. \tag{2.5}$$

$P_{SC}$ is the space charge polarization induced by the separated electrons and holes, $\tau_r$ is the recombination lifetime, $\tau_s$ is the relaxation time, $v$ the average carrier velocity, $m^*$denotes the effective mass, and $\varepsilon_r$ is the material's permittivity.

| | Value |
|---|---|
| Pulse width | 65 fs |
| $\tau_c$ (trapping lifetime) | 0.6 ps |
| $\tau_r$ (recombination time) | 900 fs |
| $\tau_s$ (scattering lifetime) | 100 fs |
| m* | 9,10 e-23 kg |
| $\varepsilon_r$ | 8,85 e-12 As/Vm |
| η | 0.005 |
| E | 40V/10 µm |

**Table 1: Simulation start values for the Drude-Lorentz analysis[19].**

Solving these equations for LT-GaAs with an optical excitation of 67 fs, a carrier trapping time constant of 0.9 ps and a carrier scattering time of 100 fs, leads to the results presented in Figure 2.

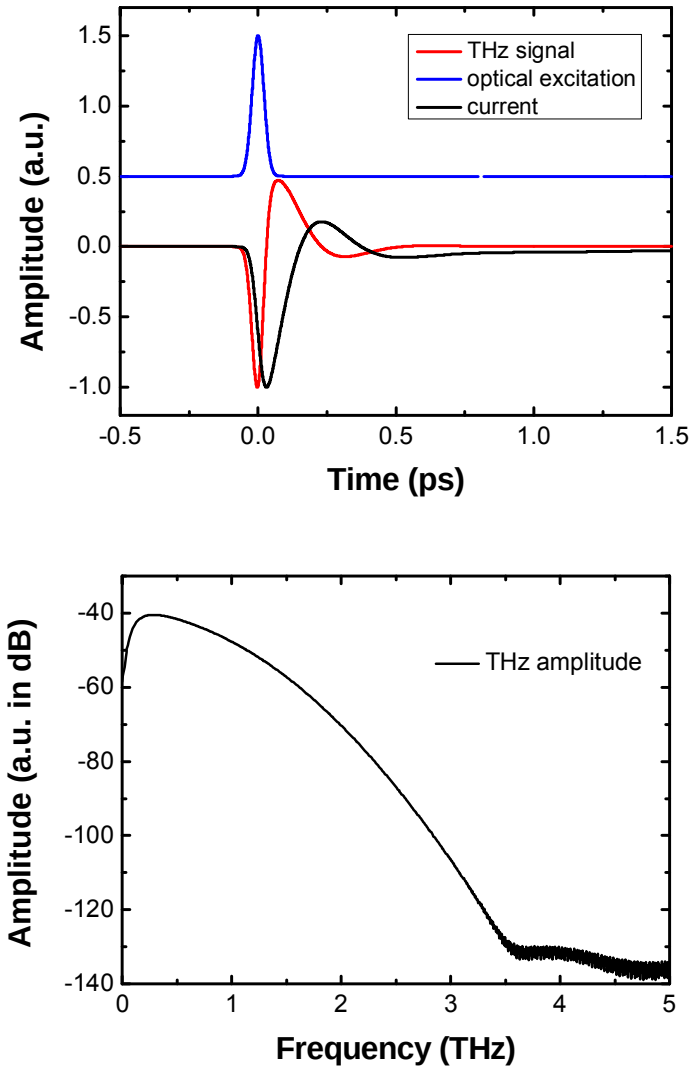


**Figure 2: a) Optical pulse (blue), induced current (black) and the derivative (THz radiation – red). b) Spectrum of the resulting THz pulse.**

The corresponding frequency spectrum of the emitted THz pulse is shown in Figure 2b.

The THz radiation can also be detected with optically sampled photoconductive antennas. The principle for coherent detection is similar to the generation scheme; however, the charge separation is not induced by an applied bias voltage but rather by the incident THz field. Due to the very short carrier trapping times in LT-GaAs, only a fraction of the THz pulse induces a separation of charges and therefore a detectable current in the order of nanoamperes. The flow of current is proportional to the convolution integral of the passing electrical field of the THz pulse $E_{THz}$ and the time dependant carrier density *n(t)* generated by the optical excitation pulse in the detector antenna's gap [20].

$$I_D(\tau) \approx \frac{1}{T}\int_0^T E_{THz}(t) \cdot n(t-\tau)dt. \tag{2.6}$$

With T denoting the laser's pulse repetition time.

Delaying the optical detection pulse in time allows for stepwise scanning through the THz pulse and yields an averaged value of the incident electrical THz field over the carrier life time. The general principle is highlighted in Figure 3.

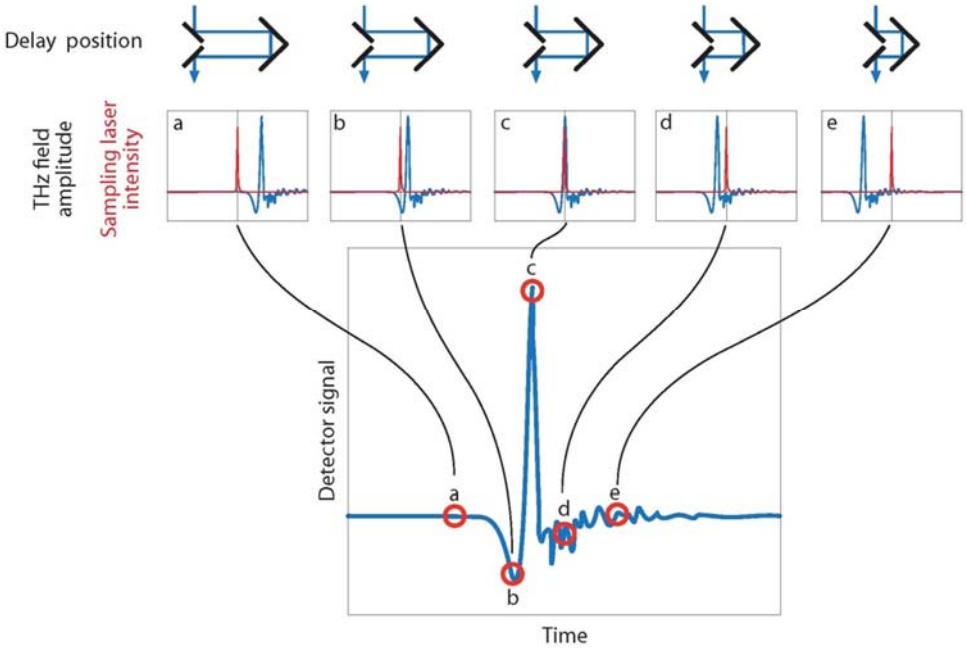


**Figure 3: Principle of coherent THz pulse sampling by delaying the optical detection pulse.**

The optical delay of emitter to detector pulse can be introduced in either optical arm. A schematic of a very simple time domain spectrometer is depicted in Figure 4, with the delay line being realized in the detector arm as a linear adjustable retro mirror. For coherent detection the same laser pulse generating the THz pulse has to be used for sampling. Thus, the path length in the detector arm has to equal the emitter path length plus the THz segment.

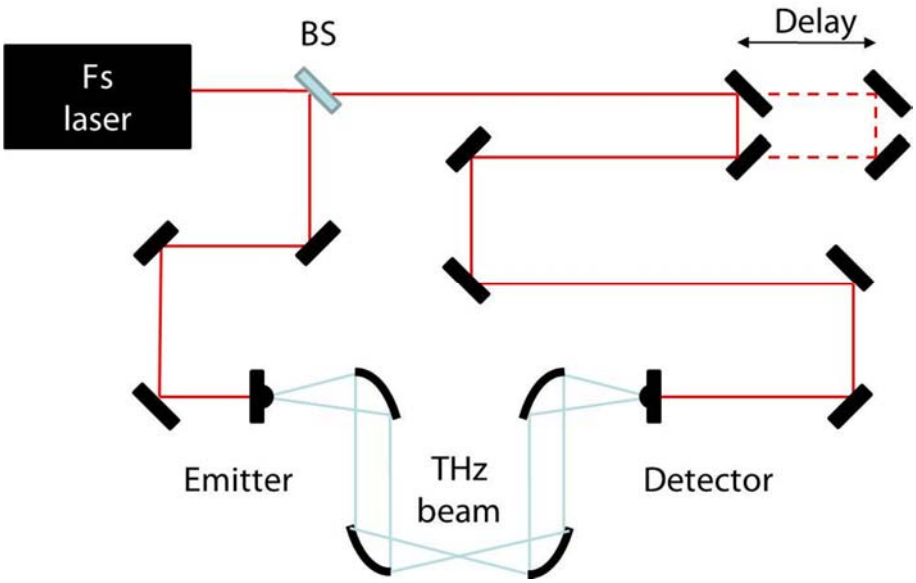


**Figure 4: Standard THz time-domain spectrometer setup.**

The extraction of relevant information on the subject under investigation can all be collected by comparing the sample measurement to a reference scan of the empty system without the sample present. The reference measurement performed right before or after the sample measurement has the advantage of eliminating external influences on the system. Changes in temperature and humidity, as well as decreased laser power or antenna efficiencies won't affect the extracted parameters as they are considered constant between the reference and the sample measurement. The higher refractive index of the sample prolongs the time of flight of the THz pulse and can be extracted by analyzing the time domain data.

For the THz TDS systems reported in this thesis, fiber lasers operating at 1550 nm with 100 fs pulses or a Ti:Sapphire laser emitting femtosecond pulses at 800 nm, see subchapter2.2.2 and 2.2.1, were used to excite photoconductive antennas. A software tool converts the time domain signal by a fast Fourier transformation into the frequency spectrum and evaluates the spectral refractive index and absorption of the sample. Fabry-Perot echo pulses caused by the reflection of the THz pulse at the samples front and backside surfaces can be used to simultaneously determine the thickness of the sample. A more comprehensive look on the analyzing software is given in chapter three.

## 2.2 Terahertz Time Domain Spectrometer

### 2.2.1 Mode-Locked Titanium Sapphire Laser

The heart of this laser system is a titanium doped sapphire ($Al_2O_3$) crystal which acts as the active medium within the cavity. The crystal is pumped by a 5 W diode-pumped neodymium-doped yttrium orthovanadate (Nd:YVO4) laser which operates at 532 nm. Due to the absorption peak of Ti:Sapphire around 500 nm (cf. Figure 5) the crystal performs a relaxation process which leads to a monochromatic continuous wave emission between 670 nm and 1070 nm.

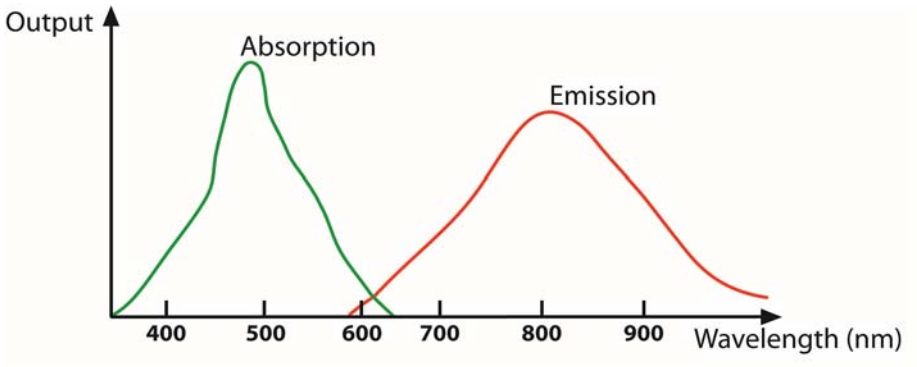


**Figure 5: Absorption and emission spectrum Ti:Sapphire crystal.**

In order to achieve pulsed operation all cavity modes have to be exited synchronously in a fixed phase relationship. This condition is called mode-locked and can be implemented by making use of the Kerr lens effect. High electrical fields induce a local change in refractive index in the crystal due to its nonlinearity. Pulsed radiation therefore gets focused within the crystal (self-focusing) and has a better overlap with the pump laser light. Thus pulsed operation can be favored. Small perturbations can already bring the laser operation from continuous wave into mode-locked pulsing, like a mechanical impulse or an intra-cavity acousto-optical modulator [CJ 93-95]. The cavity length determines the repetition rate of the laser, typically in the order of 50 to 100 MHz.

The Ti:Sapphire laser at Marburg University is a Tsunami model from SpectraPhysics, and offers a typical spectral bandwidth of 60 nm at a central wavelength of 780 nm with 1 Watt average output power. This allows for optical pulses as short as 50 fs. These ultra short pulses have very high intensities and induce next to the regular dispersion in optical components like lenses or waveplates, additional intensity dependent dispersion. This leads to an undesired broadening of the pulses and can be compensated by adding prisms or gratings in the beam path. In this setup a prism compressor is used to negate the first and second order dispersion effect of all optical components in the beam path.

An autocorrelation measurement was used to determine the optimal pulse length right before hitting the THz spectrometer's antennas.

The pre-compensated pulses are split into the two spectrometer arms and guided by optical mirrors to the emitter and receiver antenna (see Figure 4). The THz pulse is guided by four off-axis parabolic mirrors which form a focus spot in the middle. In the detection arm is an additional optical delay line comprising a linear stage with a retro reflector on top. This motorized and computer controlled stepwise sampling of the beam allows for exact retrieval of the THz pulse form. For an optimum signal to noise ratio the Lock-In detection scheme is used. Therefore the emitter antenna's bias voltage is modulated and the modulation frequency is used as the Lock-In's reference. The system's bandwidth stretches out to over 4 THz and offers a signal-to-noise ratio (SNR) of over 50 dB. A time trace and the corresponding spectrum of this system are shown in Figure 6.

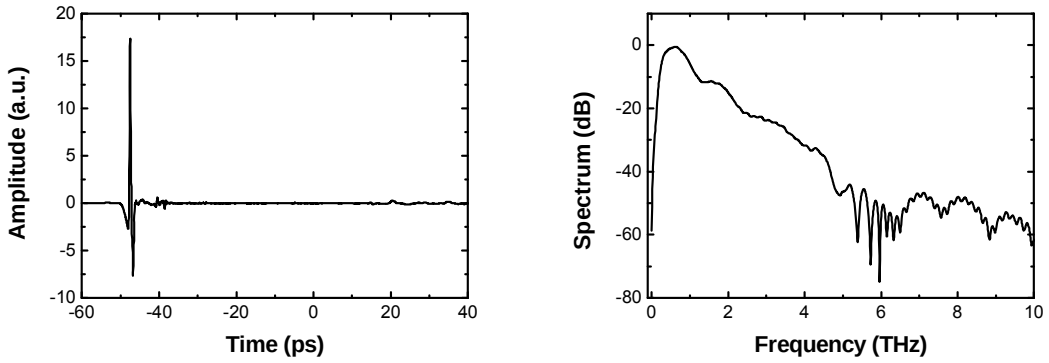


**Figure 6: Time domain signal and frequency spectrum of the Ti:Sapphire TDS system.**

## 2.2.2 THz TDS Based on a Telecommunication Wavelength Fiber Laser System

The measurements presented in this thesis were mainly performed by THz TDS systems driven by femtosecond fiber lasers. The heart of these optical pumped ring lasers builds an erbium ($Er^{3+}$) doped length of fiber as the active gain medium, which emits at the telecommunication wavelength of 1.5 µm. This fact offers the advantage of cheap and reliable components for the THz spectrometer setup. In the last four years, researchers at the Heinrich Hertz Institute in Berlin designed a new stacked InGaAs/InAlAs layer system for photoconductive antennas in the telecommunication wavelength range [21]. In comparison to their LT-GaAs counterparts operating at 800 nm, the high dark current of previous attempts with LT-InGaAs rendered this composition unusable for photoconductive antennas. In the following paragraphs a fiber laser based THz TDS system is presented in detail, special attention is paid to the novel antenna material and its design.

### 2.2.2.1 Erbium Doped Fiber Laser

Fiber lasers have steadily improved since their invention in 1963 [22], to meet nearly every imaginable need, they have the ability to produce high powers, operate in pulsed mode or emit on one or several continuous laser lines. Adjusting the cavity length and introducing a fast switching semiconductor saturable absorber mirror (SESAM), led to an emission of ultrashort optical pulses in the order of hundred femtoseconds [23]. These laser modules have become the state-of-the-art in lasers over the last decade with their size and initial costs decreasing.

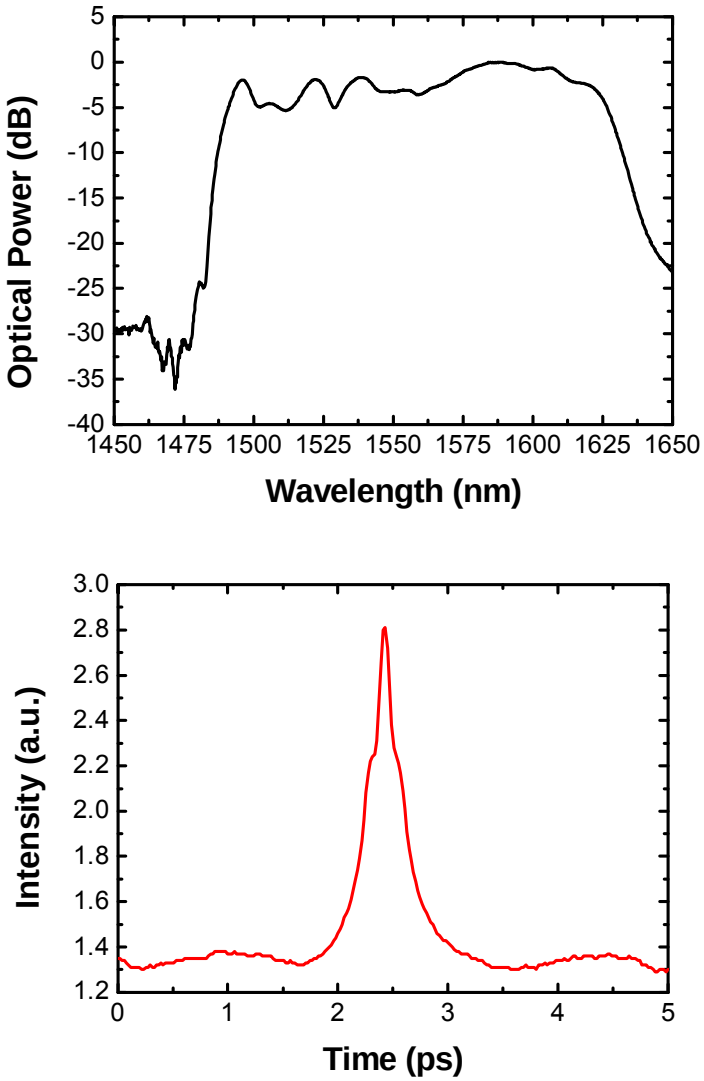


**Figure 7: Optical spectrum and autocorrelation trace of a T-Light femtosecond laser.**

The T-Light from Menlo Systems GmbH is a ring fiber laser, with an operation wavelength at 1550 nm. The erbium ions ($Er^{3+}$) are pumped by 240 mW of 980 nm continuous wave laser diode and the system emits approximately 100 mW at 1550 nm. The laser runs with a repetition rate of 100 MHz and generates sub-100fs laser pulses with a spectral bandwidth of more than 40 nm. An optical spectrum and an

autocorrelation trace can be seen in Figure 7. Fiber lasers are predestined for real world environments and applications due to their very stable operation and easy of handling. Eliminating all free space optical components the coupling into fiber enables all-fiber based THz systems without and their fragile handling.

### 2.2.2.2 Mesa-Structured Photoconductive Antenna Packages for 1550 nm

In comparison to 800 nm antennas for laboratory Ti:Sapphire laser based systems, photoconductive switches operating at 1550 nm have been developed just recently [24]. The biggest disadvantage for photoconductive switches operating at 1550 nm is the lack of a substrate materials (like LT-GaAs) which offer fast recombination times and high carrier mobilities. Low temperature grown indium gallium arsenide was found to give very fast response times, but its high dark conductivity and therefore the imperceptible change in induced photocurrent prohibited any sufficient THz generation or detection. The solution to this layered LT InGaAs/InAlAs structure was proposed to combine the advantages of both substrate layers – photoconductivity and fast trapping times, respectively. Yet, these first photoconductive antennas consist of 100 periods of InGaAs/InAlAs and due to their surface electrodes the electric field does not penetrate all periods equally, resulting in a gradient in THz generation or detection over depth (cf. Figure 8).

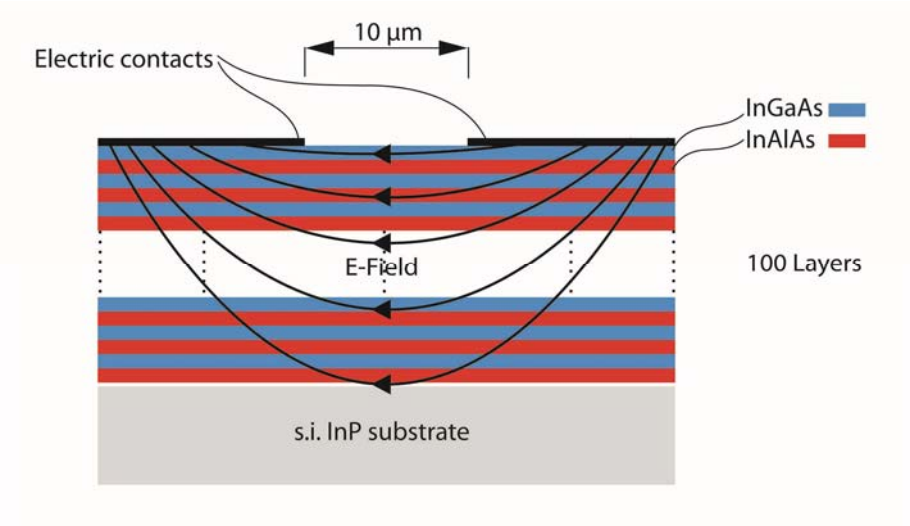


**Figure 8: Planar InGaAs/InAlAs structure and the applied electrical field[25].**

As the interaction between the generated photo carriers and the applied electrical field is far from optimal, researchers at the Heinrich-Hertz-Institute came up with an optimized design for the layer growth and electrode positions. The so called mesa structure is build up by depositing the metal electrodes on the side of the etched down layer stack (see Figure 9).

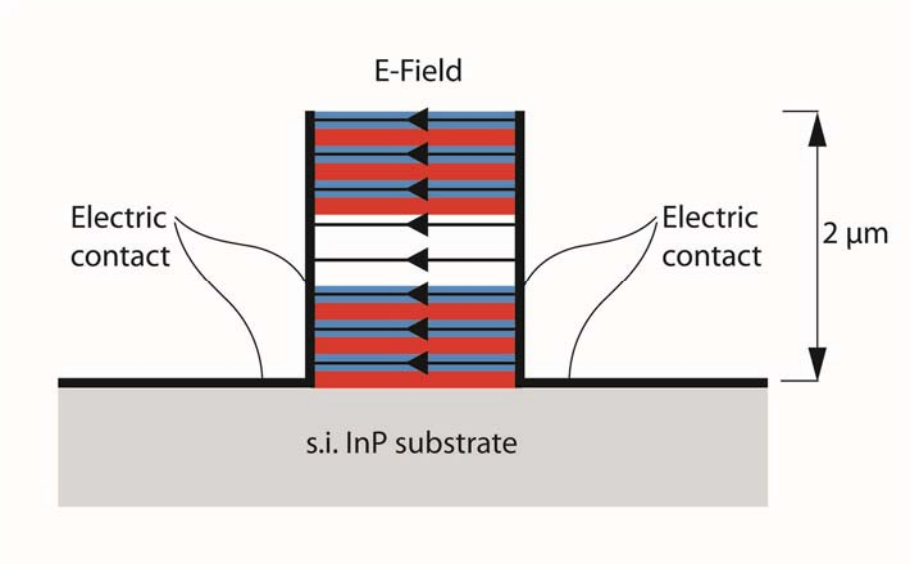


**Figure 9: Mesa InGaAs/InAlAs structure and the applied electrical field[25].**

The electric field distribution is uniform throughout all periods of the InGaAs/InAlAs stack and maximizes the generated and detected THz radiation. An electron microscope image of the Mesa metallization layer is depicted in Figure 10.

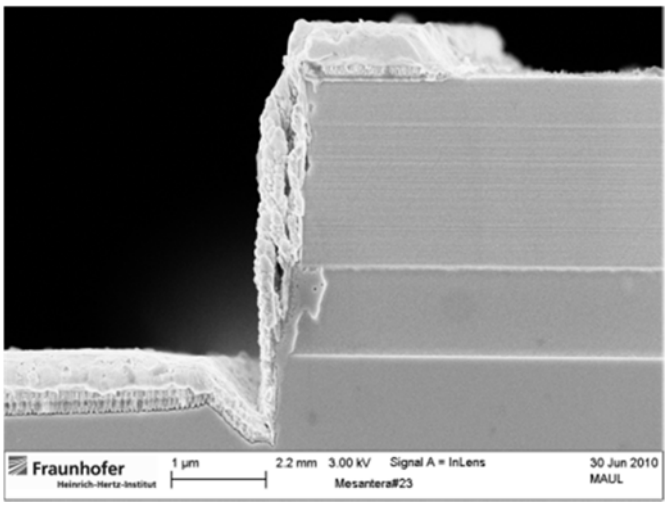


**Figure 10: Picture of the cross-section of a Mesa structure under an electron microscope. (Thanks to [25])**

Due to this additional fabrication steps the performance of these novel devices exceeds the predecessor by more than a factor of 27. Especially the reduction in dark current benefits the radiated THz output power[26] and the receiver's sensitivity. The emitted spectral bandwidth extends up to 4 THz and is now comparable with LT-GaAs based photoconductive antennas.

#### 2.2.2.3 Overview on Antenna Structures

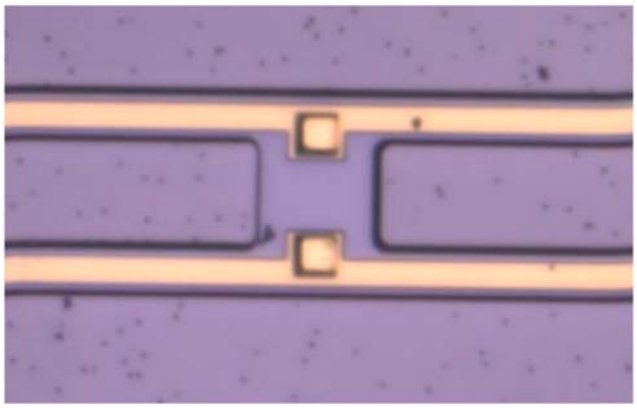

**Figure 11: Photograph of a stripline mesa antenna.**

For optimal bandwidth in a pulsed TDS system, the mesa structured substrates are fabricated with a custom metal antenna design. Two basic concepts are most popular, targeting high THz output powers or broadband emission. Bowtie structures favor a specific frequency region and offer optimal output power levels at this frequency. The downside is a sharp drop in output power at other frequencies resulting in a limited bandwidth. Stripline (see a picture in Figure 11) and dipole designs offer the broadest bandwidth but come with reduced spectral brightness. Schematics of these three different antenna structures are depicted in Figure 1.

Recorded THz traces from a TDS system using bowtie antennas as emitter and detector is shown in Figure 12. It can be clearly seen that the detected signal from the bowtie antennas is a factor 5 higher than from a system with a stripline emitter and a dipole detector. As the signal to noise ratio and not total amount of output power is the important figure of merit, the bowtie antenna is not necessarily the best choice.

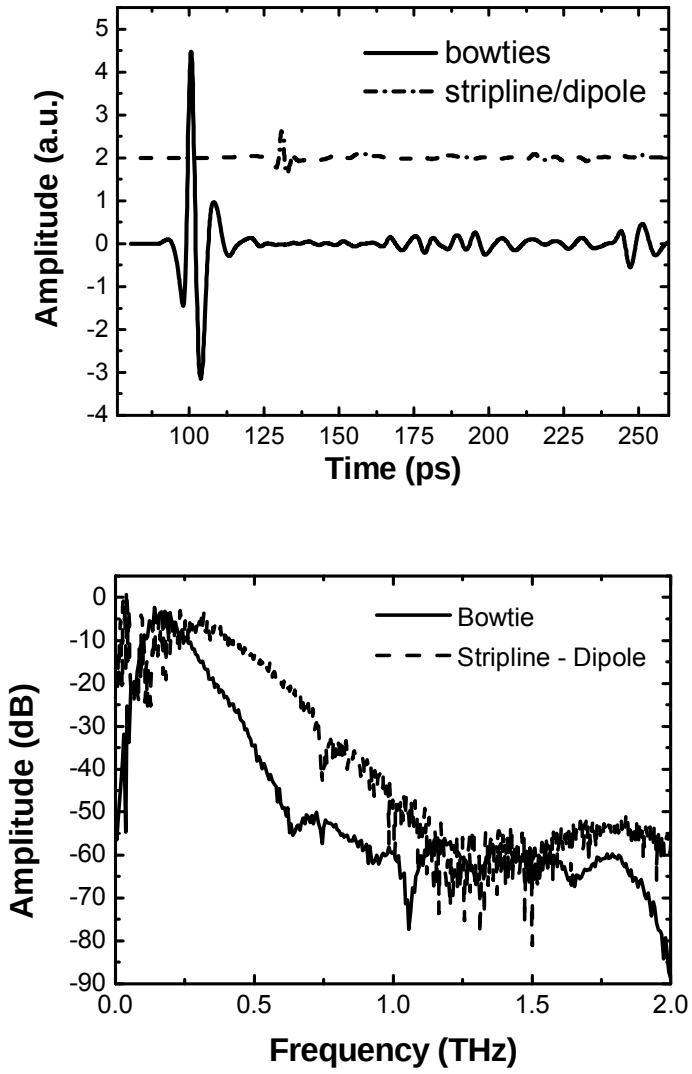


**Figure 12: Time signal(offset for clarity) and corresponding frequency spectra of bowtie and stripline/dipole THz antennas.**

## 2.3 Continuous Wave Terahertz Spectroscopy

Another established method to generate THz radiation and perform highly accurate measurements is the continuous wave (CW) THz spectroscopy. There are several ways to emit all THz power in one frequency component: One of the first optical sources was the molecular far infrared (FIR) laser which operates to frequencies down to 300 GHz, but is a bulky setup and can only be tuned by changing the active gas in the chamber. More recently, the quantum cascade laser (QCL) was realized and offers now output frequencies ranging from the infrared (IR) down to single digit THz[27]. The biggest drawback of QCLs for the lower frequency regime (< 10 THz) is the required cryogenic cooling and the very limited tuning range[28]. But there are electrical methods available

for generating continuous wave THz radiation like gunnor IMPATT diodes [29], HBT transistors [30] or uni-travelling carrier (UCT) diodes [31].

Up to now, only CW spectrometers based on mixing two laser lines with slightly different frequencies offer the same simple operation, stability and repeatability in the acquired measurement results as fiber based TDS systems. This “beating” of two optical beams is also called photomixing[32]. Usually, such photomixing THz systems have either one laser diode emitting simultaneously on two lines, or two separate laser diodes generating a single mode beam. Tuning those laser lines in respect to each other, one can control the resulting difference frequency. The frequency shift can be achieved by changing for example the temperature of one of the lasers. In the following the theoretical principle of heterodyne conversion is explained, including the configuration of a typical continuous wave THz spectrometer.

### 2.3.1 Theory of Photomixing

Heterodyne down conversion, also called photomixing, is a method to mix two slightly different optical frequencies on a photoconductive semiconductor in order to generate continuous wave THz radiation. By overlapping two laser beams, the intensity on the photoconductive material is quadratically dependent on the incident electrical field,

$$I(t) \sim |E_1 \cos(\omega_1 t) + E_2 \cos(\omega_2 t)|^2 , \qquad (2.7)$$

and results in four mixing products: $2\omega_1$, $2\omega_2$, $\omega_1 - \omega_2$, $\omega_1 + \omega_2$. This down conversion is typically also performed on an antenna chip with a metalized antenna structure on top. The optical power conversion efficiency to THz is around $10^{-6}$-$10^{-5}$[33]. Increasing the intensity of the incident optical beam close to thermal failure of the device yields maximum THz output levels in the microwatt range. A schematic principle is shown in Figure 13.

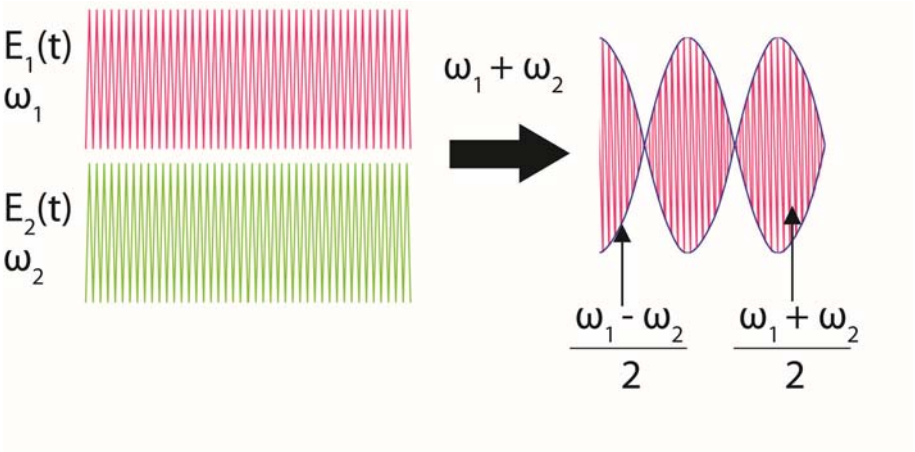


**Figure 13: Principle of heterodyne down conversion (photomixing).**

By assuming that the electrical fields of the two mixing beams are equal, the resulting intensity equals:

$$I(t) \approx E_0^2 + \frac{E_0^2}{2}\cos(2\omega_1 t) + \frac{E_0^2}{2}\cos(2\omega_2 t) + E_0^2\cos((\omega_1+\omega_2)t) + E_0^2\cos((\omega_1-\omega_2)t). \quad (2.8)$$

Except for the difference frequency $\omega_{diff} = \omega_1 - \omega_2$, all mixing products oscillate much faster than the recombination time $\tau_R$ and can therefore be neglected as they will not modulate the carrier density significantly. The optical intensity reduces to

$$I(t) = I_o + I_B\cos(\omega_{diff}t)\,, \quad (2.9)$$

with $I_0 = I_1 + I_2$ as the average intensity, and

$$I_B = 2\sqrt{\mathrm{mI_1I_2}}\,, \quad (2.10)$$

m describing the overlap ratio of the two optical beams, ranging from 0 to 1. Hence, the incident optical power follows the same modulation frequency:

$$P_I(t) = P_o + 2\sqrt{\mathrm{mP_1P}}\cos(\omega_{diff}t)\,. \quad (2.11)$$

This time variant optical power modulates the conductivity of the photoconductive antenna within the gap. The conductance is dependent on:

$$G_A(t) \approx n(t)e(\mu_h+\mu_e)\frac{L_aW_e}{W_g}\,. \quad (2.12)$$

With n as the photocarrier pair density, $\mu_h$ and $\mu_e$ are the hole/electron mobilities, $L_a$ the absorption depth of the photoconductive material and $W_e$ and $W_g$ are the widths of the electrodes and the gap, respectively. The carrier density varies over time correlating with the incident optical power:

$$\frac{dn}{dt} = \frac{\eta_e P_I}{hf_o L_a A} - \frac{n}{\tau} = \frac{\eta_e P_0}{hf_o L_a A}\left(1 + \frac{2\sqrt{\mathrm{mP_1P_2}}\cos(\omega_{diff}t)}{P_0}\right) - \frac{n}{\tau} \quad (2.13)$$

Where $\eta_e$ is the external quantum efficiency, $hf_0$ is the photon energy and A is the active gap area ($W_e \cdot W_g$). Solving this first order differential equation for the steady state, it can be approximated to:

$$n(t) = \frac{\eta_e P_0 \tau}{h f_o L_a A}\left(1 + \frac{2\sqrt{\mathrm{mP_1P_2}}\sin(\omega_{diff} t + \varphi)}{P_0\sqrt{1+\omega_{diff}^2\tau^2}}\right) \tag{2.14}$$

with $\varphi = \tan^{-1}(1/\omega_{diff}\,\tau)$. The carrier density, varying with the difference frequency $\omega_{diff}$, modulates the photomixer's conductance (Eq. (2.12)):

$$G_A(t) = \frac{\eta_e \tau e(\mu_h + \mu_e) P_0}{h f_o W_g^2}\left(1 + \frac{2\sqrt{\mathrm{mP_1P_2}}\sin(\omega_{diff} t + \varphi)}{P_0\sqrt{1+\omega_{diff}^2\tau^2}}\right) = G_0[1 + \beta\sin(\omega_{diff} t + \varphi)]\,. \tag{2.15}$$

For low optical power incident on the antenna gap, the short-circuit external responsivity *S* relates to the conductance $G_0$ through:

$$S = \frac{G_0 V_B}{P_0}\,. \tag{2.16}$$

An equivalent circuit of the antenna is drawn in Figure 14. The photomixing gap comprises the conductance $G_P$, a contact resistance $R_S$, and the geometry dependent antenna capacity *C*.

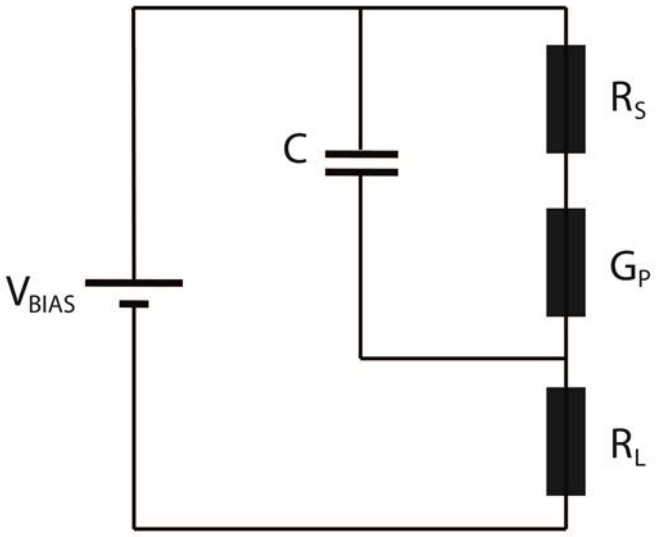


**Figure 14: Equivalent circuit of a standard photomixer and the antenna ($R_L$).**

$R_L$ represents the antenna's load resistance, which radiates the power delivered by the modulated voltage. Abiding Kirchhoff's current law, the time variant voltage $V_P$ across the photomixer follows the differential equation (2.17):

$$\frac{dV_P}{dt} = \frac{V_{Bias} - V_P}{R_L C} - \frac{V_P}{C(R_S + G_P^{-1}(t))}. \tag{2.17}$$

The contact resistance $R_S$ can be neglected in the case of $R_L/R_S \gg 1$, and $R_S G_0 \ll 1$.

The solution of this differential equation does not consist of elementary functions [34], so rather a simplified model is applied: The photomixer can be seen as an AC current source, with the drive voltage of $V_{Bias}$ ($V_P$ very close to $V_{Bias}$) and the modulated conductivity $G_P$ – still neglecting the contact resistance:

$$I_P = G_A V_{Bias} = V_{Bias}(G_0 + G_0 \beta \sin(\omega_{diff} t + \varphi)). \tag{2.18}$$

While only the AC component contributes to the electromagnetic radiation and the photomixer is de facto a current source, the current flowing within the antenna calculates to:

$$I_{R_L} = \frac{1}{1 + j\omega_{diff} C R_L} V_{Bias} G_0 \beta \sin(\omega_{diff} t). \tag{2.19}$$

By assuming the incident optical powers of both beams are equal and perfectly overlapped (m = 1), β becomes:

$$\beta = \frac{1}{\sqrt{1 + \omega_{diff}^2 \tau_r^2}}. \tag{2.20}$$

The radiated power by the antenna can therefore be calculated to

$$P_R = R_L {I_{R_L}}^2 = \frac{R_L (G_A V_{Bias})^2}{2\,(1 + j\omega_{diff} C R_L)^2 (1 + \omega_{diff}^2 \tau_r^2)^2}. \tag{2.21}$$

This result discloses two important things for operating a continuous wave antenna at its optimum. First, the used photoconductive semiconductor has to feature a low C and $\tau_R$ for the photomixing process still working efficiently at higher frequencies, due to the 12dB/octave drop induced by the two low pass cutoff frequency poles. Second, the radiated power is quadratically dependent on the applied bias voltage and the antenna's conductance. The bias voltage has a fundamental limit with the break through value of the material itself. Same upper limit holds true for the conductance, which is linear dependent on the incident optical power, which has an upper threshold as well before thermally damaging the device. All in all photomixing has fundamental efficiency limitations and works best in the lower THz frequency range. A full and more comprehensive analysis and overview can be found in Tonouchi's review paper [35].

The detection of continuous wave THz radiation can be performed with thermal detectors, like a bolometer, or by coherent detection. In the following last part of this review on CW spectrometers, the coherent detection scheme is discussed as it is the method of choice for most real world applications.

A second photoconductive antenna is used for the coherent detection. The electrical THz field present at the detection antenna induces a current density in the unbiased gap region:

$$J(t) = n(t) e \mu_e E_{THz} \quad . \tag{2.22}$$

That leads to a detected current of

$$I_D \approx G_D E_{THz} W_G \, . \tag{2.23}$$

While the detector's conductivity is dependent on the optical excitation and its corresponding phase (Eq. (2.15)), the incoming THz field inhibits a different phase due to the different path through air. The detected current can therefore be described as:

$$I_D \approx G_{D_0}\left(1 + \beta_D \cos\left(\omega_{diff} t + \varphi_{opt}\right)\right) E_{THz} \cos(\omega_{diff} t + \varphi_{THz}) \, . \tag{2.24}$$

By expanding the formula and taking into account that only an average value over time can be detected in the antenna, only the phase dependent DC value remains:

$$\begin{aligned} I_{det,DC} &\approx G_{D_0} E_{THz} \cos\left(\varphi_{opt} - \varphi_{THz}\right) \\ &\approx P_{det} E_{THz} \cos(\Delta L \frac{\omega_{diff}}{c}) \, . \end{aligned} \tag{2.25}$$

With $G_{D0}$ direct proportional to the incident optical power $P_{det}$ at the detector and $\Delta L$ as the path length difference between the incoming THz and optical beams. The THz signal can be detected by varying the path difference and the acquired signal comprises a cosine waveform. The maximum amplitude can be seen by matching the phase in both arms.

## 2.3.2 Continuous Wave THz Spectrometer Setup

A brief introduction to a standard CW THz spectrometer is given in the following paragraphs. The system presented was used in chapter 5 for the novel hybrid system approach, but can also be used on its own.

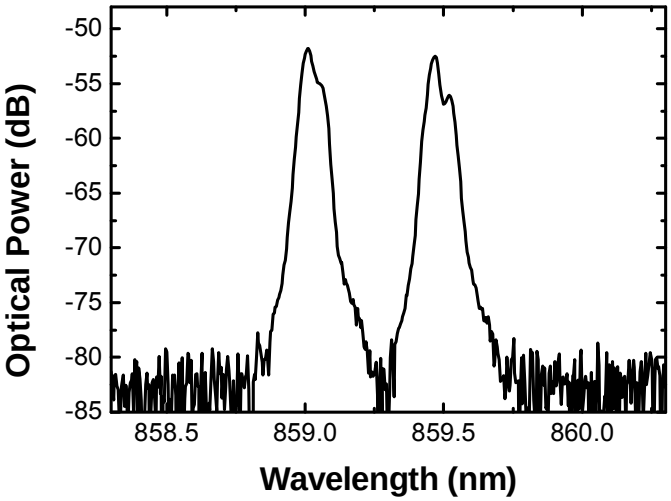


**Figure 15: Optical spectrum of the combined CW lasers measured with an optical spectrum analyzer.**

The two lasers used for this photomixing setup are distributed feedback (DFB) lasers from Toptica (DL100) emitting a narrow single mode beams at 850 nm. Both lasers have a slightly different center wavelength and can be tuned by changing their temperature. A TEC unit (DTC110) is integrated in the laser controller (DCC110) to generate the desired wavelength spacing. For higher frequency stability it is possible to monitor the output wavelength and correct the temperature with a feedback loop. This fully computer controlled system can achieve a frequency accuracy of a few MHz. The combined output spectrum can be seen in Figure 15.

The combined CW beam is divided by a beam splitter and guided over a delay line to the emitter and detector antennas. A measured sinusoidal THz time signal and the corresponding frequency spectrum are depicted in Figure 16.

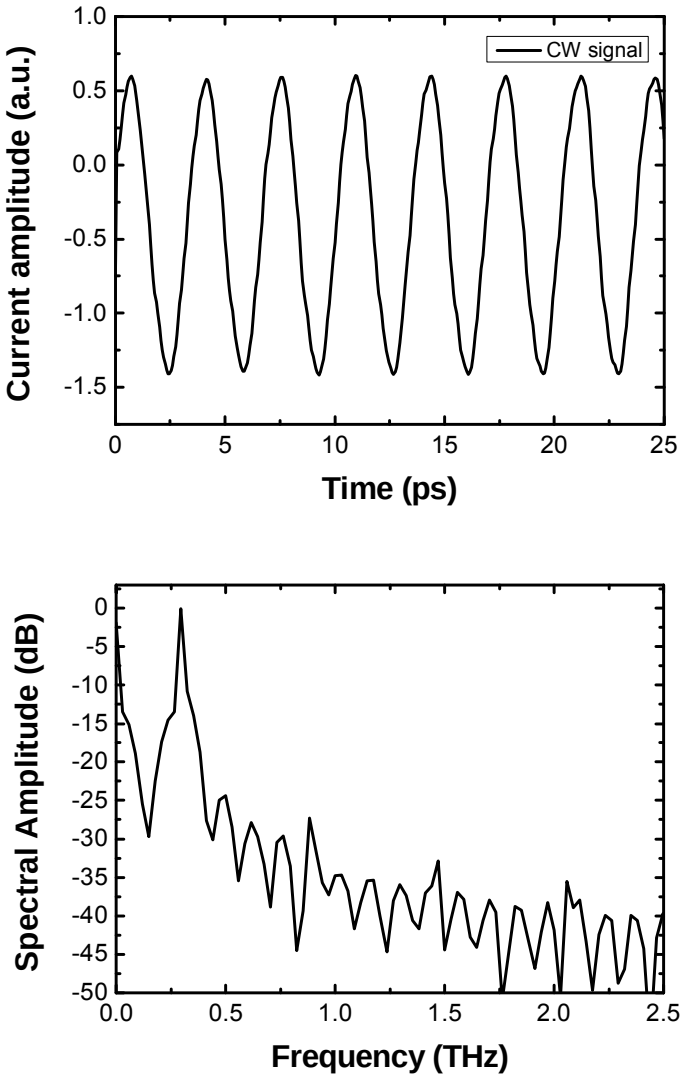


**Figure 16: Continuous wave time domain signal and spectrum.**

# 3 THz Near-Field Imaging of Polymer THz Fibers

Over recent years, diverse research studies of the interaction between THz radiation and matter have been performed. This enabled the understanding of carrier dynamics in solid-state [36] and or biological systems [37] of high complexity. Yet, THz spectrometers developed to date have suffered from large diffraction limited focal spot sizes and for some applications a low overlap between the THz focal spot and the optical sampling beam. Possible solutions for tighter THz wave confinement are waveguides for the terahertz regime which would allow for denser field distributions and penetrating otherwise inaccessible sampling areas in highly absorbent environments, e.g. within liquids or human tissue. These robust and potential low-cost waveguide solutions might enable new sensors and novel sensing applications in the THz field. However, it is still a challenging task to provide efficient low loss transmission of terahertz waves within a guiding material.

Methods for guiding THz radiation with low loss and negligible dispersion have been based on their equivalents in electronics as well as in the optical world. Examples of these cross over designs are metal planar waveguides which have been demonstrated in various shapes, including rectangular, square or circular waveguides [38], parallel-plate waveguides [39], but also plastic [40] and metallic ribbon waveguides [41], thin metal wires [42] or polymer wires [43] have been realized, just to name a few.

All metallic waveguides rely on propagation of the electrical field through the surrounding material, which is air in most of the cases. But this means that the metallic structure only provides guiding boundaries and is therefore by definition weakly guiding with a low confinement factor. Another downside is the resulting high bending loss through such weak guiding waveguides [44], which limits their applicability. Thus, for proper guiding and the ability to tailor the dispersion and confinement to one's needs a dielectric index guiding scheme is beneficiary. Another advantage of dielectric guiding is the enclosed wave propagation, typically without any interaction with the external world, rendering the THz radiation unaffected by humidity or other environmental influences. First demonstrations of microstructured THz fibers in polymer have been presented in the recent past [45-48].

In this chapter, novel microstructured polymer based THz fibers are presented and evaluated by THz near field imaging. A near-field time domain spectrometer was set up and improved to offer fast and easy operation. In cooperation with the polymer fiber group at the Danish Technical University (DTU Fotonik, Copenhagen, Denmark) a novel fiber design was fabricated by adding an absorber material in the outer fiber regions, which leads to higher confinement and elimination of higher order modes and thus multimode dispersion effects of the THz signal can be avoided.

# 3.1 Design and Fabrication of THz Fibers

## 3.1.1 Materials Used for THz Fiber Fabrication

About ten years ago, the first index-guiding microstructured polymer crystal fibers for THz radiation were presented by Han et al. in 2002 [49]. The idea is similar to the much smaller silica based optical fibers, which have extremely low losses and the feasibility of endlessly single-mode guiding [50] or even introducing zero guiding dispersion [51]. These microstructured fibers have been studied extensively and their waveguide characteristics for both silica and polymer optical fibers have been investigated. But in contrast to polymer optical fibers for the visible and near-infrared domain, the number of suitable THz substrate materials is more limited. While polymethyl methacrylate (PMMA) and polycarbonate (PC) are perfectly transparent for optical wavelengths, their molecular chains have polar groups attached and the resulting dipole moment leads to an increased absorption of THz frequencies. Studies of material parameters on a wide range of polymers and their compounds suited for the THz range have been performed in the last decade [52]. In order to reduce or eliminate dispersion within the waveguide, the optimal material possesses a flat refractive index across a broad window of the THz frequencies and minimal absorption. TOPAS and Zeonor, both cyclic olefin copolymers and nearly identical in their characteristics, match these criteria best. From a low cost perspective, high-density polyethylene (HDPE) or polytetrafluoroethylene (PTFE) are valuable base materials as well and they come with the advantage of being mechanically machined with ease. Thus THz optics like different types of lenses or prisms can be fabricated at low cost [53]. Their limitation lies in the increased absorption for higher frequencies above 1 THz and they are therefore best suited for systems operating at lower frequencies.

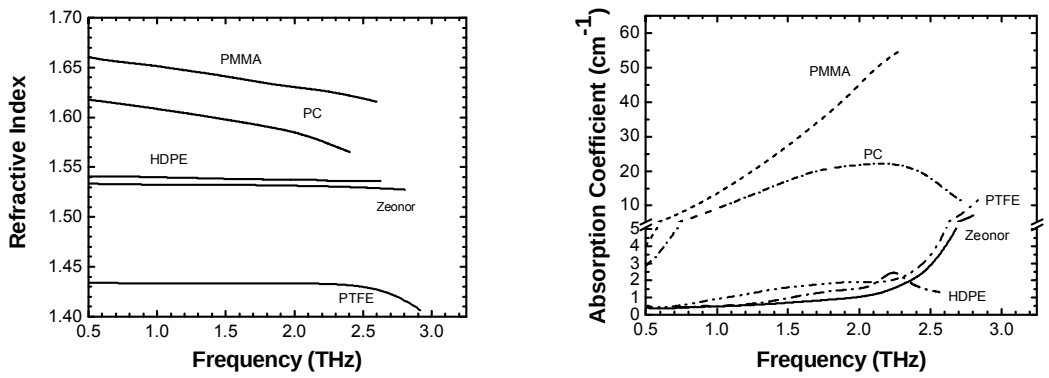


**Figure 17: Refractive index and absorption coefficient of relevant polymers [54].**

An overview on the refractive indices and the absorption for commonly used polymers is shown in Figure 17. It can be clearly seen that Zeonor, Teflon (PTFE) and HDPE have a nearly flat refractive index up to 2 THz. Yet, Zeonor has the lowest and flattest

absorption curve. Nielsen et al. [46] demonstrated a low-loss TOPAS photonic crystal THz fiber in 2009. TOPAS and Zeonor are most commonly used for polymer based THz fibers, due to their low loss, negligible dispersion, and the ability to draw the material in a fiber drawing tower.

### 3.1.2 Polymer Fiber Drawing

In the following subchapter polymer fiber drawing is presented in detail, as it is used not only for fabricating THz waveguides measured in this chapter, but also for fabrication of polymer based THz filters presented in the next chapter. Polymer fiber drawing is similar to pulling silica based telecommunication optical fibers. The change of the preform material from glass to polymers comes along with several advantages and fabrication simplifications. Silica based glasses have their glass transition state above 1800°C, yet polymers and their compounds start getting soft and smooth at around 200°C, most of them even below that point. While pulling down any preform the inscribed holes or lattice structure scales down with the reduction of the fiber's diameter. Mainly mechanical drilling is used to inscribe holes or otherwise shaped forms in patterns into the preform like triangular or hexagonal lattices. Thus, it is possible to fabricate micrometer thin holes and structures in optical fibers with approx. 125 µm outer diameters [55, 56]. For the THz region the target dimensions of the final fiber lies in the millimeter range. A schematic of a fiber drawing tower is shown in Figure 18.

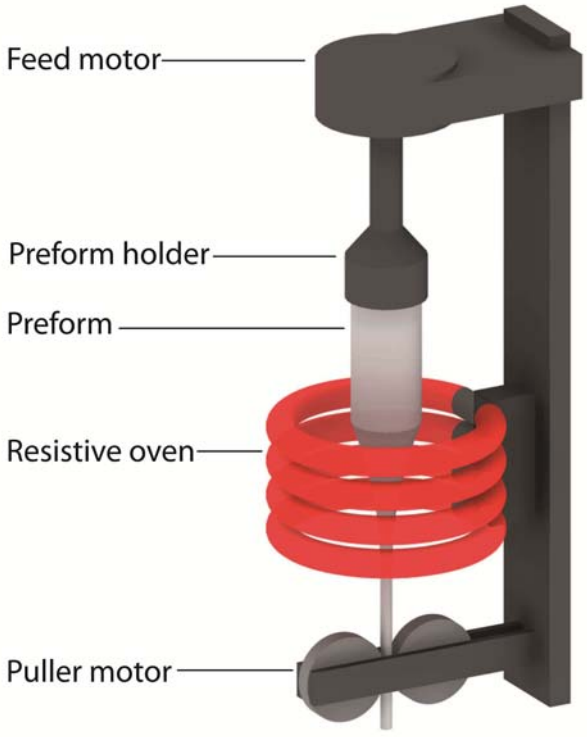


**Figure 18: Schematic of a fiber drawing tower.**

The preform is clamped into the preform holder at the top of the tower and is heated up by a localized heating zone within the oven. When the polymer material becomes soft and tensile the weight of the lower part is pulling the preform apart and a bottleneck forms in the heat zone (cf. Figure 19). The oven can either be fitted with convectional (resistive) heating or optical radiation heating by infrared (IR) arc lamps. The reduced canes are fed through the puller wheels and can then be drawn down to its desired diameter. The feeding and the pulling speed are crucial parameters, along with the right oven temperature. As long as the material stays soft and tensile, the feed and pull speeds determines the resulting fiber diameter. Due to the conservation of mass, the pulling speed has to be the feeding rate times the quadratic factor of the desired diameter reduction. For example, to reduce a 50 mm preform down to a 10 mm THz fiber at a feeding rate of 20 mm per minute requires a pulling speed of 0.5 m per minute. The steps of getting a fiber draw started are shown in Figure 19.

**Figure 19: Initial drawing steps of a fiber draw run with bottle neck emerging (heat zone in red).**

For this thesis preforms for THz canes and polymer optical fibers have been drawn on three different drawing towers. A resistive heating tower at Macquarie University was used for initial polycarbonate (PC) and polymethyl methacrylate (PMMA) optical fiber draws. More sophisticated draw runs for polymer optical fibers were performed at the facilities at the University of Sydney. Their fiber tower is a refitted silica draw tower with a customized IR-lamp oven. The fast and uniform heat distribution within the preform allows for very stable and highly accurate pulling conditions. It was possible to achieve diameter variations of industrial standards of 1 µm over several hundred meters of fiber with a target diameter of 125 µm. TOPAS preforms for THz fibers were mainly provided through a collaboration with the Danish Technical University (DTU) in Copenhagen, Denmark. Their commercially bought drawing tower is fitted with a high grade resistive oven. A more comprehensive overview on the general drawing procedure and DTU's fiber tower can be found here [57].

### 3.1.3 Simulation and Computer Assisted Design

Describing the electromagnetic field propagating within a specific structure or waveguide, the Maxwell equations provide all necessary information. In optics the characteristic material parameters are given by the absorption $\alpha$ and the refractive index $n$. In the case of negligible absorption as in silica based optical fibers with losses of 0.1 dB/km, the formulas become quite simple but if the absorption cannot be neglected, one has to consider the complex refractive index

$$\bar{n} = n - i\kappa \tag{3.1}$$

with $\kappa = \frac{\alpha}{2}\frac{c}{\omega}$; $c$ denoting the vacuum speed of light and $\omega$ is the angular frequency of the propagating wave.

Except for the simplest structures, solving the electromagnetic field equations is usually done by numerical modeling. In the case of index-guiding waveguides with the assumption that the boundaries are in transverse direction and that the wave is propagating in the z-axis direction, commercially available software tools, so called mode solvers, can be used. The modeling and solver software COMSOL can address almost all structural designs and incorporates the possibility of adding complex refractive indices by simultaneously reducing the number of calculations by taking into account the device symmetries [58]. Standard index-guiding photonic crystal THz fibers are circular shaped in the transverse plane and have symmetrical features so that the computational effort can be reduced by a factor of 4 by taking only one quarter of the lattice structure into account. A simulation of an arbitrary fiber lattice in COMSOL is shown in Figure 20.

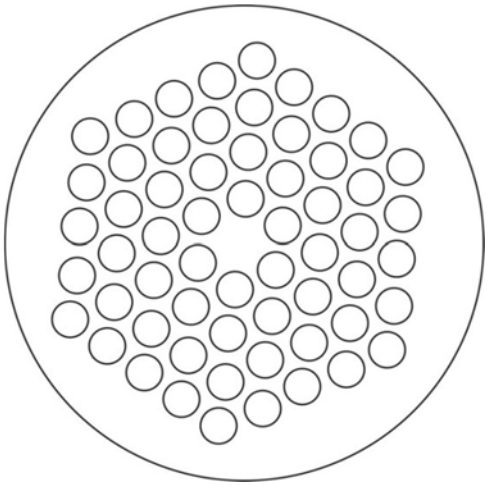

**Figure 20: Schematic of an arbitrary THz fiber lattice.**

The standard characterization and design parameter for triangular shaped microstructured fibers is the V parameter (normalized frequency) [59]. This value in its original form is used for describing standard step-index fibers, but by taking into

account the extended effective V parameter for holey fibers presented by Koshiba et al.[60] one can estimate the behavior of microstructured fibers. The V parameter is given by

$$V_{eff} = \frac{2\pi}{\lambda} a_{eff} \sqrt{n_{core}^2 - n_{FSM}^2}. \tag{3.2}$$

with $\lambda$ as the operating wavelength, $\alpha_{eff}$ is the effective core radius, $n_{co}$ and $n_{FSM}$ are the refractive index of the core and effective cladding, respectively.

Simulation and measurements performed in Koshiba's publication verified that the cutoff condition of $V_{eff}$ = 2.405, known from standard step-index fibers, holds true as well. Inserting this value in Eq. (3.2) results in a function for the relative cutoff wavelength $\lambda/\Lambda$ as a function of relative hole diameter $D/\Lambda$, where $\Lambda$ is the hole pitch.

Three regions can be identified accordingly [60]: For relative hole diameters below 0.43 the fiber can be endlessly single moded. Above this "endlessly single mode threshold" of 0.43, microstructured air-hole fibers are considered single or multi moded dependent on the wavelength. Thus, the cutoff wavelength for triangular lattice THz fibers can be calculated as well.

## 3.2 THz Near-Field Imaging

THz waveguides and especially THz fibers are usually characterized for their dispersion and material losses, which is performed with standard THz spectrometers as presented in chapter 2. But for verification of the electrical field distribution within THz waveguides it is very interesting to see the effects of air holes with feature sizes of the targeted wavelength. The relative lattice features compared to the guiding wavelength is one of the main differences between fibers for the optical domain and THz fibers. In order to visualize all localized effects of the fiber's lattice one cannot look at the far field which is by default detected by the THz receiver but has to consider the near field electromagnetic field distribution. The distance of the sampling point distinguishes between a near-field and far field measurement. For distances greater than two times the targeted wavelength the electrical field is detected as plane waves, giving the far field pattern. Closer than one full wavelength, the so called near field can be measured which is still affected by sub wavelength features or perturbances in the beam path or any other frequency dependent effects in the waveguide. Techniques for high-resolution imaging beyond the wavelength dependent diffraction limit were known for a long time in RF applications and in microwave systems [61], as well as in conventional optical systems [62-64]. The technique for the optical domain is called near-field optical microscopy and relies on a sub-wavelength scanning in close vicinity of the surface or imaging plane of interest. The intensity measured behind a small aperture or the

measured reduction due to a sub-wavelength beam block like a metal tip or metal coated optical fiber is mainly dependent on the size of the aperture/tip rather than the diffraction of the passing wave front. This method allows for a spatial resolution several magnitudes below the wavelength [63]. Expanding this scheme in the THz frequency region was demonstrated by Hunsche et al. at Bell Labs in 1997 [65]. Since then, different methods of introducing a small perturbance in the THz beam path have been proposed. An elegant and flexible method is the use of an optically gating excitation to modulate the transmitted THz field which was first introduced by Zhang et al. in 2000 [66]. This scheme is used in the near-field setup employed for all measurements done on THz fibers in this thesis. The principle bases on detecting the difference between an unhindered beam and a locally blocked beam. This difference THz time domain signal is sampled with a delay line and one obtains a full difference wave form dependent on the position and diameter of the blocked area.

In this chapter, the principles of the dynamic aperture near-field imaging scheme are applied to fit the needs of THz fiber mode profiling. The basic setup is presented in the following paragraphs and near field images of various fiber designs are discussed and analyzed.

### 3.2.1 Material Parameters for Dynamic Aperture Near-Field Imaging Setup

For the measurements performed in subchapter 3.3, near-field imaging is applied in order to resolve the spatial electrical field intensities across the THz fiber's cross section. The idea behind dynamic aperture imaging is the modulation of the transmitted THz wave by a semiconductor layer by locally excited photo carriers. Ideally, the material should have no absorption for THz frequencies when there is no optical excitation present and a high carrier density while illuminated. Standard materials used for THz applications in that regard are high resistive silicon (HR-Si) and gallium arsenide (GaAs). First, the general parameters which determine the ability to effectively change the THz transparency are discussed. Similar to chapter two, the Drude model is applied to calculate the photo carrier density modulation. The excited number of carriers within the semiconductor follows equation (2.3), but is also dependent on the photon energy (see Figure 21).

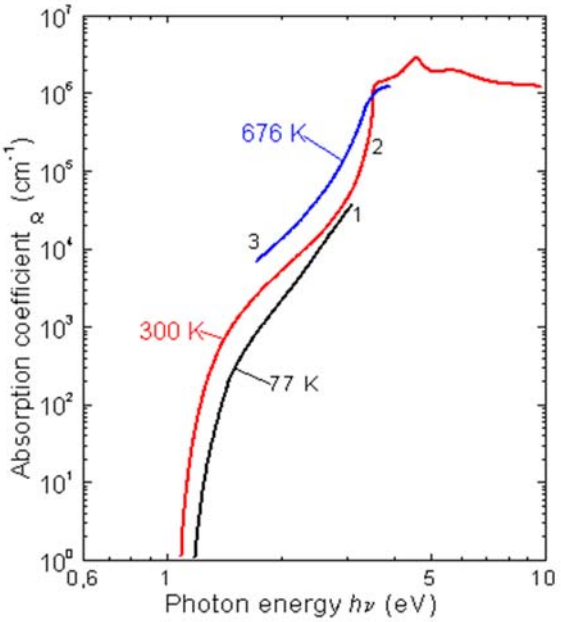


**Figure 21: Photon energy dependent absorption of Silicon[67].**

The generation rate *G(t)* is primarily dependent on the incident optical power. In the case of continuous wave excitation, which will be used in this approach, it can be assumed in the stationary equilibrium $G_0$. The generated photo carrier density $n_{pc}$ equals

$$n_{pc} = \tau_r \cdot G_0 \,, \tag{3.3}$$

with $\tau_r$ as the material's recombination time constant.

The semiconductor's permittivity $\varepsilon_r$ is connected to the conductivity of the material $\varepsilon_m$ and therefore influences the transparency for THz frequencies directly

$$\varepsilon_r = \varepsilon_m + \frac{i\sigma}{\epsilon_0 \omega} \tag{3.4}$$

with $\varepsilon_0$ as the vacuum permittivity, $\omega$ the angular frequency of the incoming radiation and the conductivity $\sigma$ given by [68]

$$\sigma = \frac{\epsilon_0 \tau_s \omega_p^2}{(1 - i\omega\tau_s)} \tag{3.5}$$

where $\omega_p$ denotes the plasma frequency, which is given by

$$\omega_p = \frac{e^2 n_{pc}}{\varepsilon_0 m^*} \tag{3.6}$$

With $n_{pc}$ as the photo carrier density, $e$ as the electron charge and $m^*$ as the effective electron mass. The induced carriers modify the conductivity and therefore the refractive index of the material, which is given by the fundamental definition of the refractive index:

$$n = \sqrt{\varepsilon_r \mu_r}\,. \tag{3.7}$$

Note that the semiconductor materials relevant to this thesis have a magnetic permeability $\mu_r$ of close to 1. Thus, a change in free carriers within the material leads directly to a change in refractive index:

$$\Delta n \propto \Delta \varepsilon_r \propto \sigma \propto n_{pc}. \tag{3.8}$$

The higher the excited photo carrier density is, the higher the induced effective modulation in refractive index. Therefore it is substantial having long carrier life times in the semiconductor material. As direct band gap materials like GaAs have a shorter carrier lifetime per se, the best candidates are indirect band gap materials. Potential transparent THz substrates are germanium (Ge) or silicon (Si).

Comparing their characteristic material parameters from values found in the literature [69], it can be seen that under continuous wave excitation the recombination times are in the range of 1 ms, which is several magnitudes higher than the recombination time of GaAs. Their absorption is in the same ballpark, which makes the absolute refractive index the deciding parameter. In order to reduce the amount of THz power lost by the reflection of the surfaces, the material with the lower refractive index is favorable. The reflection coefficient at the air-semiconductor interface is given by the Fresnel equation

$$R = \left(\frac{n_1 - n_2}{n_1 + n_2}\right)^2. \tag{3.9}$$

The refractive index of Ge and HR-Si was determined to 4.0 and 3.418, respectively [70]. It should be noted that exciting a semiconductor material by localized continuous wave excitation generates heat and leads to an increased intrinsic carrier density in the order of $10^{11}$ $cm^{-3}$[69], which is magnitudes below the optical excited carrier densities. Hence, the heat influence is not considered relevant for this continuous wave dynamic aperture scheme.

### 3.2.2 Experimental Setup

The setup comprises a fiber-coupled THz TDS system as presented in subchapter2.2.1. The femtosecond optical pulses are generated in a ring cavity fiber laser and are less than 100 fs long. The optical pulses are guided through glass fibers to the fiber coupled

antennas, thus no free space optical components are required. This enables stable and reliable operation in any environment. A schematic drawing of the TDS setup is shown in Figure 22.

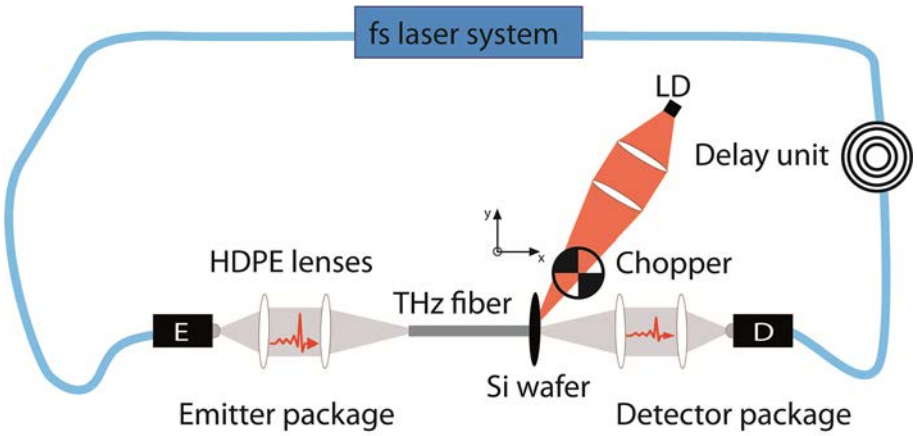


**Figure 22: Schematic of the THz near-field setup.**

The THz beam is collimated and focused by 2" custom designed HDPE lenses with a focal length of 60 mm. Positioned in the focal spot is the polymer THz fiber, which has a very thin HR-Si wafer attached on one end of it. The wafer has a thickness of 50 µm, which is smaller than a full wavelength of interest in the material (cf. $\lambda_{THz}$ = 88 µm).This enables near field modulation of the electrical THz field guided by the fiber even by illumination from the other side. Yet, the reactive near-field region defined by $\frac{\lambda}{2n\pi}$cannot be targeted. The required wafer thickness of 15 µm can't be realized. The continuous wave excitation is provided by a fiber-coupled 3 Watt edge-emitting laser diode operating at 808 nm. The excitation beam leaving the multimode fiber is collimated and refocused to a spot size of approx. 200 µm by standard convex lenses (f = 40 and 75 mm, respectively). As the fiber is highly multi-moded (115 µm core diameter and 125 µm outer cladding diameter) the collimated beam shape features a donut form rather than a Gaussian beam profile. The optical focal size can be determined by taking into account the mode field diameter coming out of the end of the fiber (about 115 µm), the focal length of the lens used to collimate the divergent beam (f = 40 mm) and the focusing lens parameters. To determine the photo carrier behavior in the focal region, the optical excitation beam and its absorption within the semiconductor has to be analyzed. For the lateral distribution a CCD camera was placed in the attenuated beam and moved in steps out of focus in both directions to measure the optical intensity distribution. As can be seen in Figure 23 the multimode collimated donut beam profile results in a flat top focused beam spot. Therefore the optical excitation on the semiconductor wafer can be assumed to be uniform throughout the focal spot size.

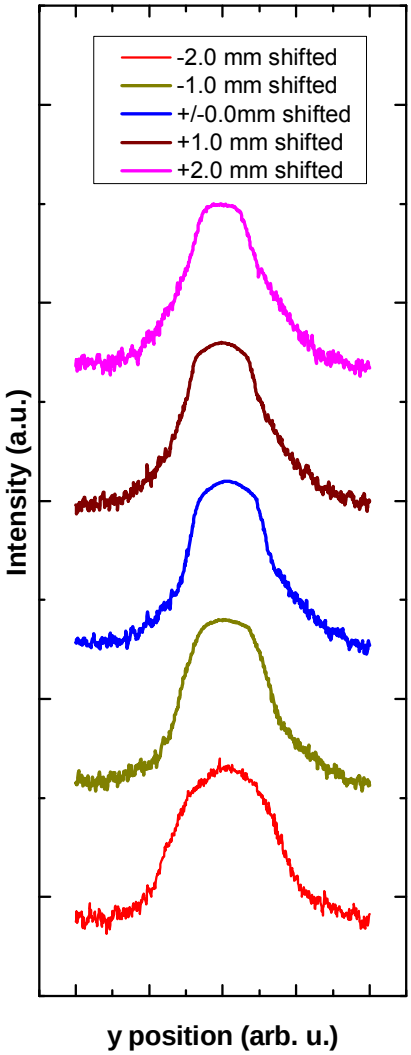


**Figure 23: Optical beam profile with a CCD camera at one line across the center for varying positions of the camera.**

The carrier density distribution in direction of the incoming light (in the depth of the wafer) can be estimated by the absorption length. This value is highly dependent on the material and the wavelength of the excitation (photon energy). The absorption constant over photon energy can be seen in Figure 21. For silicon the absorption length at 808 nm is found to be around 10 µm. It is fair to assume that after 5 times the absorption length basically all incoming photons have been absorbed. The carrier density within the material will decrease with distance from the incident surface. This means that the THz wave, traveling through the wafer from the other side, will experience an increasing carrier density along the way up to the maximum right at the surface of the wafer. As the lateral distribution is uniform, this is sufficient to say that the optical excited spot modulates the passing THz wave uniformly across the focal spot region. The in-axis distribution only determines if all or just portions of the THz wave are blocked. A 100% block is desired as it gives a higher SNR in the detected signal, but

the near field method still reveals the difference signal while blocking only parts of the beam. The carrier diffusion in the lateral plane was simulated with COMSOL. It was found that the expansion of the spot is approximately 2.5% and can therefore be neglected (cf. Figure 24)

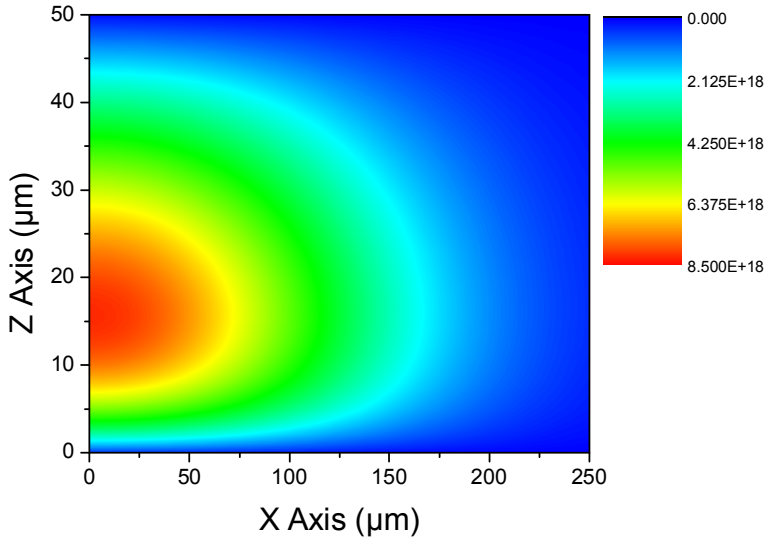


**Figure 24: COMSOL carrier diffusion simulation in a 50 µm HR-SI wafer**

Diffraction effects of the induced optical excited region can be neglected, as the collimating THz lens is far away in respect to the wavelength (f = 60 mm) and detects only plane wave components directed in the propagation direction of the beam. Diffraction effects would be measured as additional absorption. This effect would be relevant if the frequency dependent absolute energies are investigated. For this near field analysis the frequencies are only view separately and the spot size is kept constant for each position on the wafer, so additional absorption caused by diffraction is equal throughout all points in one image.

The excitation beam is modulated by a chopper wheel at a frequency of 83 Hz, which is connected to the Lock-In amplifier as reference frequency as well. The detected Lock-In signal reflects the difference between the partially blocked and the unhindered THz signal and thus revealing the “missing” signal components. By raster scanning the laser focus across the HR-Si wafer, a THz time trace is recorded for each spot (pixel) by delaying the optical detection pulses in regard to the THz pulses. The mechanical delay stage (PI M-683.2U4) was linearly traversed by 1 mm/sec, which corresponds to an induced time delay of 6.66 ps per second. Every 50 ms a data point is recorded, sampling the THz pulse in 333 fs time steps.

## 3.3 Mode Profiling of THz Fibers

While the standard characterization of THz fibers includes the determination of material and waveguide losses and frequency dependent dispersion in the waveguide, all of which can be performed by a common TDS setup, the verification of mode profiles poses a more difficult task. Resolving the localized electrical field components requires a sub-wavelength perturbation of the electrical field in close vicinity of the image plane in question. This can be achieved by forcing the transmitted THz wave through a small aperture or tapered tube [65], by detecting directly – in close physical contact - with a photoconductive antenna at the end of the waveguide [71], or by electro optical sampling in reflection geometry with a nonlinear crystal placed directly at the end facet of the fiber [72]. “Negative” modulation is possible as well, which was presented by Zhang and his group by blocking a small section of the transmitted THz wave[66]. The latter approach is adapted to our measurement setup and consists of a HR-Si wafer which acts as a CW optical excited dynamic aperture. With the propagation of the THz wave in the z-axis, a two dimensional image of the transverse electrical field can be obtained. The THz fibers positioned in the THz focus spot and are hold in place by a foam plastic which has a refractive index in the THz range close to 1, in order to prevent undesired leakage or reflections of a metal holder. The images taken comprise an effective area of 5x5 mm², which covers the whole end facet of the fibers under inspection.

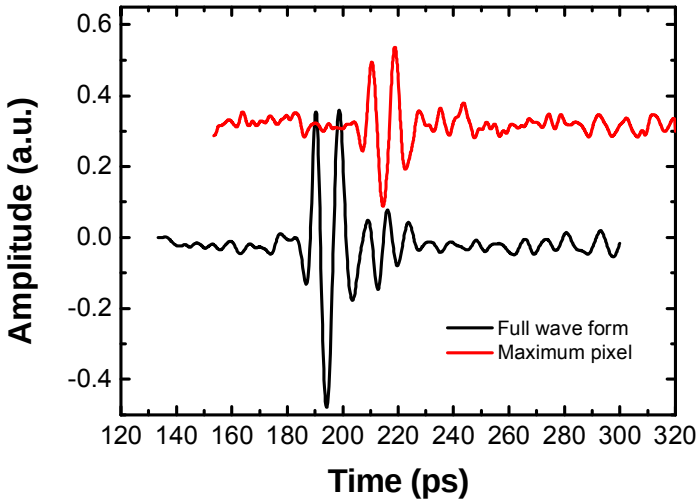


**Figure 25: Time traces of the THz near-field measurement in comparison to a full wave form (for clarity reasons the time trace of the maximum pixel is shifted and offset).**

In Figure 25 the time trace of the center pixel can be seen in comparison to the full wave form propagating through the fiber. Taking the peak-to-peak values for each pixel reveals the total THz field distribution across the THz fibers as all frequency components contribute to the pulse structure. For images of single frequencies, the time

traces are first transformed into the frequency domain by standard fast Fourier transformation (FFT). In a second step the amplitude at the desired amplitude is plotted for each pixel, depicting a relative power distribution.

The illuminated spot size is in the order of 200 µm, but can be reduced by using a lens with a decreased focal length. The reduction in spot size yields a higher resolution, but comes with the tradeoff of smaller interaction with the THz wave and therefore a smaller signal to noise ratio. The smallest feature size the system can safely detect is half the focal spot size. Increasing the optical power results in a higher carrier density in the focal spot and therefore offers a better THz contrast, but the thermal failure level of the photoconductive material sets a limit of optical excitation levels.

## 3.3.1 Measurement Results

### 3.3.1.1 Two Ring Structure

In a first experiment a fiber with a two ring structure was analyzed by near-field imaging. In order to compare the guiding performance of the fiber design and the electric field distribution within the structure of the fiber, a standard polyethylene rod was imaged as a reference. The induced structures by the drill and draw fabrication method had a hole diameter of 285 um and a pitch of 790 µm (see Figure 26). The fiber is compared to a standard PE rod with a diameter of 5 mm. In comparison to optical fibers, THz fibers have a much smaller dimension relative to the guiding wave. This leads to fewer cladding modes, which are spatially less separated from the core modes. Also, guidance by the air-cladding interface has a much stronger effect than in the core defined by the air holes. That effect is used for THz waveguides made out of polymer rods.

All THz fibers fabricated for this thesis have no polarization maintaining design, so in principle the polarization of the THz wave can shift while propagating through the fiber. However, the lattice inhibits no twists inside the fiber and the length of the fiber is considered short in relationship to the wavelength and thus, the polarization is not affected. Measurements done over time verified those assumptions, as no reduction in the transmitted THz field could be detected over several hours.

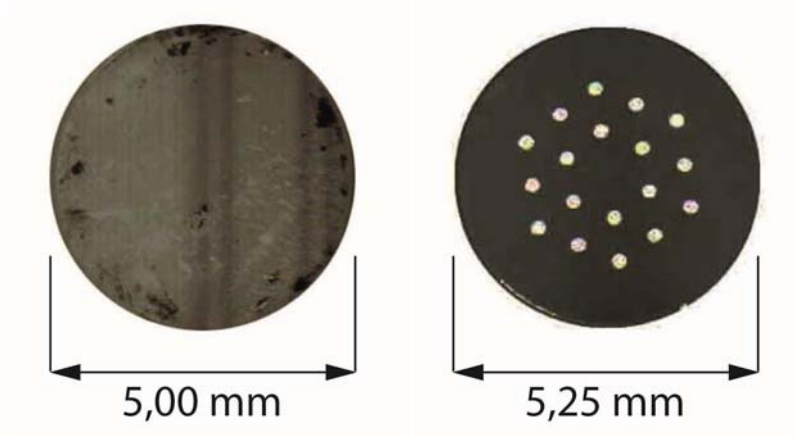


**Figure 26: Picture of a PE rod (5 mm diameter) and a TOPAS two ring structured PCF (5.25 mm outer diameter, 280 µm hole diameter and 750 µm pitch).**

A standard polyethylene (PE) rod is used to compare the structured PCF. The PE-air refractive index difference is enough to make the PE rod a waveguide itself. Pictures of the corresponding cross-sections are shown in Figure 26.

Simulations for both layouts have been performed in COMSOL and the fundamental mode at 500 GHz is shown in Figure 27.

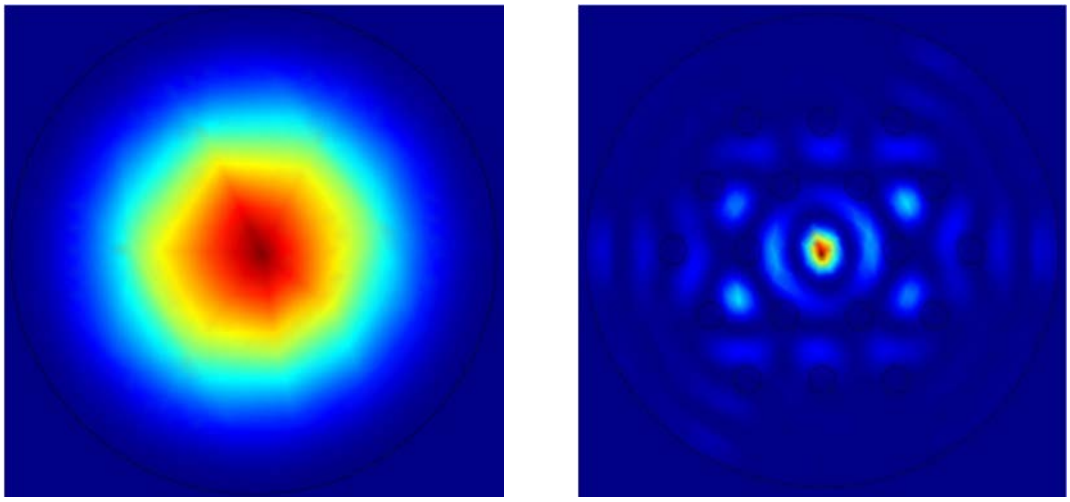

**Figure 27: Mode field simulations for the PE rod (left) and the two ring structured fiber (right) at 500 GHz.**

A 101 x 101 pixel sized image was taken by raster scanning the illumination spot across the HR-Si wafer covering an area of approx. 5 x 5 mm² with a step size of 50 µm. The peak to peak amplitude values for comparison are depicted in Figure 28.

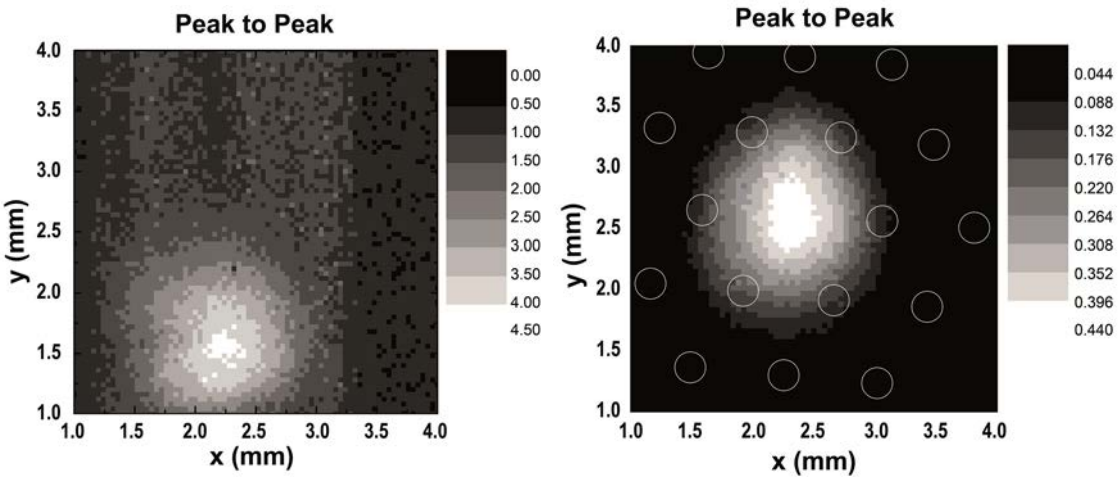


**Figure 28: THz peak to peak image of a PE rod (5 mm diameter) and the two ring structured TOPAS fiber (5.25 mm outer diameter).**

The ring structured fiber was designed for single mode guiding from 400 GHz up to 1.2 THz. The peak to peak images of the PE rod and the two ring TOPAS fiber clearly show a higher confinement by the inscribed structure. While for each pixel a full time domain trace was recorded, it is also possible to compare the field distribution of specific frequencies and modes.

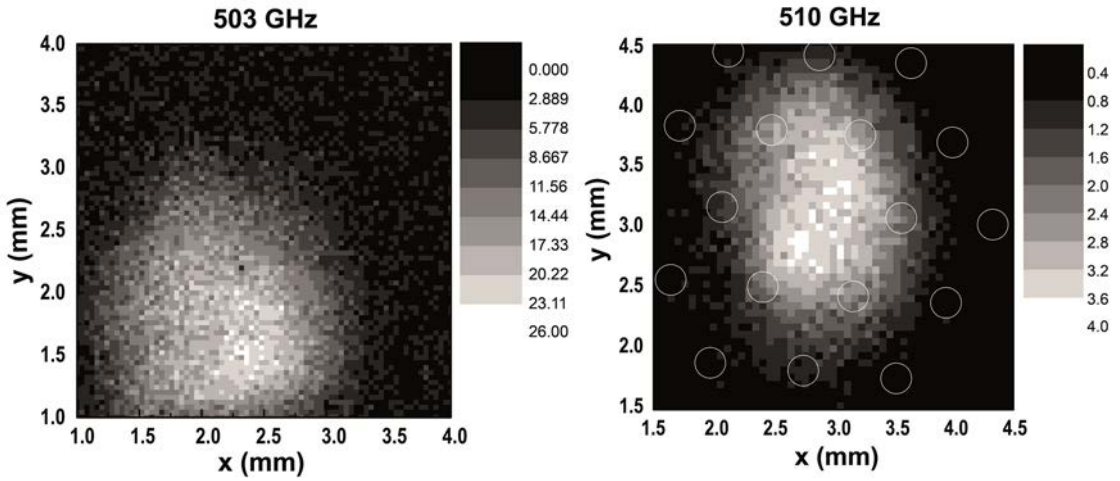


**Figure 29: Measured THz image at 503 GHz of a PE rod (left side) and a TOPAS two ring structured PCF at 510 GHz (on the right side).**

Looking at the lower end of the single mode frequency range of the microstructured fiber, here at around 510 GHz, the mode profile is compact and contains more energy within the core region. At higher frequencies the PE rod without any guiding structure present dissipates power through leakage and frequencies above are low in power. The PCF in contrast has still significant power levels across the fiber core.

### 3.3.1.2 Honey Comb and Four Ring THz Fiber Structures

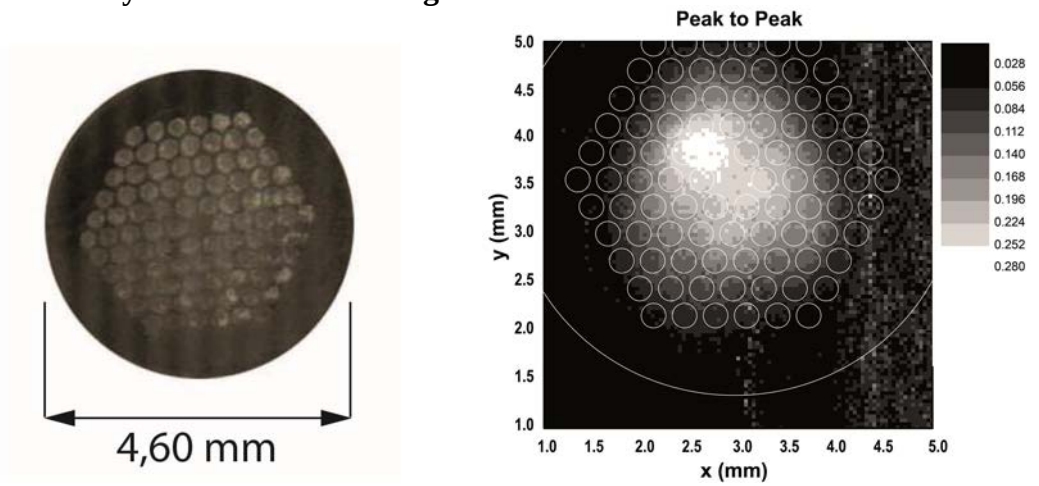


**Figure 30: Picture of a TOPAS honey comb structured PCF (4.6 mm diameter) and the peak to peak THz image.**

In a second experiment, a different fiber design was characterized by the near-field imaging setup. The PCF had an outer diameter of 4.6 mm, a hole diameter of 285 um and a relative pitch of 370 µm, which means that it can support higher order modes[60]. A photograph of the fiber's cross section and the peak to peak THz image are displayed in Figure 30. Having a look again on selected frequencies, the high-resolution images clearly show the transition to higher order modes with even two maxima at 980 GHz within this fiber.

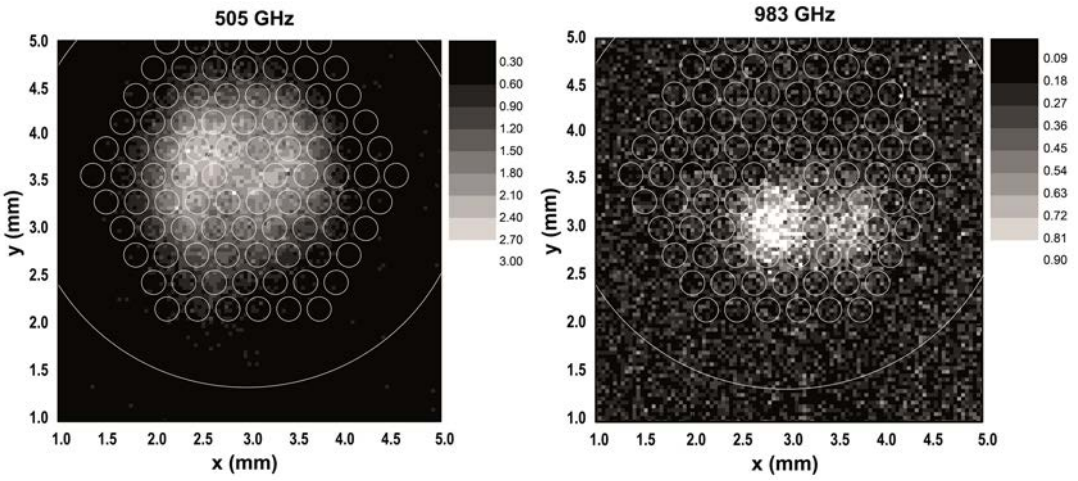


**Figure 31: THz image of a five ring honey comb structured TOPAS fiber at 505 and 983 GHz, respectively.**

These higher order modes can be excited by imperfect coupling into the fiber or through power transfer from the fundamental mode into propagable higher modes. For most applications, including spectroscopic measurements, higher order modes render the measurement results useless. That is why usual fiber designs target broad single mode guidance with negligible dispersion at best.

Another example of this undesired behavior was measured by a second PCF with a higher pitch as well. The hole size was determined to 371 µm and the pitch to 650 µm.

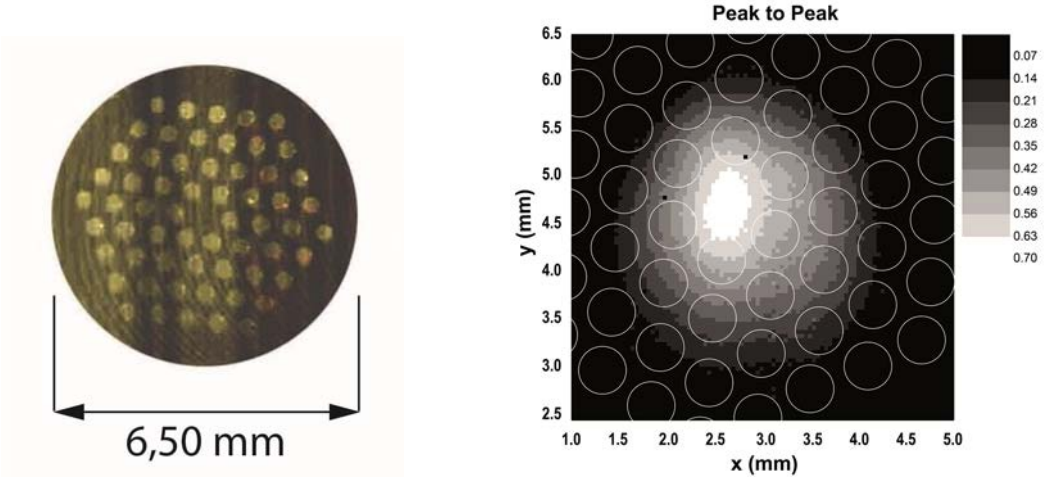


**Figure 32: Picture of a TOPAS four ring structured PCF (6.5 mm diameter) and the peak to peak THz image.**

For this hole to hole spacing ratio, higher order modes are appearing above 800 GHz (Figure 33). Especially the non-uniform shape at 900 GHz shows non-perfect coupling into the fiber. This effect leads to distorted mode fields and can lead to undesired artifacts in sensing applications relying on a THz pulses for time domain measurements.

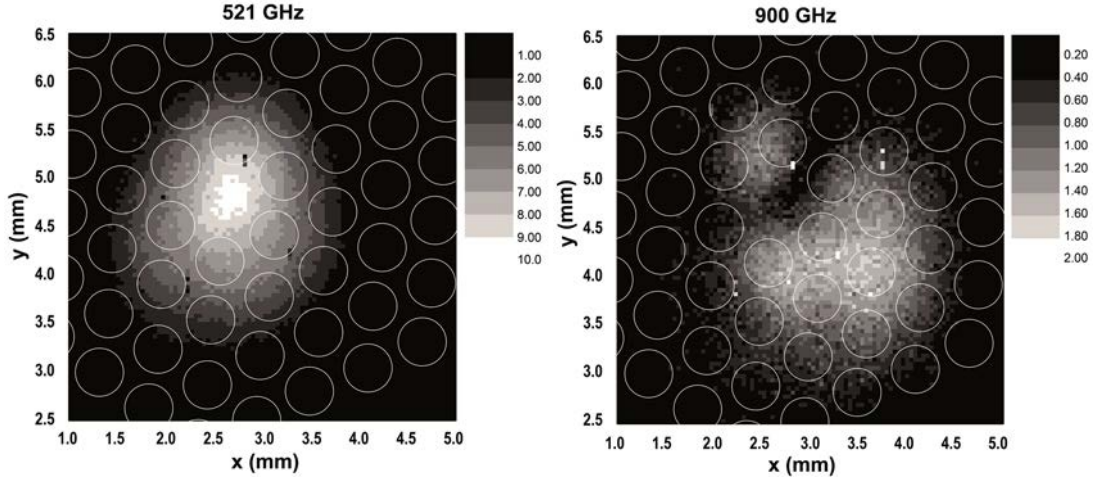


**Figure 33: THz image of a four ring honey comb structured TOPAS fiber at 505 and 900 GHz, respectively.**

### 3.3.1.3 Novel Design with Added PEG

The novel fiber design is based on a TOPAS preform with an outer diameter of 60 mm. The preform was drilled and then pulled down in the customized polymer drawing tower at DTU, Denmark (cf. Figure 18) as presented before. Typical drawing temperatures of the preform are around 200°C. The resulting THz fiber had an outer diameter of approximately 5 mm and is therefore suited to guide THz radiation. The cyclic olefin copolymer TOPAS has a nearly flat refractive index of approx. 1.525 up to 1.5 THz and a low material loss coefficient [46].

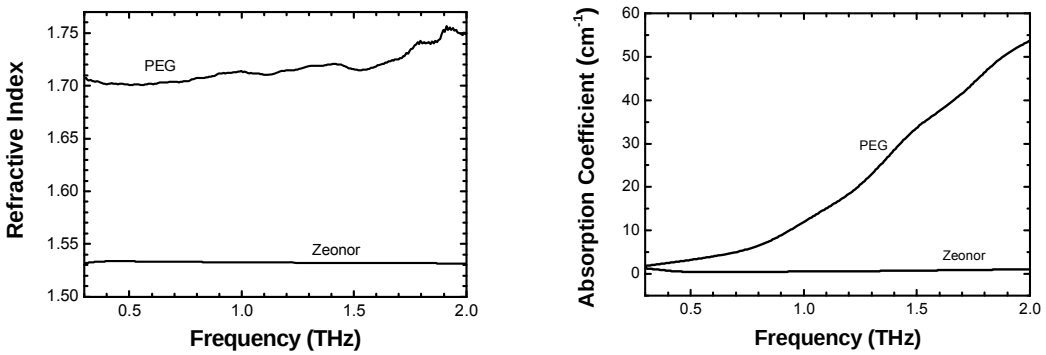


**Figure 34: Refractive index and absorption coefficient of Zeonor/TOPAS and polyethylene glycol (PEG) over frequency.**

The fundamental structure of the novel fiber design comprises a triangular lattice with a hole size of 214 µm and a pitch of 385 µm. Two pieces of the fiber were cut out and one was processed after the draw with polyethylene glycol (PEG). This special polymer was used due to its high absorption in the THz frequencies (see Figure 34) and the fact that it is softening at around 64°C. Thus, by heating up the preform and the polyethylene glycol to about 70°C allowed for filling the now fluid PEG in the outer holes with ease while the TOPAS fiber remained rigid. The additive, milky PEG can be easily checked by visual inspection due to the transparency of TOPAS in the visible.

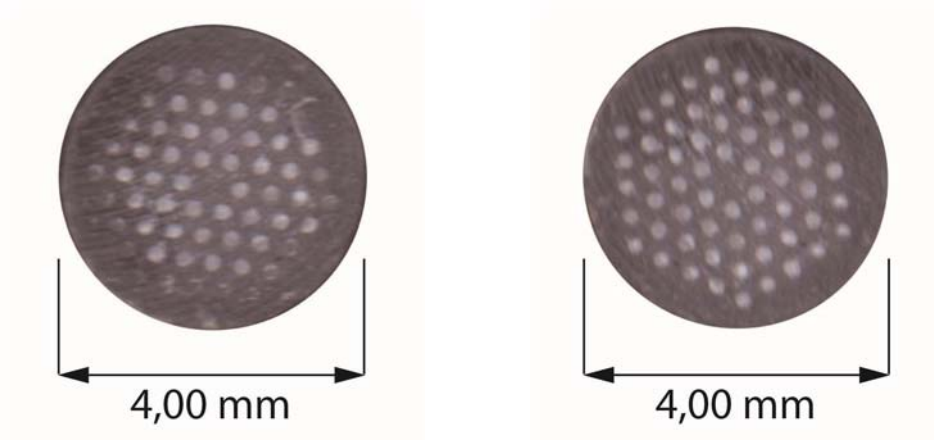


**Figure 35: Cross-section of the two polymer photonic crystal fibers with (left) and without (right) added polyethylene glycol (PEG) in the outer holes (visible as darker spots in the outer air holes).**

Simulating the resulting electrical field distributions within the fibers was performed with the above mentioned mode solver software COMSOL. It can be used to determine the number of guided modes within arbitrary physical lattices and offers their corresponding mode structures in plotted form. Figure 36shows the simulated peak intensity THz field images for the fundamental mode at 500 GHz for both fibers designs.

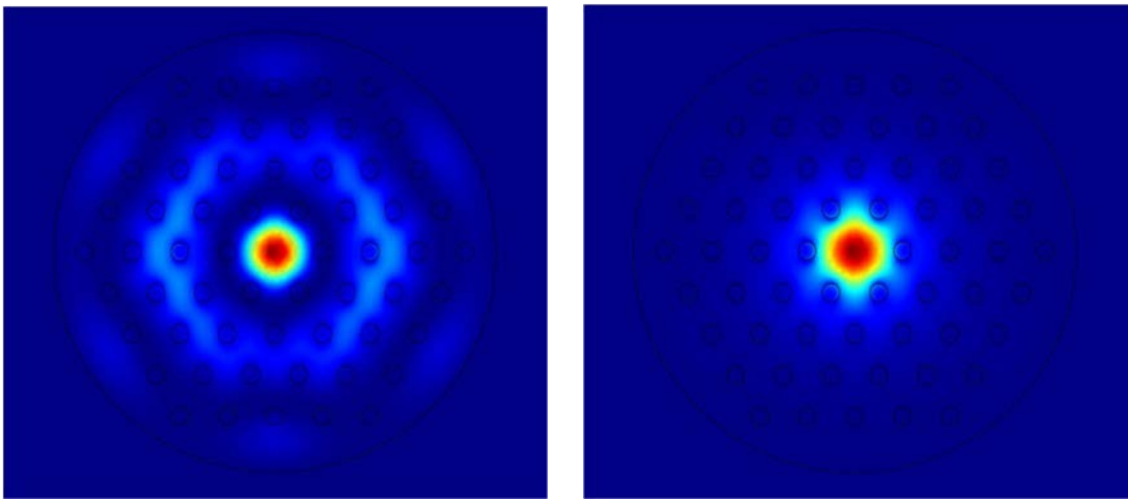

**Figure 36: Simulated THz peak intensity mode profiles in the PCF with (left) and without (right) PEG for the fundamental mode at 500 GHz.**

A more comprehensive comparison of the confinement of the modes for frequencies ranging from 0.4 to 1.0 THz reveals that the new design works perfectly for lower frequency modes which electrical field stretches out in the cladding and in the PEG. However, the fundamental modes of higher frequencies, which are mainly contained within the index-guiding core, are not affected significantly (cf. Figure 37).

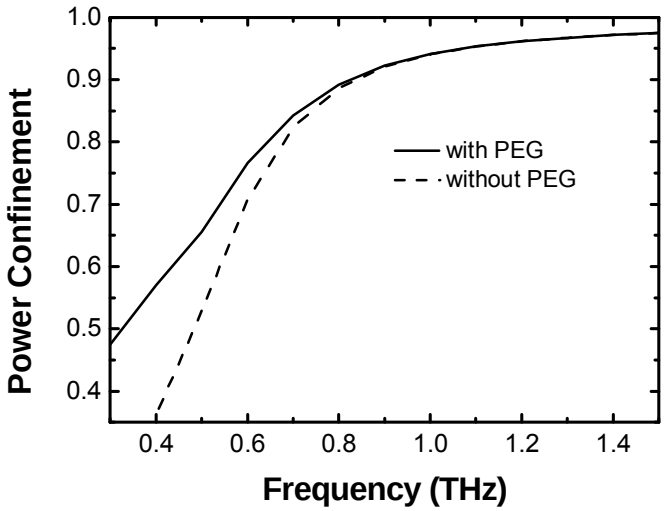


**Figure 37: Simulated fraction of guided THz power within the fiber core. (4 mm outer diameter, 215 µm hole diameter and 385 µm pitch).**

Imaging the end facet of the fiber with the near-field setup validates the simulations. The peak to peak amplitude values for comparison are depicted in Figure 38and superimposed with the fiber lattice structure to simplify the comparison. The additional PEG filling leads to a more confined electrical field distribution within the core.

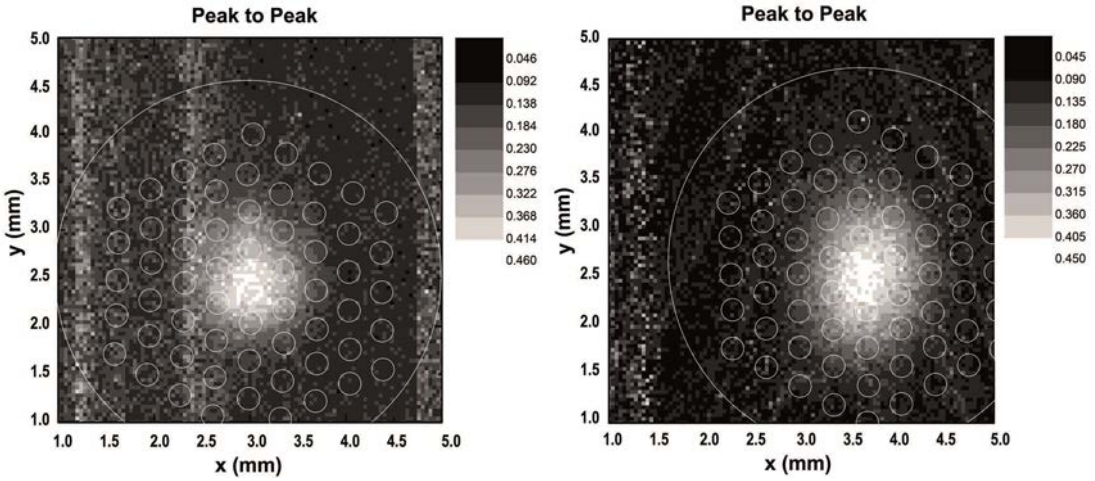


**Figure 38: THz peak to peak image of the novel design with and without PEG in the outer rings.**

Analyzing a pixel row across the THz pulse maximum and fitting the plot with a Gaussian function reveals that the full width half maximum (FWHM) value decreases with the added PEG by nearly 10% from 1.14 mm down to 1.04 mm (see Figure 39).

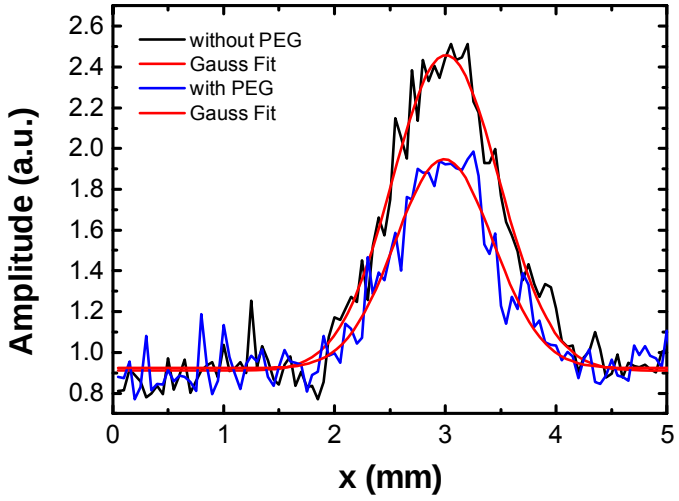


**Figure 39: Gaussian fit of the electrical field distribution for the THz fibers with and without PEG.**

According to the simulations the field confinement especially works well for frequencies below 1 THz (cf. Figure 37). Therefore the electrical field distributions at 521 GHz were checked (Figure 40).

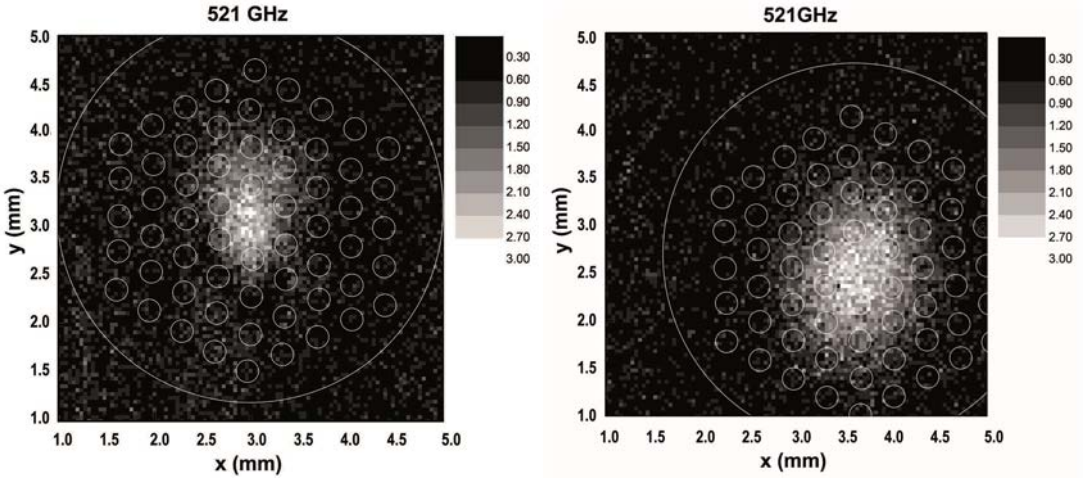


**Figure 40: THz near-field image at around 521 GHz for the THz fiber with (left) and without PEG (right).**

The added polymer also guarantees that cladding modes and higher order modes experience much higher losses and are therefore suppressed. This feature enables sensitive sensing applications without any distorted THz pulses or hazardous double pulse interferences cause by different propagation times within the waveguides.

## 3.4 Conclusions

In summary, propose a novel single mode THz waveguide design has been demonstrated, providing improved mode confinement and the ability to eliminate higher order modes from propagating. In the first part of this chapter, the general fabrication and design process of drawn polymer photonic crystal fibers was is presented. A dynamic aperture near-field imaging setup build around a fiber coupled TDS system was set up and used to characterize the mode profile in some microstructured THz waveguides. Modulating the optical excitation allowed sub-wavelength spatial resolution in the THz mode profile. Mode profile images of different THz fibers have been presented and analyzed in regards to their waveguide properties. This adapted near-field scheme may not only be relevant for new applications in near-field micro-spectroscopy but also for confining higher THz field intensities and guiding these signals to otherwise inaccessible areas.

# 4 Novel Polymer Based THz Filters

Despite the steadily growing research efforts in the last two decades, THz technology and sensing systems are far from being compact and cost-effective. Commercially purchasable products just became available recently[73, 74]. The development of compact passive devices for THz applications such as waveguides[39], filters[75], reflectors[76] and modulators[75, 77]are still in the early stages of development and will contribute to sophisticated THz systems for real world applications in the future. Like for the optical technology, where optical signal processing was done in bulk optics with all the associated problems before silica based optical fibers and fiber based components became available.

Current designs of filters for the THz range base on two different concepts: metallic meshes and dielectric photonic band gap structures (see Figure 41). Periodic wire grids or perforated metal layers in combination with dielectric substrates or spacers [78-82] can act as low-pass, high-pass or even band-pass filters. The typical fabrication process involves mechanical processing [78], deposition with a mask structure [80], lithographic etching schemes [81] or galvanization on structured substrate materials [82]. Photonic band-gap designs are well known from the optical domain [83-85]. Their periodic structure can only act as band reflectors or stop band filters. Various designs have been demonstrated by structuring silicon wafers [86], using laser machining [87], rapid laser prototyping [88] or stacking approaches [89].

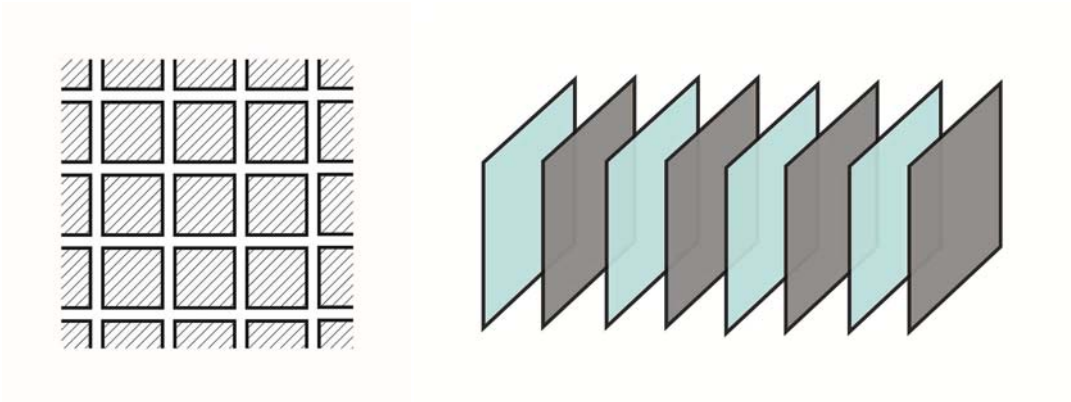

**Figure 41: Schematics of a metal grid (left) and a stacked photonic band gap structure (right) for THz frequencies.**

In this chapter a new fabrication approach is introduced in order to mass produce feature sizes below 300 µm. For sub-wavelength interaction with THz frequencies, like 1 THz, the feature size has to be smaller than 150 µm, assuming a refractive index of 1 (air). These dimensions are achieved by pulling a polymer preform in a fiber drawing tower to the desired diameters for THz applications. The photonic band-gap structure is designed and optimized by the generalized multipole technique (GMT) [90, 91].

Polymer-air photonic crystal filters have been fabricated in both polycarbonate and TOPAS and their frequency characteristics are verified in a standard THz TDS system.

## 4.1 THz Filter Design

Wavelength selective filters are well studied in the optical domain, better known as Bragg gratings [92]. These structures feature a λ/2 periodicity to obtain constructive interference for the back reflected optical wave. Each period consist of two sections with different refractive indices $n_1$ and $n_2$ but ideally the same optical thicknesses:

$$n_1 l_1 = n_2 l_2 \,, \tag{4.1}$$

with$l_1$ and $l_2$ denoting the physical length of both sub-periods. However, a slight variation of this optimum ratio doesn't have much influence on the position nor the depth of the transmission gap.

At each interface, between $n_1$ and $n_2$, a portion of the wave is back reflected and by introducing enough periods a frequency band is reflected or rather filtered out completely.

For this novel approach the photonic crystal structure, usually designed for transverse field confinement while propagating along the z-axis, is used this time for perpendicular beam propagation. A section through a schematic of the proposed 2D photonic crystal is shown in Figure 42.

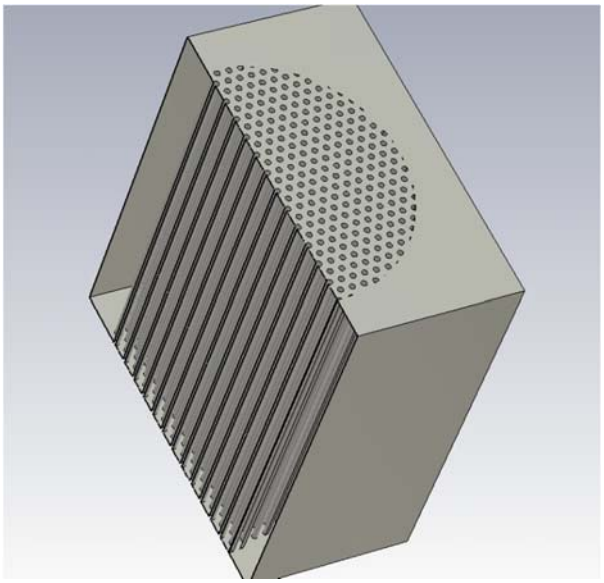

**Figure 42: Section through the 3D model of the THz filter design.**

The structure within the photonic crystal region is made of stacked tubes. The key parameters are the spacing between tubes, and the hole size after drawing (assuming interstitial regions are collapsed). This allows full control over their size and the ratio between inner and outer diameter of the stacked tubes by using the right initial tube dimensions. These degrees of freedom enable several of filter designs in the future. One variation on the theme could be the introduction of defects into the periodic structure to modify the filter response in a well-defined way, but these variations on the theme are yet to be explored.

In this work two first filter demonstrations, one made out of polycarbonate (PC) and the other from TOPAS, are presented and their frequency characteristics are simulated and afterwards verified by a standard THz time domain spectrometer.

### 4.1.1 Generalized Multipole Technique (GMT)

The Generalized Multipole Technique (GMT) is a frequency domain full-wave semi-analytical method for analyzing finite and infinite photonic crystal structures. The field distributions are calculated by multipolar functions which are separated by customized boundaries [90]. Solving the Maxwell equations for such defined regions (compare Figure 43) one obtains the field distribution across the solution domain in GMT.

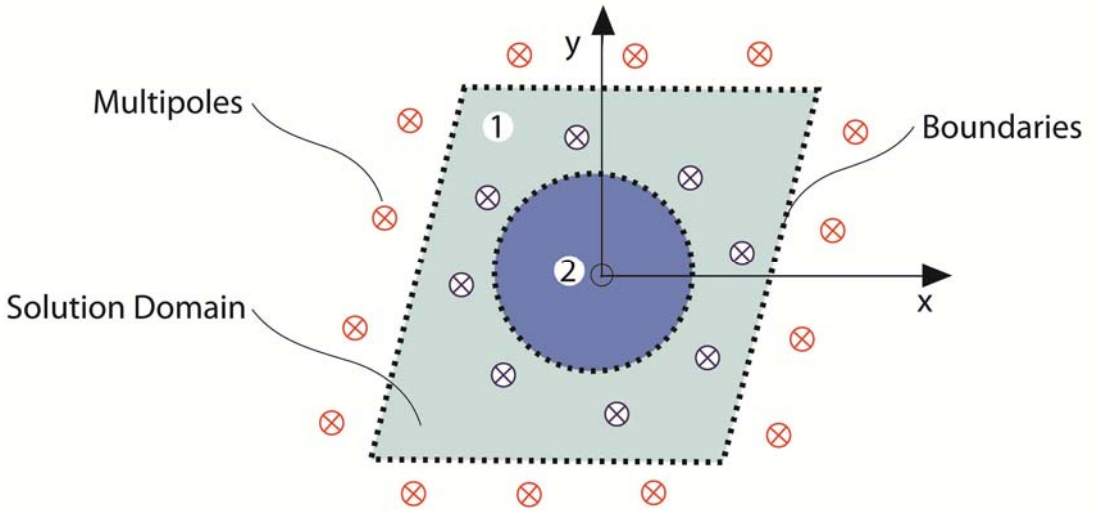


**Figure 43: Top view schematic of a typical solution domain with (1) as the exterior region and (2) the interior.**

Note that almost any arbitrary kind of boundary conditions can be modeled with the GMT. Each boundary condition is implemented as a set of discrete points, which allows for finding the unknown multipole coefficients. This leads to a linear system of equations, which is usually over-determined, and can be solved by so called singular value decomposition (SVD) [93]. All simulation data for the 2D THz photonic crystal structures were calculated by an optimized GMT algorithm developed by [94].

For the THz filters design a hexagonal unit cell with PC (n = 1.65) as the base material was assumed. Defining a unit cell and its boundary conditions, the GMT algorithm can be utilized to calculate the photonic crystal's band diagram and the mode fields. In Figure 44 the corresponding the crystal geometry together with the reciprocal lattice structure of the THz filter is shown with $D$ as the distance between adjacent holes and $D_h$ as the hole diameter.

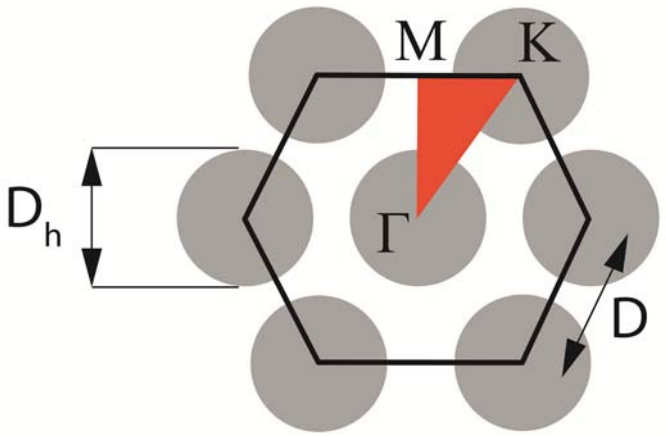


**Figure 44: Geometry of photonic crystal with the irreducible Brillouin zone superimposed (top view).**

The ratio between the hole diameter $D_h$ and the pitch $D$ was optimized for maximum suppression and the optimum value was found to be 0.745. For this fixed hole diameter-to-pitch ratio, the center stop band frequency versus the spacing of the holes can be calculated. A 1/D dependency can be seen in Figure 45.

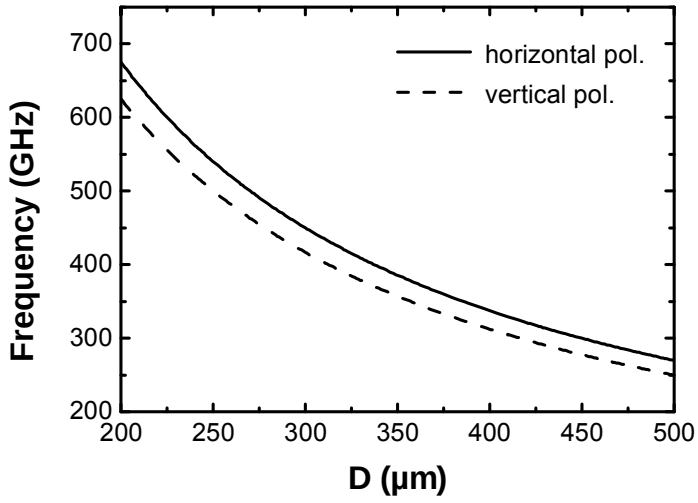


**Figure 45: Center frequency of the band gap for the optimum hole diameter-to-pitch ratio of 0.745 versus the pitch for horizontal and vertical polarization.**

The results for the simulation with the GMT for a hexagonal lattice structure with 220 µm air hole diameter and a periodicity of 300 µm for each hole is shown in Figure 3. Solid lines show the band diagram for the first two horizontal polarized modes along the air holes, the dashed lines for the vertical polarized modes perpendicular to the air hole direction.

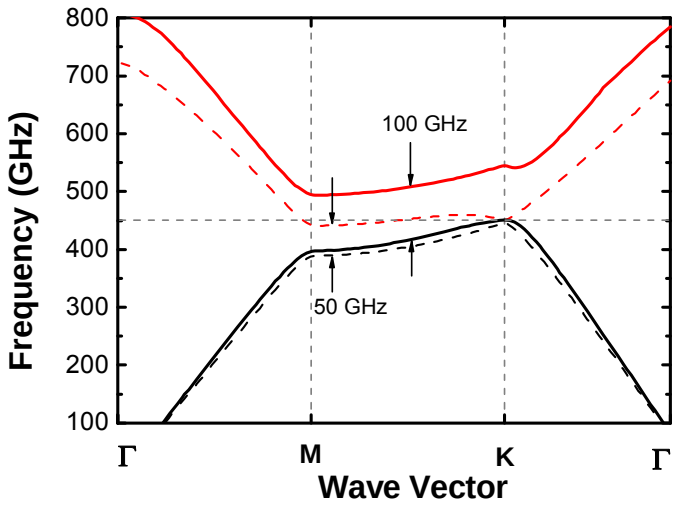


**Figure 46: Band gap diagram for a photonic crystal (base material PC, n = 1.65) with 220 µm air hole diameter and 300 µm spacing; dashed line for the vertical and solid line for the horizontal polarization.**

As can be seen the resulting band gap gained by the GMT method is located at 400 to 450 GHz for both polarizations and offers a width of 100 GHz for horizontal polarization and about 50 GHz for vertical polarization. By rotating the lattice in respect to the incident beam, a broadening of the band-stop gap can be achieved.

For fully characterizing and understanding this filter structure, a closer look is taken on the frequency dependent refractive index. An easy but not very meaningful approximation estimate of the refractive index would be to consider only one column of air holes. This would lead to neglecting the mutual interaction between adjacent holes and therefore it was chosen to use a finite number of air hole rows to calculate the effective refractive index. To visualize the effect of increasing number of air hole columns, simulation with the generalized multipole technique (GMT) for both polarizations are performed (see Figure 47).

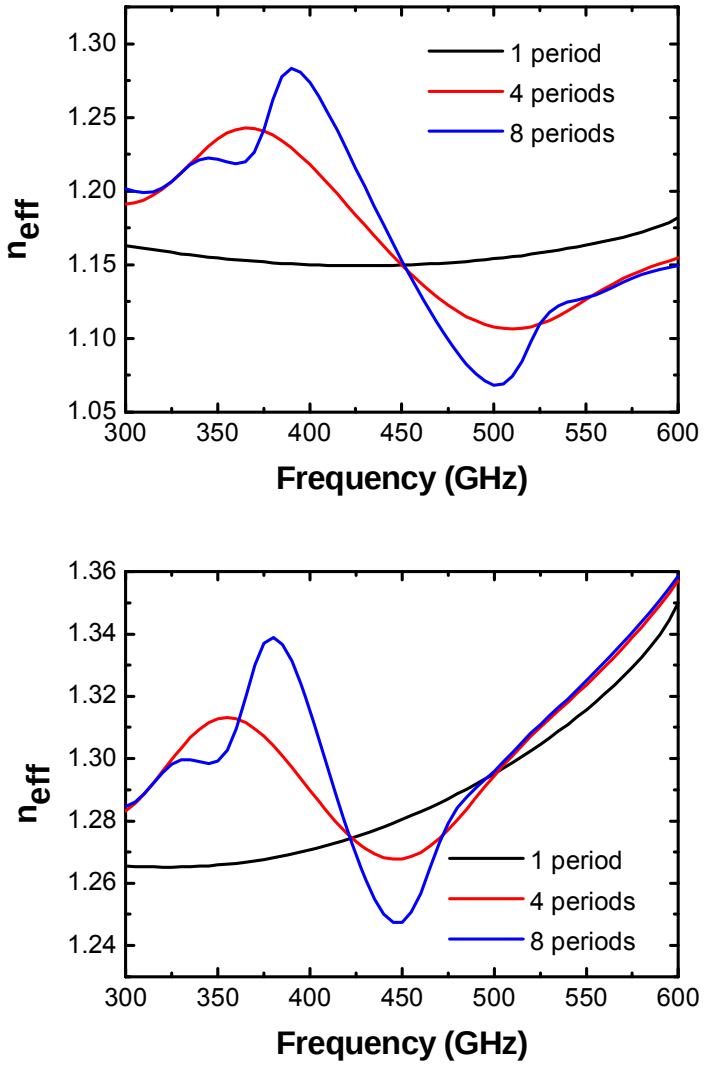


**Figure 47: Simulated effective refractive index for a) horizontal and b) vertical polarization for an increasing number of air-hole columns (1, 4, and 8) in a PC THz filter (n=1.65, D=300µm, $D_h$/D=0.745).**

Two things should be noted here. First, the photonic crystal has a significantly different effective refractive index variation for horizontal (in line with the air-holes) and vertical polarization (perpendicular to the air-holes). For both directions the periodic filter structure will have an effect, but the band stop filter will be stronger in the horizontal polarization. The second finding is that 8 to 10 periods are totally sufficient to describe the resulting refractive index behavior of photonic crystals. Increasing the number of periods yields no significantly better results, but requires more calculations and thus longer computational time.

These fundamental simulations are adequate to estimate the photonic crystal frequency response under ideal circumstances, meaning the material is considered lossless. In realty on the contrary, losses have an influence in polycarbonate, especially for higher frequencies, and can't be neglected even for low numbers of periods (cf. Figure 1 in

Chapter 3). As shown in the previous chapter, typical polymer materials used for THz applications are Zeonor, TOPAS, HDPE and Teflon (PTFE). The higher absorption of PC limits its usual application to niche THz applications.

Therefore the frequency dependent dielectric loss is included in the GMT analyzing code. The base material assumed here for the simulation is polycarbonate (n = 1.65) and considered lossy, having a varying complex permittivity. The loss tangent (*tan*(δ)), which is defined by the ratio of the imaginary part of the dielectric permittivity to its real part, is varied for the simulations to see the effect of absorption for these THz filter structures. The values are assumed for the lossless case (*tan*(δ) = 0), a low absorption rate (0.01) and for an increased absorption rate (0.1) which is close to the measured permittivity of PC.

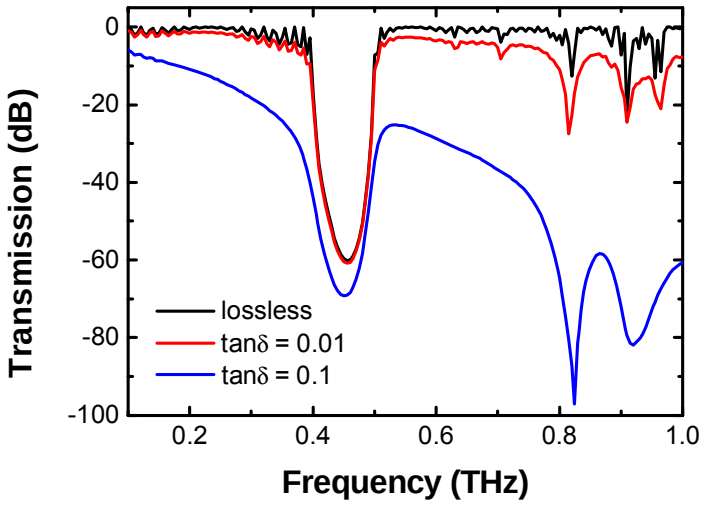


**Figure 48: Effect of dielectric absorption for three different values for tan(δ) on the transmission characteristics for a PC THz filter (n=1.65, D=300µm, $D_h$/D=0.745)**

The simulation results for all three *tan*(δ) values are shown in Figure 48. A significant decrease in the transmission spectra due to dielectric absorption is evident. As expected the loss increases with frequency. PC samples of different fabricator and charges measured in a standard THz TDS system revealed loss tangents of 0.016 – 0.02.

### 4.1.2 Fabrication Process

For photonic crystal structures to work, the feature size has to be at least smaller than half the targeted wavelength. For THz applications these feature sizes (typically below 300 µm) can't be accessed directly by mechanical drilling, which can't provide the required thin, symmetrical holes, stretching over several centimeters. Again, the fiber drawing technique can be applied to fabricate hole diameter of nearly arbitrary dimensions. A fiber drawing tower (as described in chapter 2) was used to pull down custom designed THz filter preforms. Due to practical reasons, the photonic crystal

features cannot be mechanically drilled in the preform as for the THz polymer fibers (waveguides) described in the previous chapter. Drilling through a 10 cm long preform is limited to 1 mm drills, smaller drills can't be driven into the material without deviating from the intended path nor can they transport the drilled material out of the hole. So using mechanical drilling for inscribing a hexagonal lattice with 1 mm holes into a 60 mm preform limits the possible number of photonic crystal periods to about 30. Another aspect is the time consuming preparation of the preform, which would take days to finish the drilling on a CNC machine, due to the necessary drill-picking one has to perform in order to prevent the polymer to heat up and deform or discolor. The solution is an additional draw run in order to fabricate a length of tube with sub-millimeter hole diameters, and stack pieces of this smaller tube into a second preform. This way the second preform's structure can be tailored to our needs. The preparation steps were as follows:

- Pulling a standard polymer tube (outer diameter more than a centimeter) down to 1 mm outer diameter
- Cutting the 1 mm tube in hundreds of 10 cm pieces
- Stacking these 10 cm tube pieces into a bigger second tube (approx. 3-4 cm inner diameter – cf. Figure 49)
- Second fiber draw run for reducing the stacked preform down to THz features sizes (outer diameter about 1 cm). Applying low-pressure or vacuum to close the interstitial holes between stacked tubes.

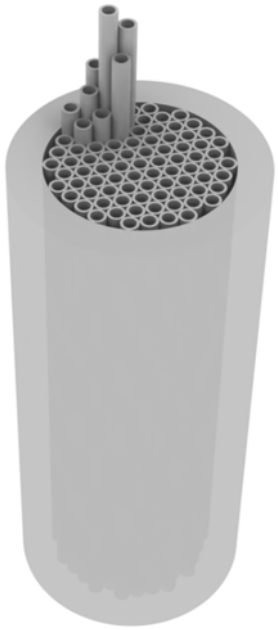

**Figure 49: Schematic of the stacking process prior to the second draw run.**

Two different polymer preform base materials were used for the THz filter fabrication. For the initial proof-of-principle fabrication runs, commercially available polycarbonate (PC) tubes were used. The first draw run was performed on PC tubes with 12 mm outer diameter and 9 mm inner diameter.

Pulling a 1 m long tube of 12 mm outer diameter results in more than 100 m length of tube with 1 mm outer diameter and approximately 0.7 - 0.8 mm hole diameter. After that the 1.2 mm tube was cut into several hundreds of 10 cm pieces. Another PC tube was used to stack the 1 mm tubes in the center hole. This way, about three hundred 1.2 mm tubes were stacked in a tube with 38 mm outer diameter and 32 mm inner diameter. Pulling this stacked preform in a second drawing run down to about 1 cm outer diameter results in hole diameters of approximately 220 µm and a pitch of 300 µm.

During the pulling process low-pressure was applied to close up the interstitial holes between the tubes. To prevent the inner holes from collapsing they were sealed off with a drop of glue or by heat-assisted cramping. A simulation drawing of the resulting THz Filter structure can be seen in Figure 50.

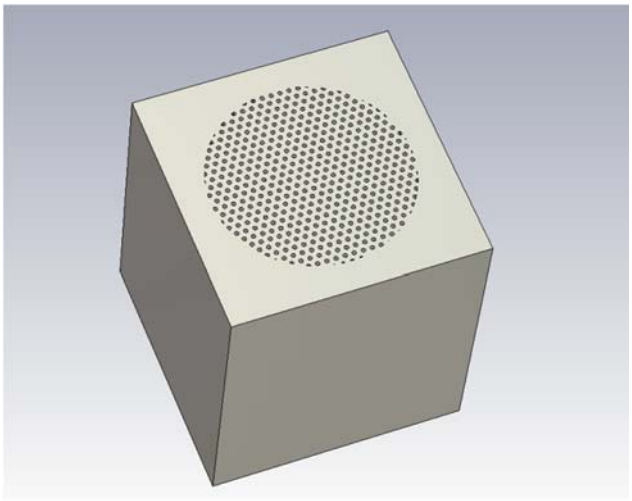

**Figure 50: 3D cubical model of the THz filter design embedded in the simulation software (GMT) with an edge length of 10 mm.**

## 4.2 THz Transmission Measurements

All investigated THz filters were characterized in a THz time domain spectrometer with a bandwidth of more than 4 THz as presented in subchapter 2.2.1. The THz time trace was measured with a Lock-In amplifier triggered by the alternating emitter antenna's bias voltage. The Lock-In was set to 30 ms integration time and to an input sensitivity of 20 µA. The pulses were delayed in 0.5 ps steps by a mechanical delay line. THz filter pieces of approximately 1 cm length were cut out of the fiber canes and placed in the focal spot of the THz beam path. The THz path was purged with dry nitrogen in order to prevent any water vapor absorption lines to distort the signal. The THz filters and their air hole structure were aligned perpendicular to the THz field. The hole structure induces a frequency stop-band which is dependent on the periodicity of the holes and the effective optical thickness of the 2D photonic crystal layers. The transmittance spectrums of several THz filters were measured. All filters reported in this subchapter were fabricated using commercially available polycarbonate tubes, and all measurements were taken with the THz beam polarized parallel to the cane axis (z – direction). Sections of the drawn PC rods were chosen with different values of pitch, and some measurements were also taken as a function of angle of incidence of the THz beam.

### 4.2.1 Polycarbonate Filters

THz filters made out of commercially available polycarbonate (PC) tubes were measured for their frequency characteristics. Their hole diameter to pitch ratio was targeted with a value of 0.75 by the initial tube used for fabricating the 1.2 mm stacking pieces. The hole diameter might slightly change during the pulling process due to non-

uniform heating throughout the stacked preform. Because the holes are not perfectly round due to imperfections in the fabrication process and due to the applied low-pressure to close the interstitial holes, they influence the measured frequency response. The non-uniform lattice results in a broadened dip with a second pronounced dip in close vicinity. Yet, these holes are sub-wavelength in dimensions and thus the only critical feature is the periodicity of the holes, which defines the specific center frequency of the stop band. The air hole diameter was measured under a microscope to be 210 µm. Two filters were measured with slightly different hole diameters targeting 400 and 450 GHz, respectively. The outer PC tube was milled down so that the cylindrical shape would not induce an additional beam distortion. A picture of the cross-section of the milled THz filter can be seen in Figure 51. Some of the inner tubes appear closed or deformed at the end face, but this is a result of cutting, and usually does not indicate a defect in the periodicity of the structure.

**Figure 51: Photograph of the PC THz filter drawn preform and a cross section of the design fabricated at USYD.**

Measuring the transmission spectrum of the THz filters in respect to a reference measurement on the empty system in a pulsed TDS system reveals the filter characteristics over a broad band of frequencies. In Figure 52 the transfer function is plotted over frequency. A clear dip in transmission is visible in the spectrum at around 400 GHz (solid line).

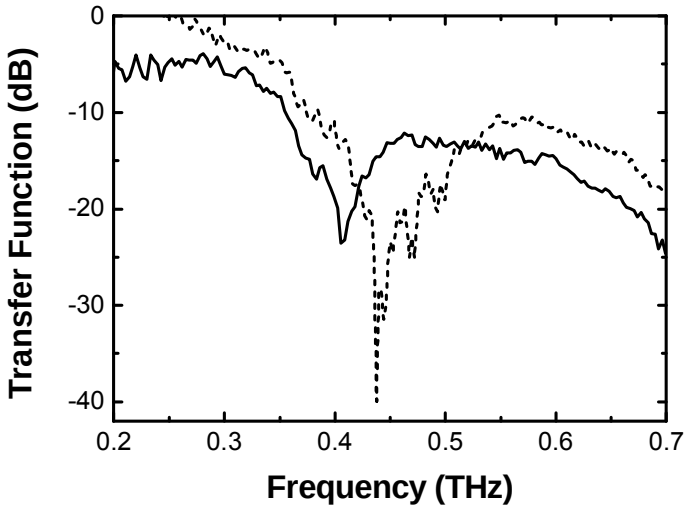


**Figure 52: Measured transfer function of two PC THz filters (dashed line is offset for clarity reasons).**

A second filter, which appears to have some inhomogeneities in its period, was measured as well (cf. Figure 52 – dashed line). The decreased diameter and hole sizes resulted in a shifted center absorption peak, the irregularities in the crystal lattice broadens the stop band. This result corresponds well with the simulated data in subchapter4.1.1. The stop band peak is more than 30 dB deep and the full feature covers about +/- 15% of the center frequency which corresponds well with simulation results (see Figure 48).

### 4.2.2 TOPAS Based Filters

For a second, improved filter design the polymer base material was changed from PC to the cyclic olefin copolymer TOPAS for allowing higher frequencies to be guided through several centimeters of polymer THz fiber with low absorption ratios. TOPAS exhibits a lower absorption coefficient than PC, especially for frequencies above 1 THz. Demonstrating the capability of the fiber drawing method to generate hole diameter of a few tens of microns, TOPAS filters targeting central stop band frequencies above 2 THz were fabricated. In a first drawing step a 60 mm preform with a 40 mm hole on the middle was drawn down to 0.8 mm outer diameter. The resulting 300 m of fiber were used to cut about 800 pieces of 15 cm length. All of these small tubes were cramped at one end to prevent the inner holes from collapsing during the second draw run with applied low-pressure. In a second preform, 60 mm outer diameter and 40 mm inner diameter, the small tubes were contained and pulled down in a second step to outer diameters ranging from 1.4 cm to 1.0 cm.

**Figure 53: Picture of the TOPAS fiber cane after the second draw run (fabricated at DTU).**

The end facet of this TOPAS THz filter was lathed rather than milled which smeared out the holes in the middle of the filter. Three 1 cm pieces were cut out of the resulting cane and measured in the Ti:Sapphire driven THz TDS system. The transfer function for each of the three different TOPAS filters can be seen in Figure 54.

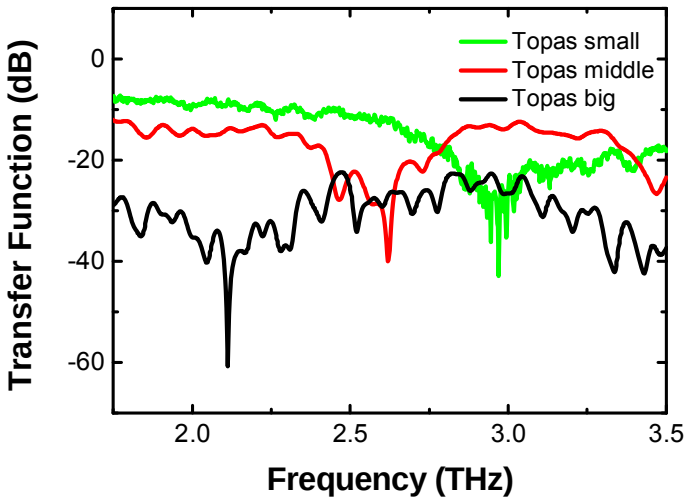


**Figure 54: Measured transfer function for TOPAS THz filters with 1.0, 1.15 and 1.4 cm outer diameter.**

Each dip is roughly 20 dB deep and a center frequency shift from 2.1 THz up to 2.95 THz can be seen for decreasing filter dimensions. The reduction in insertion loss is due to the reduced absolute filter thickness the THz pulse has to penetrate through.

## 4.3 Angle Dependent Measurement

The THz filters are fabricated in a cylindrical shape due to the fiber drawing method and the required symmetrical heating process. That means the photonic crystal induces a different frequency stop band in the incident THz pulse at different angles. In subchapter 4.1.1 simulation performed with the generalized multipole technique were used to estimate the transmission behavior. The transmission spectrum from 0° to 30° in 5° steps can be seen in Figure 55.

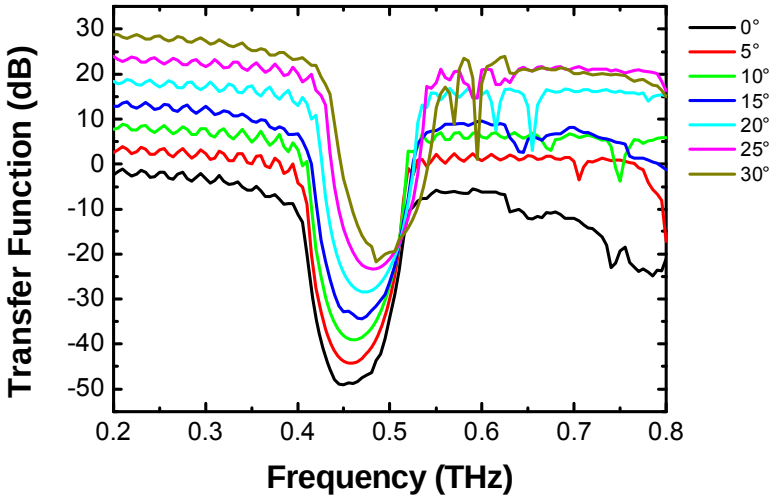


**Figure 55: GMT simulated relative transmittance at varying incident angles for a THz filter with the GMT algorithm (graphs are offset for clarity).**

A shift in the central frequency is occurring for increasing angles of incidence. In order to prove this behavior for the fabricated PC THz filter with a designed filter response at 400 GHz was set on a rotatable mount and measured in 5° steps under dry atmosphere (nitrogen flooded). Due to the long time span for these measurements, a reference trace of the empty system was taken in between. The recorded transfer functions over frequency are plotted in Figure 56.

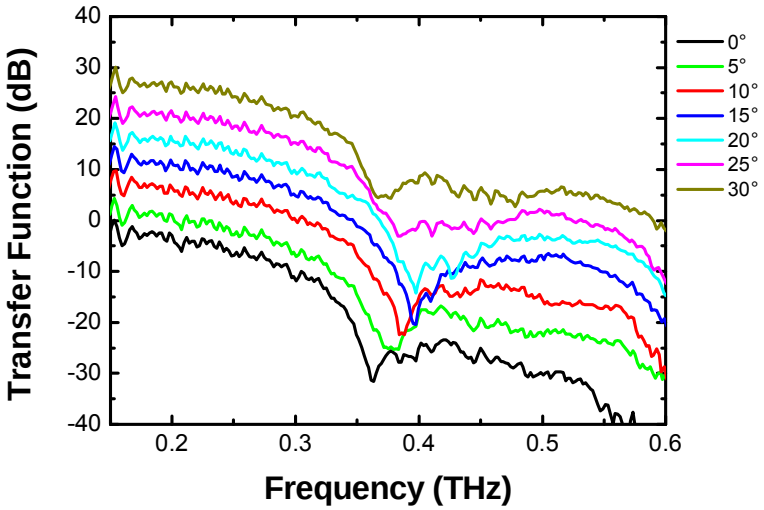


**Figure 56: Measured transfer function at varying incident angles for a PC THz filter(graphs are offset for clarity).**

Simulation and measurement are in good agreement as a shift in the center frequency can be detected. The center frequency shifts about 10% of its original value to higher frequencies. A minor broadening of the dip in transmission can be seen in the measurement as well, owed most likely due to imperfections in the lattice structure. So by varying the angle of the filter structure in regards to the incoming beam, the response can be tuned easily. This further strengthens this fabrication method's ability for offering mass production capability combined with a range of possible application fields.

## 4.4 Discussion and Conclusion

In this chapter the design and fabrication of novel polymer based filters for the THz frequency range were presented. First demonstrations of these types of filters, fabricated by the fiber drawing technique, have been investigated. Their transmission spectra were determined by a standard THz time domain spectrometer with a bandwidth of over 4 THz. These experiments were performed not with the goal of studying the physical mechanism causing the frequency characteristics but to investigate whether this method of fabrication yields suitable results for THz filters. Whilst the experimental results deviated from ideal and simulated results, especially regarding the shape and depth of the bandgap, measurements were consistent with expectations regarding the lower bandgap edge and its dependence upon pitch and angle of the photonic crystal. Variation in transmission spectra from theory were most likely due to non-uniformity and defects in the crystal lattice, which we expect could be overcome with experience and improved better fabrication techniques.

Frequency stop bands with a depth of up to 30 dB and a width of approximately 20% of the center frequency were realized with the fiber drawing method. This novel approach offers a cost effective and fully scalable fabrication process for fabricating customized photonic crystal structures in polymer.

The photonic band gap diagram and optimum fabrication parameters have been simulated and verified by my experiments. The angle dependent frequency response is measured with the THz TDS system as well.

One can imagine to use these filter structures as switchable band pass filters for THz radiation by filling the air holes with a liquid crystal (LC). LCs exhibit a birefringence for THz frequencies depending on their orientation in respect to the THz polarization. Switching them from an aligned to a perpendicular position by applying a strong electrical field, the photonic crystal structure can possibly vanish. For a first tryout a LC with refractive index of 1.61 in the ordinary and 1.49 in the extra ordinary polarization was chosen to match the refractive index of PC (n = 1.65). Unfortunately, due to the lower refractive index difference in the “on” state in comparison to PC, $\Delta n = 0.16$, rather than 0.65 with air holes, the dip in transmission could not be seen clearly. The fact that only limited numbers of periods are available limits the possibilities of improvement further. So the only way is to find a LC with a higher birefringence. Such LCs are about to be available in the THz soon. First test samples provided to our group were measured and a birefringence of up to 0.33 was found (cf. Figure 57) [95].

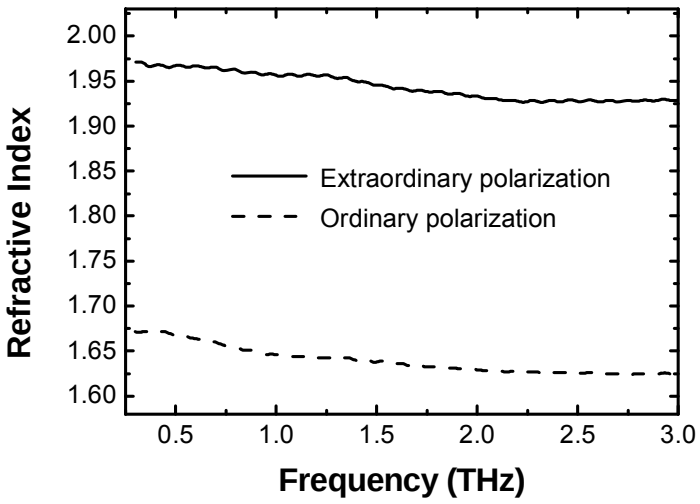


**Figure 57: Refractive index for the ordinary and extraordinary polarization of a liquid crystal with a high birefringence[95].**

The refractive index of typical LCs stretches from 1.4 up to 1.96in the THz range, which would invert the index contrast between material and LC-filled holes for most base materials. Therefore the ideal low-loss material for such switchable filters would be silica based glasses with a refractive index of approx. 1.96 for THz frequencies. This

new switchable filters will further mature THz technology and could provide the needed ability to selectively filter out specific frequency bands in the THz range. This will enable sophisticated THz telecommunication applications in the future network systems.

# 5 THz Generation from Multi-Frequency Laser Radiation

Even though terahertz (THz) technology has been on the rise for the last decade, there is no commercial, mass-market product available yet. Available THz spectrometers are still in the price range of more than 100.000$ and not in a compact and portable design. The high potential and applicability of THz radiation was demonstrated for various areas, like material analysis of semiconductors [96], characterization of elastomers and polymers [97], as well as sensor systems in the food[13] or paper and wood industry [98]. Another promising field of usage is at airport security checks, where THz technology enables non-destructive and safe testing of equivocal and possible hazardous liquids or materials in bottles or other containers [14]. So called “body scanners” have been used a probationary status and their reliability of detecting hidden objects beneath cloth will be evaluated in the near future. The biggest drawback to date is the lack of cost efficient, compact and robust lasers to drive these THz sensor systems in real world environments.

So far most laboratory laser systems with their high complexity and dimensions are only gradually suited for a semi-mobile operation with repeatable measurement results. Yet, a stable and reliable sensing operation is necessary to identify possible threats or detect unwanted substances. Scheller et al. presented a possibility to overcome these drawbacks by employing a multimode laser diode in their THz setup in 2009 [4]. The theoretical fundamentals were investigated in the 60’s, where multimode optical mixing for microwave generation was predicted and also extended to higher frequencies if adequate mixing materials would be available. In 2000, Japanese researchers [16] demonstrated the first multimode THz system. Yet, the detection scheme was based on a thermal detection (bolometer) and the laser diode in use had non-specific mode spacing which led to THz frequency components of varying intensity and more or less random distribution across the system’s bandwidth.

Like a continuous-wave THz spectrometer, the quasi time-domain spectrometer bases on photomixing on a photoconductive antenna structure. But instead of mixing two optical laser lines from two different single mode laser diodes, the new approach relies on the mixing of several cavity modes emitted by one broadband semiconductor laser diode. The detected THz time domain signal exhibits a pulse like shape similar to a time-domain spectrometer signal and is therefore called quasi time-domain spectrometer (QTDS).

In this chapter the QTDS systems are used for imaging applications and a novel combined system approaches are presented. At first the common operation of a QTDS system and the theory behind it is laid out in detail. Acquired measurement data is presented and the advantages and disadvantages of QTDS spectrometers are discussed

in brief. Experimental data on different dielectric samples measured by a QTDS spectrometer and QTDS imaging results are depicted. As a first combined system a hybrid setup consisting of a CW THz spectrometer and a QTDS system is demonstrated with the original author of the QTDS scheme. The new system offers the spectral brightness of CW THz spectrometers and overcomes the 2π ambiguity for absolute thickness measurements. The second new system approach, set up and operated by myself, combines two multimode QTDS laser diodes which have a slightly different center frequency and therefore allows generating THz frequencies well above the spectral bandwidth of a single QTDS diode. Two auxiliary laser diode models were used to demonstrate dual QTDS operation.

The chapter will conclude with an outlook on the future of low-cost and portable spectrometers.

## 5.1 Photomixing of Multiple Laser Modes

The general principle of photomixing was introduced and discussed in chapter two. A closer and more comprehensive look will be presented in this paragraph on extending the regular two laser modes photomixing to multiple laser modes.

Employing a multimode laser diode, with a spectral bandwidth of around 2 nm, leads to several laser modes to be guided to the photoconductive antennas. Typically these broadband diodes emit more than 40 cavity modes with varying optical power. Similar to the case of two colors mixing, one can extend the formulas to multiple frequencies mixing. Instead of splitting the incident optical power in two modes, it is now divided up on all supported cavity modes *M*:

$$P_{Opt,E} \propto [E_1 \sin(\omega_1 t + \varphi_1) + E_2 \sin(\omega_2 t + \varphi_2) + \cdots + E_M \sin(\omega_M t + \varphi_M)] \,. \tag{5.1}$$

Where $E_i$ denotes the amplitude of the corresponding laser mode and $\omega_i$ its angular frequency.

Due to the quadratic dependency between the optical power and the incident electrical field, there are several resulting mixing products generated: the harmonics for each optical frequency, as well as the sum and difference frequency for each pair of optical modes. As discussed in subchapter 2.3, due to the low-pass characteristics of the photoconductive antenna only the difference frequencies are supported and therefore only these mixing products are considered for the generated THz field:

$$E_{THz}(t) \propto \sum_{i=1}^{M-1} \sum_{j=i+1}^{M} \omega_{ij} A_E(\omega_{ij})\, E_i E_j \cos(\omega_{ij}\Delta t + \varphi_i + \varphi_j) \quad . \tag{5.2}$$

With $\omega_{ij}$ denoting the corresponding angular difference frequency and $A_E$ representing the spectral efficiency of the emitter antenna. Note that the cavity modes of the laser diode are not in any phase relation to each other and therefore the generated THz frequencies have random phases as well. But due to the coherent detection by the same optical mode mix in the detector antenna this arbitrary phase term cancels out and a fix DC current value can be detected for a certain path length difference ΔL. Due to this phase cancelation the recorded time trace reflects a pulse like shape, but in fact there is no real THz pulse emitted or detected. The induced current on the detection side results from the integration of the incident THz electrical field with the modulation of the conductance $G_R$ in the detector antenna induces by the same optical modes:

$$I_R(\Delta L) = \int_{-\infty}^{\infty} E_{THz}\left(t - \frac{\Delta L}{c_0}\right) G_R(t)\, dt. \tag{5.3}$$

This quasi DC detection averages over the induced fast oscillating current components [99] and by taking into account the spectral receiver antenna characteristics $A_R$ the photocurrent is given by

$$I_R(\Delta t) \propto \sum_{i=1}^{M-1} \sum_{j=i+1}^{M} \omega_{ij} A_E(\omega_{ij})\, A_R(\omega_{ij}) P_i P_j \cos(\omega_{ij}\Delta t), \tag{5.4}$$

where $\Delta t = \frac{\Delta L}{c_0}$ represents the induced time delay between emitter and detector path.

The number of resulting THz frequency components increases quadratically with the number of optical modes *M* and therefore the power for each THz line decreases. To overcome this reduction in spectral brightness and to provide a better signal to noise ratio a laser diode with equidistant mode spacing is chosen which leads to a reduction in THz frequencies to M-1 THz modes. The resulting time domain signal comprises a periodic pulse like shape with the time spacing $t_{pulse}$, determined by the inverse mode spacing:

$$t_{pulse} = \frac{1}{\Delta f} \quad . \tag{5.5}$$

Applying the fast Fourier transformation over the whole time trace, leads to a comb like spectrum with fixed frequency spacing (cf. Figure 58).

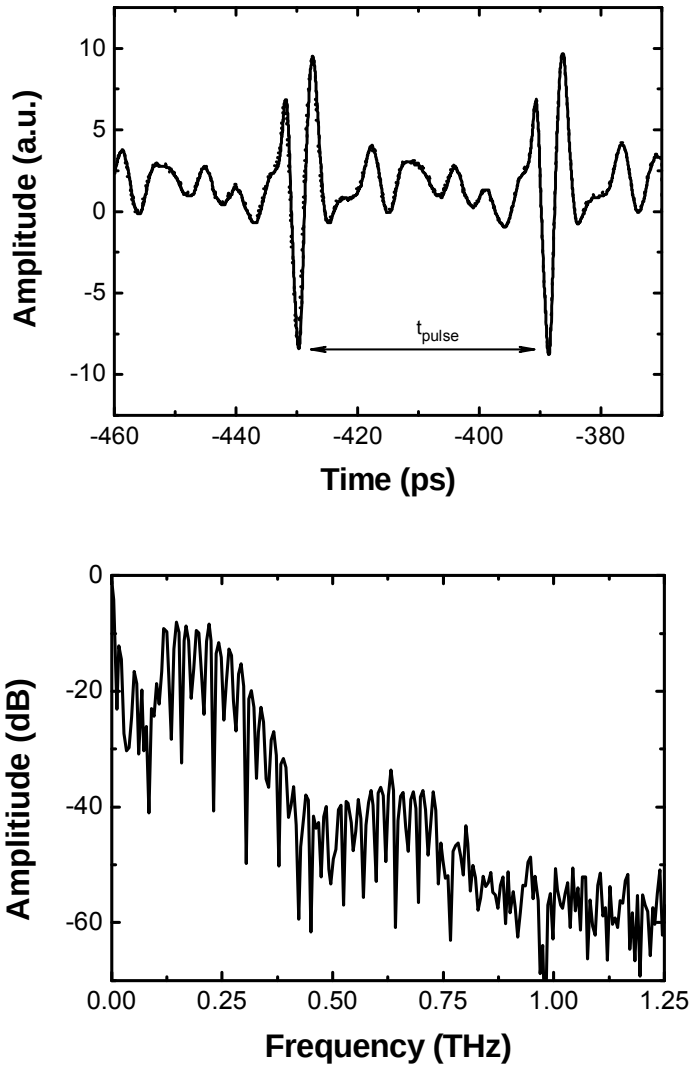


**Figure 58: A comb-like spectrum is generated by photomixing equidistant optical laser modes.**

The measured signal can now be interpreted as a regular time-domain spectrometer trace and allows for determination of absorption and refractive index at the same time with a given thickness or specialized analyzing tools [100]. This special case of time-domain spectrometer is therefore called quasi time-domain spectrometer (QTDS), which is based on CW optical generation and a higher THz mode spacing in the tens of GHz rather than the theoretical 100 MHz as for standard femtosecond laser driven TDS spectrometers. Note, there is a limitation to the maximum delay one can detect unambiguously, determined by the pulse spacing $t_{pulse}$.

## 5.2 Experimental Setup

While regular TDS setups are built around expensive femtosecond lasers, the QTDS approach relies on a low-cost multi-mode laser diode with an emission bandwidth of around 3 nm which equal a frequency bandwidth of ca. 2 THz. These laser diodes are available in standard three-legged knob layout or a common laser pointer can be used. A red laser pointer with 100 mW output power at 661 nm was chosen for the setup and the beam was guided over a beam splitter and a mechanical delay line in one optical arm to the two semiconductor antennas (cf. Figure 59). As only the difference between the optical modes is of importance and not the absolute frequencies, there was no need for a temperature controller.

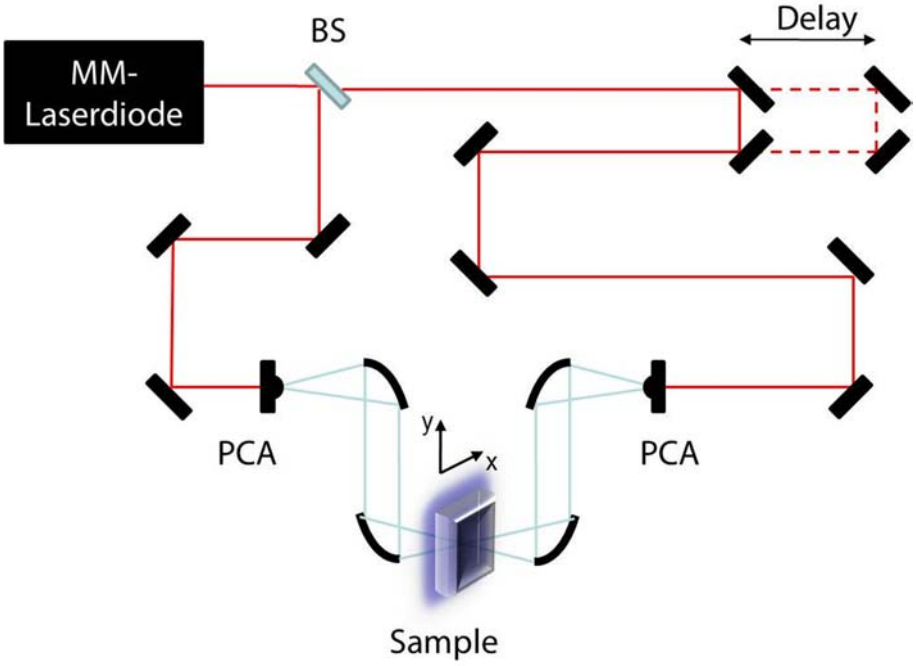


**Figure 59: Schematic of a standard QTDS setup with imaging stage in the THz focal plane.**

The laser diode mode spacing is defined by the resonator length of the diode and can be calculated by equation (5.6):

$$\Delta f = \frac{c}{2 n_{eff} L_{cav}} \tag{5.6}$$

Where $n_{\mathrm{eff}}$ denotes the effective refractive index seen by the cavity modes and $L_{\mathrm{cav}}$ represents the cavity length. The optical spectrum of the multimode laser diode can be seen in Figure 60.

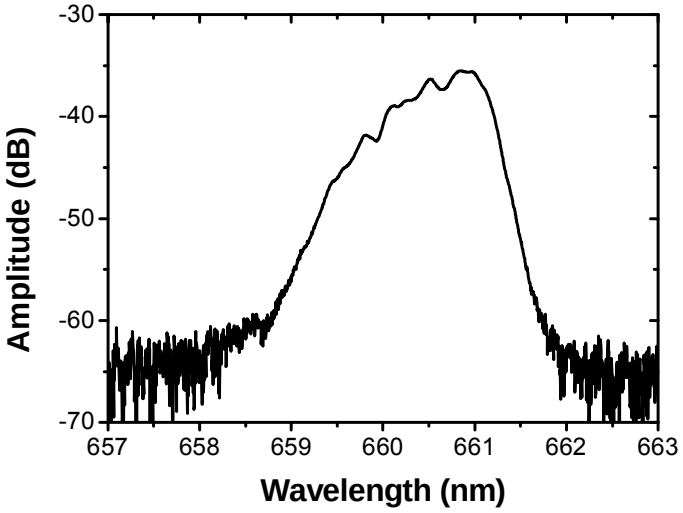


**Figure 60: Optical Spectrum of a QTDS diode.**

The data acquisition is carried out with a Lock-In amplifier which is triggered by the modulating voltage applied to the emitter antenna with a frequency of around 4 kHz. The antenna is biased periodically with +/-20 V.

The comb structure in the frequency spectra, which is determined by the cavity mode spacing $\Delta f$, leads to a periodic time domain signal [101]. By reducing the measurement window in the time signal to one pulse length $t_{pulse}$, the spectrum becomes continuous (Figure 61).

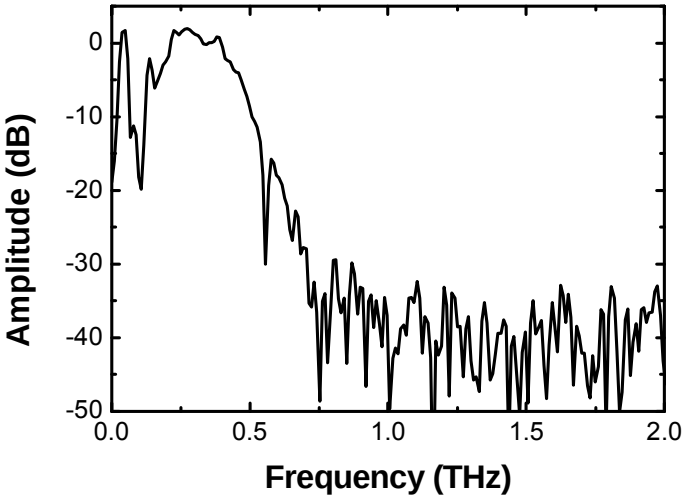


**Figure 61: THz spectrum of a QTDS system.**

The system offers a bandwidth of about 400 GHz and a signal to noise ratio of approx. 40 dB. The QTDS approach is perfectly suited to observe general absorption variations over a broader range of frequencies and measure thickness and refractive index at the

same time [100], but has its limitations when it comes to detecting narrow absorption lines like for gas sensing [102]. An example measurement is shown in Figure 62, where the dotted line displays the measurement of the sample and the solid line represents the reference measurement without a sample present. Two effects can be seen clearly, a time delay induces by the reduced speed of propagation as well as an attenuation of the peaks amplitude. Both information can be analyzed like in regular TDS systems and yields the refractive index and absorption coefficient of the sample under investigation. If Fabry-Perot echo pulses can be detected as well, it is also possible to extract the thickness simultaneously, but that requires a thick sample to separate the echo pulses from the main pulse[7].

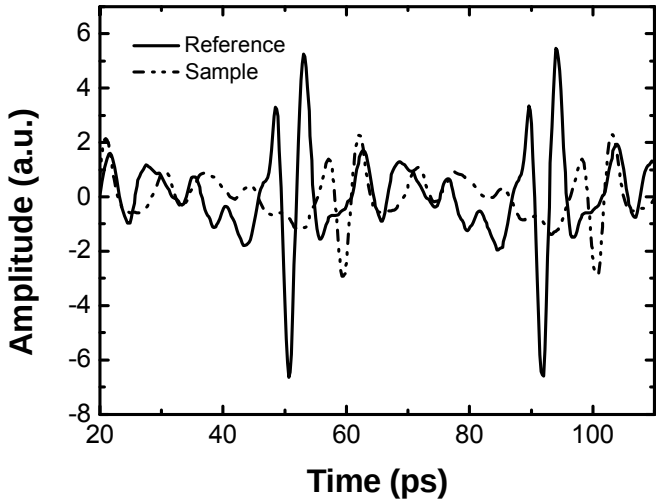


**Figure 62: Time traces of a reference THz pulse and a pulse passing through a sample.**

In order to perform sophisticated imaging measurements the stability of the laser diode needs to be verified. Whereas the absolute wavelength is not a concern for the photomixing efficiency, the power distribution between the cavity modes is. Several measurements taken over hours show that there is no significant deviation between the time domain data (cf. Figure 63).

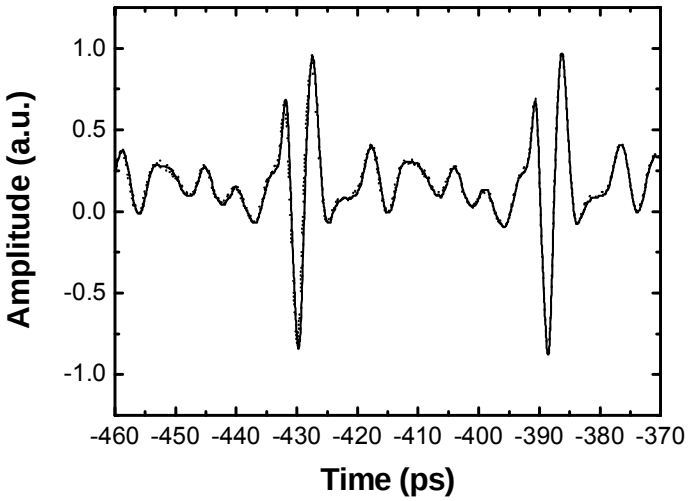


**Figure 63: Signal deviation monitored over several hours.**

## 5.3 QTDS for Imaging Applications

In this subchapter the potential of quasi time-domain spectroscopy (QTDS) is assessed in terms of imaging and inspection applicability. A standard QTDS system is used for generating THz images in the time and frequency domain. These methods are well known from TDS [103, 104]and CW THz setups [105, 106]. For industrial application and quality inspection it is necessary to resolve spatial changes in material parameters and varying sample thicknesses.

The QTDS spectrometer setup is now extended by an x-y translation stage, which can be mounted with the sample under investigation (presented in Figure 59). By stepwise moving the sample through the focal spot, a full time trace for each pixel is recorded. The important value for each pixel is the peak to peak (p-p) amplitude, which corresponds to the absorption, and the absolute time delay of the pulse in regards to a reference measurement. Both values are an indicator for the thickness and the refractive index of the samples at a specific position. By assuming a uniform refractive index across the sample, the absolute peak position can reveal thickness variations very precisely.

**Figure 64: Photograph of a polymer airbag cover.**

First a THz image of a plastic airbag cover with a predetermined breaking point was mounted on the x-y imaging stage. A photograph of the airbag cover is shown in Figure 64. The breaking line clearly visible by the human eye can also be identified in the THz image by a shorter delay of the measurement pulses due its thinner thickness. As the feature size is below the focal spot size, the THz radiation travels through differing portions of polymer material. Thus, a double pulse signal in the time domain is detected which represents one part of the pulse propagating through the thin breaking line and the other part through the thick standard airbag cover. Such a double pulse time trace can be seen in Figure 65.

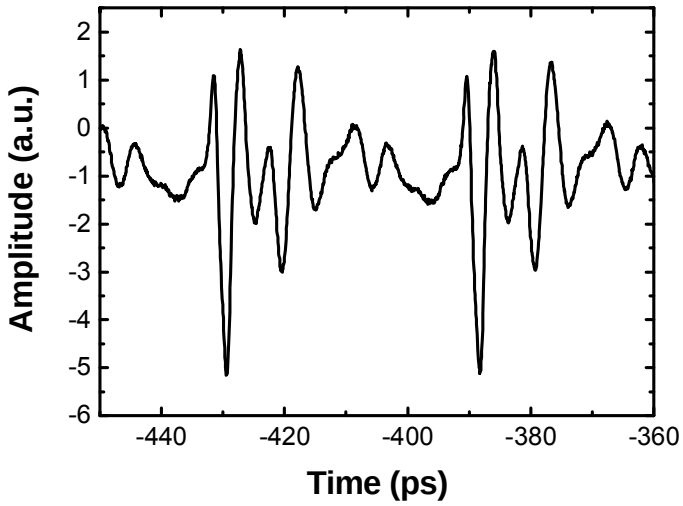


**Figure 65: Time domain signal of a THz pulse passing through the breaking line and the adjacent polymer material resulting in a double pulse structure.**

This feature enables us to simultaneously extract the thickness of the breaking line and the base polymeric material by comparing the induced time shift to an air reference measurement. Note, that this again only works smoothly for well separated pulses. The resulting raster scanning THz image with 140 x100 pixels and a 0.5 mm step size is

presented in Figure 66. The breaking line is clearly visible in the peak-to-peak values, which is a good indicator due to the reduced amplitude when a double pulse is detected.

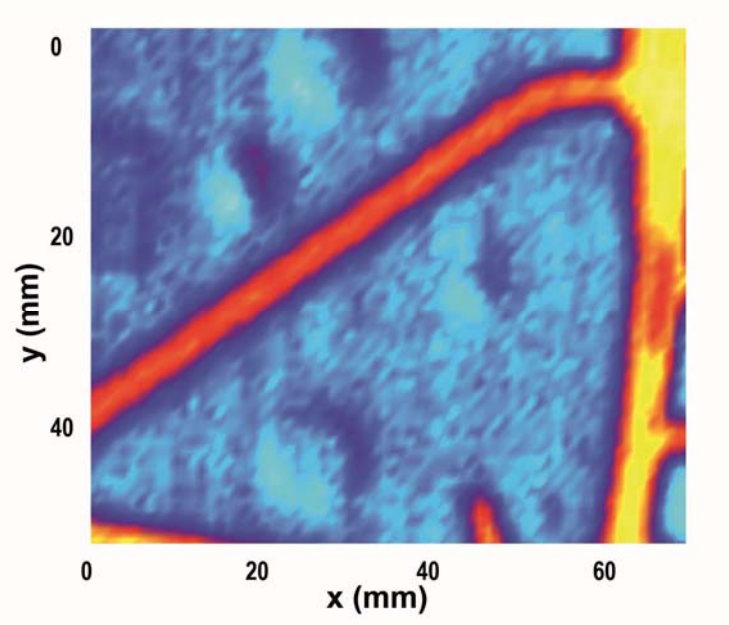


**Figure 66: THz image of the airbag cover.**

The second sample was a piece of polymer sheet with foreign bodies included. The polymer slab was 4 mm thick and made of extruded polyethylene (PE). During the fabrication process inclusions were put in the injection mould deliberately. The change in absorption and refractive index by the defilements leads to a change in amplitude of the THz signal and causes a time delay of the pulse. Again, an image with 0.5 mm raster steps was taken of the PE sample, resulting in a 40 x 46 pixel image which is shown in Figure 67.

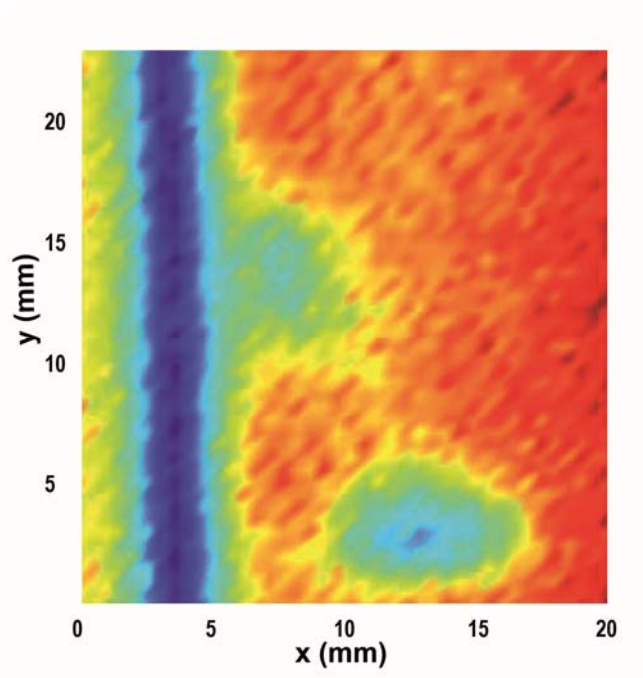


**Figure 67: QTDS THz image of a PE slab with defilements.**

The maximum amplitude value was taken to indicate the absorption at that specific point of the sample, relating back to the thickness of the material. The SNR was the same as for the standard QTDS system in the range of 40 dB. The foreign inclusions can be clearly detected by the QTDS imaging, even thou the smallest feature size is only 1 mm. Thus, quasi time-domain spectrometers offer a great potential for cost effective industrial monitoring tools to control and determine inclusions, thickness, composition ratios and spectral features of numerous materials.

## 5.4 Hybrid Continuous Wave Spectrometer

In the previous two subchapters it was shown that QTDS can substitute regular TDS systems for many applications. Yet, it suffers from a relatively poor frequency resolution which is dependent on the optical mode spacing of the multimode laser. It also has its limitations in comparison to a standard tunable continuous wave (CW) spectrometer, due to its low spectral brightness. On the other hand, the biggest drawback for a CW system is the ambiguous phase information which usually eliminates the possibility of thickness determination.

In the following paragraphs a novel hybrid system approach is presented, to overcome the 2 $\pi$ ambiguity of CW THz spectrometers by keeping their spectral brightness at the same time. The new approach bases on a multimode laser diode and two tunable DFB laser diodes (CW THz Spectrometer). As THz signals only add a detectable signal in the photoconductive receiver antenna, when the THz wave was send out by the same laser

modes (coherent detection), it is possible to generated multiple THz signals simultaneously in one THz antenna pair without interfering with each other. In order to prevent photomixing between the two laser beams, their wavelengths are chosen with a far enough spacing (approx. 200 nm). Another possible approach would be to use orthogonal polarizations for each laser beam. In our case, both laser beams are superimposed through a dichroic mirror, reflecting above 800 nm and transparent for 660 nm (cf. Figure 68). The combined signal is then split by a beam splitter (BS) and guided to both antennas. The CW THz system is operating at 850 nm and the QTDS laser diode, emitting at 660 nm, was the same as in the previous subchapter.

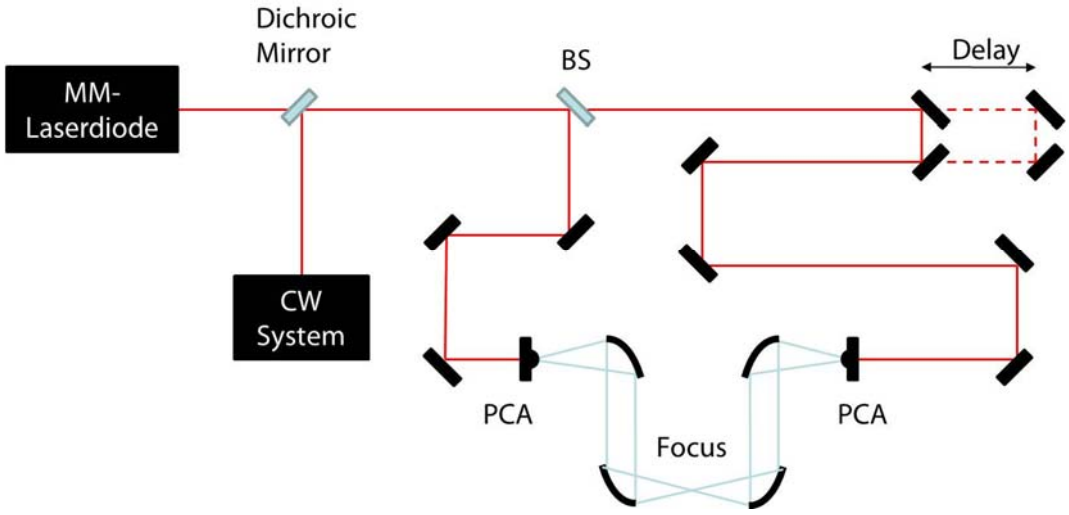


**Figure 68: Schematic of a standard QTDS setup.**

The resulting THz time domain signal is build up from the sum of each single THz signal, the pulse train for the QTDS signal ($I_{\mathrm{QTDS}}$) and the pure sinusoidal, tunable signal ($I_{\mathrm{CW}}$) generated by the DFB lasers.

$$I_{reciever}(t) = I_{QTDS}(t) + I_{CW}(t) \tag{5.7}$$

In Figure 69 are the time traces for each individual system and the combined hybrid signal displayed. On the right side the corresponding spectra are shown. The higher spectral brightness of the CW signal can be seen in the frequency domain, which offers a much higher signal to noise ratio for measurements at that frequency. This enables precise sample characterization with the CW signal and overcoming the 2π uncertainty of the thickness measurement by analyzing the pulse delay of the QTDS signal.

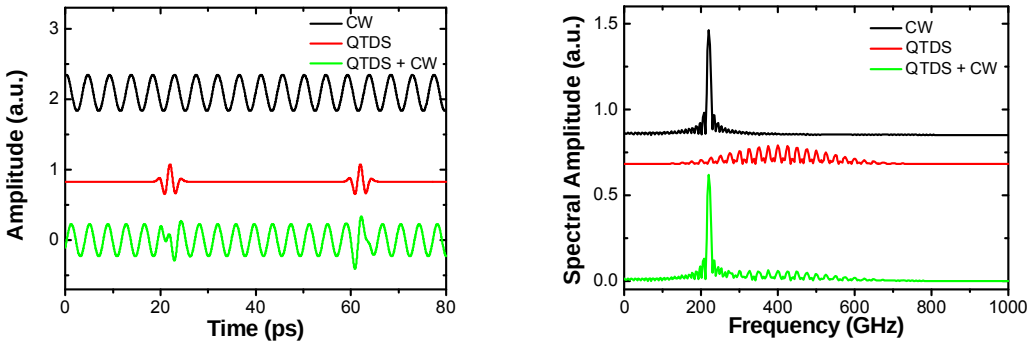


**Figure 69: Time domain and frequency domain signals for the combined hybrid system and for each individual system.**

To show the hybrid system's versatility, the DFB lasers were tuned in regards to each other and varying mixing frequencies were monitored. Hybrid signal traces of increasing CW THz signals are presented in Figure 70. The amplitude of the CW signal reduces with higher difference frequencies due to the decreasing antenna efficiencies (cf. time and frequency traces).

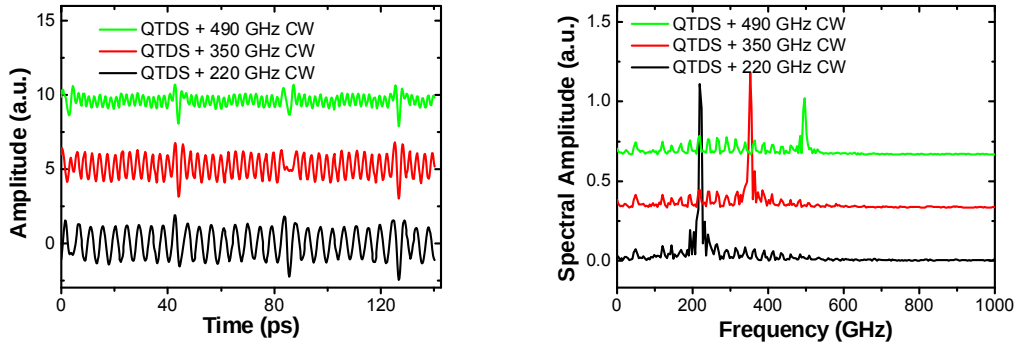


**Figure 70: Hybrid time domain and frequency domain signals for different cw frequencies.**

To demonstrate the advantages of the improved hybrid approach, we placed a 6 mm slab of glass ($SiO_2$) in the THz beam focus. A stand-alone continuous wave THz spectrometer would by far not be able to resolve the thickness, as the induced phase shift is more than one sine period (see Figure 71a). With the additional information gained by the QTDS signal, one can use either the ancillary time-domain or spectral information to solve this problem.

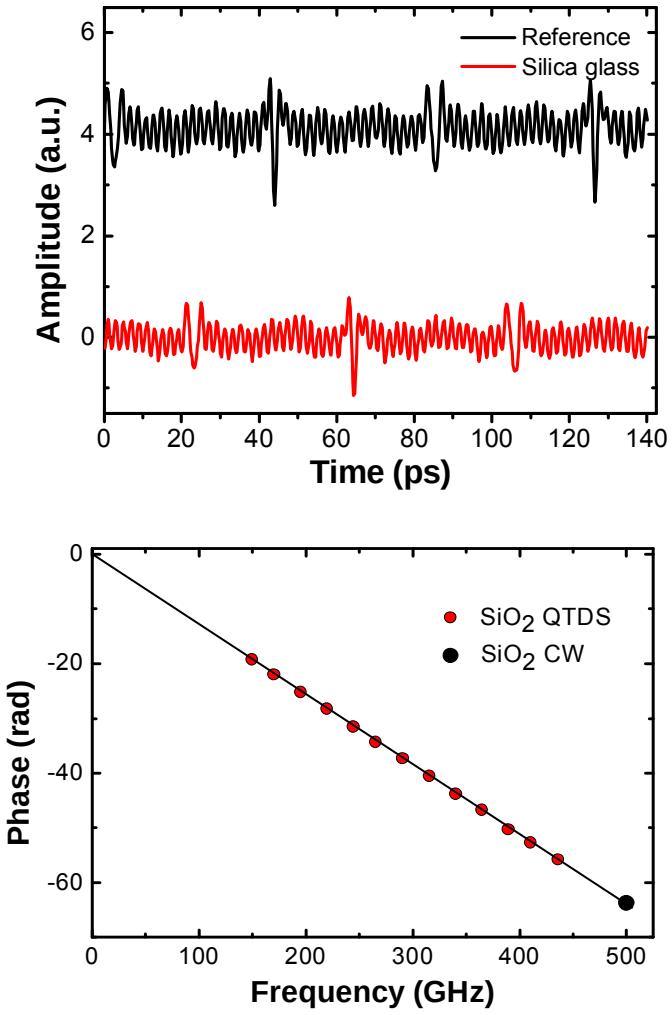


**Figure 71: Hybrid approach to determine the absolute phase delay for thickness measurements [6].**

In the measured time trace, the absolute shift of the QTDS pulses can be easily extracted, but this information contains an average value across all frequency components within the QTDS THz pulse. For a more precise determination due to the higher signal to noise ratio of the CW system, one can combine the 2π affected CW phase information with the phase delay measured with the QTDS diode. By subtracting the nearest smaller number of CW periods (modulo-function) from the extracted QTDS shift and adding the highly accurate CW phase shift (still affected by the 2π ambiguity); one can calculate the exact thickness $D_{cw}$ at the CW frequency (see formula (5.8)).

$$D_{cw} = \frac{\left|\Delta\varphi_{total,cw}\right|}{2\pi} \cdot \frac{c}{(n_{cw} - n_{air})} \cdot \frac{1}{f_{cw}} \tag{5.8}$$

$$\left|\Delta\varphi_{total,cw}\right| = \left|2\pi\, mod(T_p \cdot f_{cw})\right| + \left|\Delta\varphi_{cw}\right|. \tag{5.9}$$

The glass sample was measured with a micrometer to 6.25 mm and the findings agree very well with the thickness determined with the hybrid system.

Instead of using the pulse peaks to determine the time delay, one can also evaluate the containing phase shift of each individual QTDS frequency component. This approach is only valid for low dispersive samples, because then the induced phase shift scales linear with frequency. A line of best fit can be drawn through the origin and the discrete phase shifts of each comb frequency. That allows for a precise determination of the total phase shift $\varphi_{\text{total,cw}}$ of the CW signal (see Figure 71b).

This novel hybrid approach can be added to existing continuous wave THz spectrometer with ease to render them able to determine thicknesses of the sample under investigation with one measurement. The extra components (a dichroic mirror and a multimode laser diode) are off-the-shelf products with small costs compared to the original investment for the temperature stabilized CW system.

## 5.5 Twin QTDS System

Quasi time-domain spectrometers have proven to be a cost effective alternative to standard TDS systems for many applications. The possibility to guide more than one optical laser beam on the same emitter and receiver antennas holds a great potential for custom THz solutions. Like the novel hybrid CW system presented in the last subchapter, one can also imaging to upgrade a QTDS system with another multimode laser diode. This holds the advantage of employing laser diodes with different mode spacing, or the opportunity to have tunable mixing products between the two laser diodes, just like a CW system mixing two single frequencies from separate lasers. This concept will be elucidated in this chapter. Next to the fundamental principle, some time and frequency traces of dual QTDS spectrometers are shown.

For a dual or twin QTDS system it is now necessary to ensure mixing between the two laser modes. Therefore they have to be incident in the same polarization on the two semiconductor antennas and the center frequency spacing should be well within the antenna characteristics to achieve sufficient output power levels for the new mixing products. Both beams are overlapped through a beam splitter and guided to the photoconductive antennas (see Figure 72). Note that the incident optical power of both laser diodes had to be reduced by grey wedges to prevent thermal failure of the antenna structures. On each photoconductive antenna were about 36 mW optical power present, 18 mW from each QTDs laser diode.

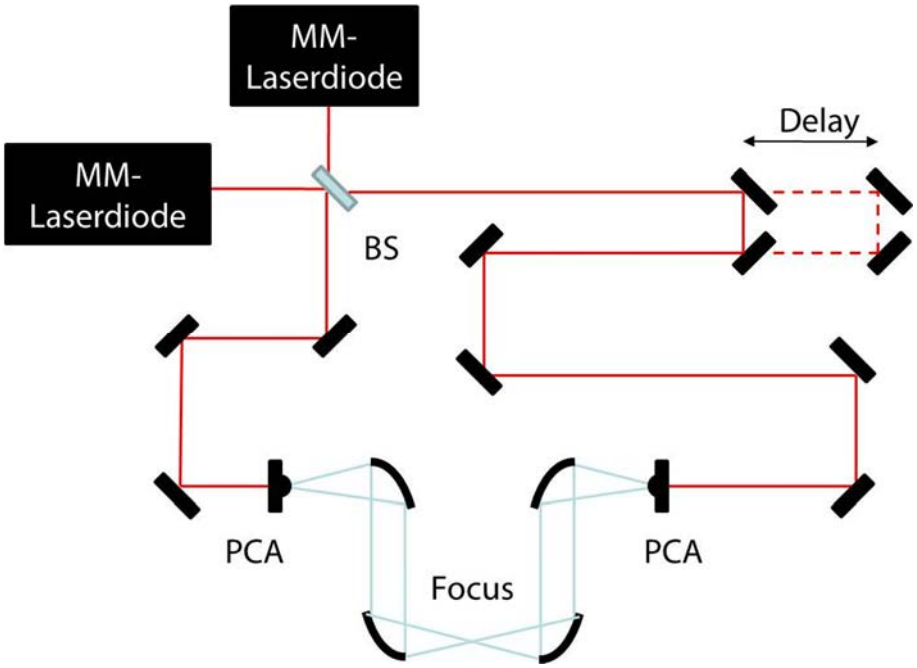


**Figure 72: Schematic of a twin QTDS setup.**

For a first test spectrometer two different kinds of knob laser diode modules were chosen. Overlapping these two laser beams results in a THz spectrum which inhibits both pulse trains (cf. Figure 73). Like in the previous setup, the first diode had a cavity mode spacing of approx. 25 GHz (smaller signal - 40 ps spacing), whereas the second diode had a longer resonator and therefore a shorter frequency spacing (16.7 GHz – 60 ps pulse spacing).

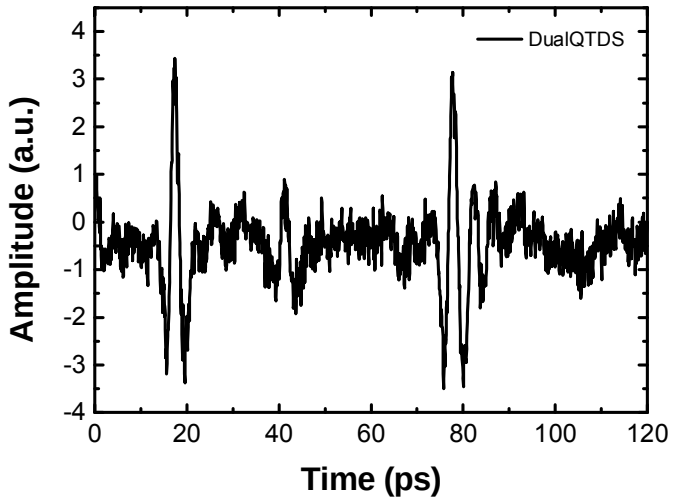


**Figure 73: Dual QTDS time trace with different cavity mode spacing.**

Unfortunately, the center frequencies were in the range of 3 THz and hence too far apart for intermediate mixing products appearing in the frequency spectrum (see Figure 74).

The spectrum contains also many features due to the different mode spacing of each laser diode and the resulting multiples thereof.

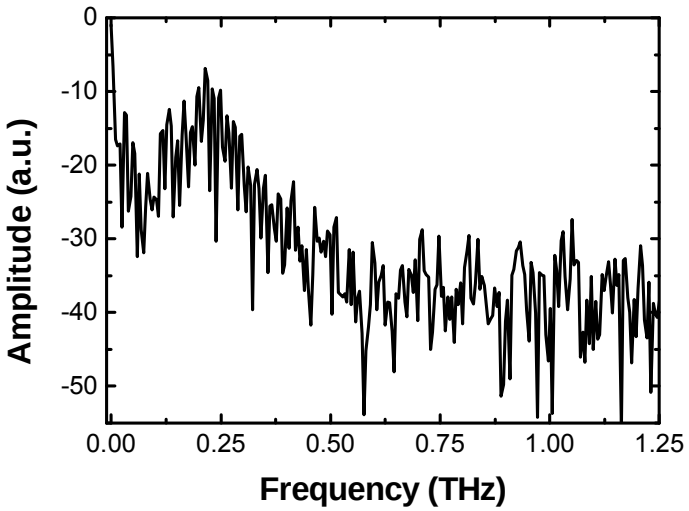


**Figure 74: Frequency spectrum of dual QTDS system with different cavity mode spacing.**

Selecting a well chosen laser diode with a center frequency spacing of around 1.2 THz allows for generating mixing products between both laser diodes. A similar laser diode to the first one was chosen and the two beams merged through a beam splitter. Both diodes have a cavity mode spacing of 25 GHz and therefore the pulses are lying exactly on top of each other in the time trace. This is due to the fact, that the optical beams share the same path length in both arms to the detector antenna, and thus have the same $\Delta L$ induced by the delay stage. A time trace of the resulting signal can be seen in Figure 75.

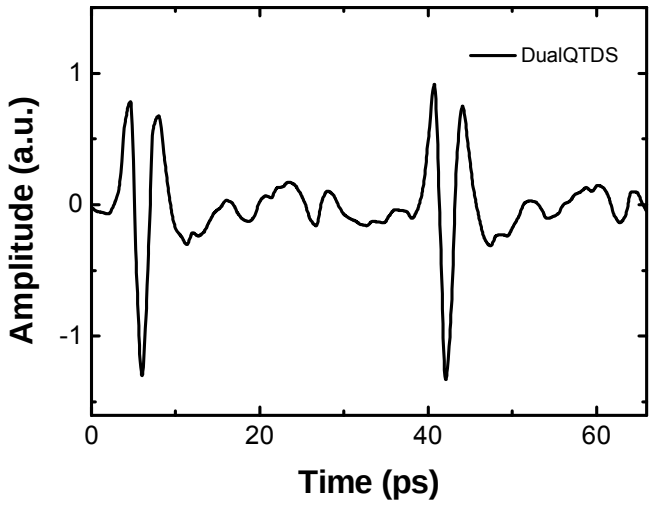


**Figure 75: Dual QTDS time trace with equal cavity mode spacing.**

Transforming the time signal into the frequency domain reveals the desired new mixing components above 1 THz. Photomixing products from each laser diode with its own modes form the spectrum up to 750 GHz but around 1.2 THz new frequency mixing products evolve (see Figure 76).

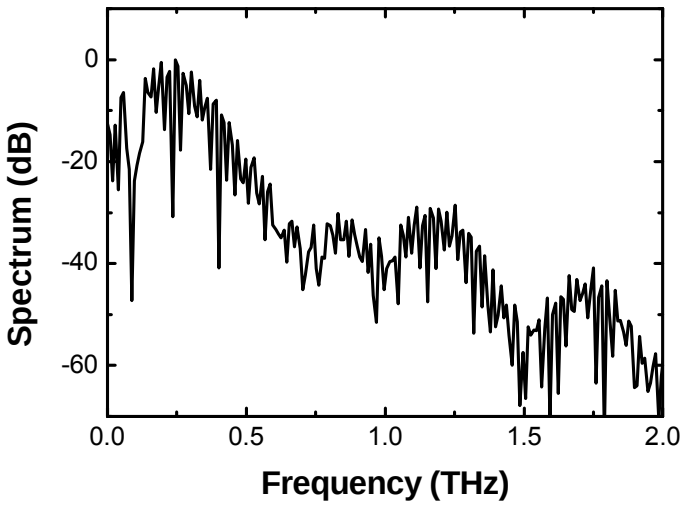


**Figure 76: Dual QTDS time trace with equal cavity mode spacing.**

The fundamental mode spacing of 25 GHz still remains present in those higher frequency THz modes but due to the lower efficiency of the antennas at higher frequencies the resulting THz power remains lower.

## 5.6 Conclusions

In this chapter the applicability of quasi time-domain spectrometers (QTDS) for real world applications were analyzed. After going into the mathematics behind the generation and detection process of QTDS systems, the imaging capability of standard QTDS systems has been elicited. Novel hybrid and dual QTDS spectrometer designs have been presented. The hybrid spectrometer setup consisting of a standard continuous wave THz spectrometer and a QTDS laser diode was discussed, allowing for obtaining the material parameters of the sample under investigation as well as its thickness at the same time. Thus, this new system approach offers a cost effective and easy solution to upgrade existing CW THz spectrometers.

Incorporating a second multimode laser diode in a standard QTDS setup opens the possibility to access even higher mixing frequencies than those of just one multimode laser diode. Two different additional diodes with 16.6 GHz and 25 GHz mode spacing were integrated in a QTDS spectrometer and the measured time traces and frequency spectra were presented. This approach allows for an effective way to extend the frequency range of common QTDS systems and enables customization of the system to a plethora of applications.

Quasi time domain spectrometers will provide the basis for first cost effective mass market THz products and sensing solutions. In the years ahead this ingenious concept will be subject to further investigations.

# 6 Summary

So far terahertz (THz) technology, targeting frequencies between 0.1and10 THz, was foremost used for laboratory based material science experiments, but it is now on the verge of transitioning into real world sensing applications. For this step to further succeed, sophisticated THz generation and detection methods as well as THz beam guiding schemes are necessary. This work contributes to the field of THz technology by simulating, fabricating and analyzing novel THz filter designs and THz fibers as waveguides. The revolutionary QTDS spectrometer approach is further extended and its ability to drive future flexible and mobile THz sensor systems is verified.

In the first result chapter of the thesis, a novel THz waveguide design with additive polymer is presented, supporting higher mode confinement and the ability to eliminate higher order modes from propagating. The fiber was analyzed in a customized dynamic aperture near-field setup, based on standard THz time domain spectrometer. Modulating the optical excitation allows sub-wavelength spatial resolution for the mode profile imaging. This enables the detection of multimode behavior and leads to the verification of cut-off frequencies in these waveguides. Mode profile images of different THz fiber waveguides have been presented and analyzed. This improvement may not only be relevant for new applications in near-field micro-spectroscopy but also for offering higher THz electrical field intensities in a bendable waveguide.

As a second result the fiber drawing method was adapted to fabricate first prototypes of polymer based THz photonic crystal filters. This bandgap filter design was simulated and optimized by a semi-analytical modeling software method (GMT). Their frequency response and the correlation between simulation and fabrication were measured by standard transmission THz TDS and angle dependent measurement to verify the frequency characteristics.

In the last chapter quasi time domain spectrometers (QTDS) build around cost effective multimode laser diodes are presented in different system configurations. The applicability of this technique was demonstrated for THz imaging purposes. Because of the pulsed time-domain waveform, different analyzing methods such as time of flight and peak-to-peak, known from conventional TDS, can be applied. Furthermore a hybrid continuous wave THz system was presented. This novel system overcomes the $2\pi$ uncertainty of regular CW THz spectrometers, enabling thickness determination by analyzing the QTDS time trace. Combining two multimode laser diodes to form a dual QTDS approach was set up and time and frequency domain signals are shown to underline the new advantages with such a tunable system. The proposed systems performance already allows for a broad field of applications and will be another step towards compact and mobile THz sensor systems in the near future.

# References


1. M. Stecher, et al., *Point-by-Point Written Sampled Fiber Bragg Gratings*. in *Australian Conference on Optical Fibre Technology (ACOFT)* 2009: Adelaide, Australia.

2. M. Stecher, et al., *Periodic refractive index modifications inscribed in polymer optical fibre by focussed IR femtosecond pulses*. in *18th International Conference on Plastic Optical Fibers (POF)* 2009: Sydney, Australia.

3. Stecher, M., et al., *Mode profiling of THz fibers with dynamic aperture near-field imaging*, in *Infrared Millimeter and Terahertz Waves (IRMMW-THz). 2011 36th International Conference on* 2011: Houston, Texas.

4. Scheller, M., and M. Koch, *Terahertz quasi time domain spectroscopy*. Opt. Express. 2009. **17**(20): p. 17723-17733.

5. Stecher, M., M. Scheller, and M. Koch. *Hybrid continuous wave terahertz system* in *Infrared Millimeter and Terahertz Waves (IRMMW-THz). 2010 35th International Conference on* 2010.

6. Scheller, M., et al., *Hybrid continuous wave terahertz spectroscopy*. Opt. Express. 2010. **18**(15): p. 15887-15892.

7. Scheller, M., et al., *Terahertz quasi-time-domain spectroscopy imaging*. Appl. Opt. 2011. **50**(13): p. 1884-1888.

8. Auston, D.H., K.P. Cheung, and P.R. Smith, *Picosecond photoconducting Hertzian dipoles.* Applied Physics Letters. 1984. **45**(3): p. 284-286.

9. Hu, B.B. and M.C. Nuss, *Imaging with terahertz waves.* Opt. Lett., 1995. **20**(16): p. 1716-1718.

10. Krumbholz, N., et al., *Monitoring polymeric compounding processes inline with THz time-domain spectroscopy*. Polymer Testing. 2009. **28**(1): p. 30-35.

11. Vieweg, N., et al., *Fiber-coupled THz spectroscopy for monitoring polymeric compounding processes*. Vol. 6616. 2007: SPIE. 66163M.

12. Ung, B.S.Y., et al., *Towards quality control of food using terahertz.* BioMEMS and Nanotechnology III (2007: ACT, Australia). 2007.

13. Jördens, C. and M. Koch, *Detection of foreign bodies in chocolate with pulsed terahertz spectroscopy*. Vol. 47. 2008: SPIE. 037003.

14. Krumbholz, N., et al., *Handheld terahertz spectrometer for the detection of liquid explosives.* Vol. 7485. 2009: SPIE. 748504.

15. Brown, E.R., et al., *Photomixing up to 3.8 THz in low-temperature-grown GaAs.* Vol. 66. 1995: AIP. 285-287.

16. Matsuura, S., M. Tani, and K. Sakai, *Generation of coherent terahertz radiation by photomixing in dipole photoconductive antennas.* Vol. 70. 1997: AIP. 559-561.

17. Jepsen, P.U., R.H. Jacobsen, and S.R. Keiding, *Generation and detection of terahertz pulses from biased semiconductor antennas.* J. Opt. Soc. Am. B, 1996: **13**(11): p. 2424-2436.

18. Mendis, R., et al., *Tunable CW-THz system with a log-periodic photoconductive emitter.* Solid-State Electronics. **48**(10-11): p. 2041-2045.

19. Krumbholz, N., *Fasergekoppelte Terahertz-Zeitbereichspektrometer: Entwicklung und Anwendung.* 2010. Technische Universität Braunschweig: Göttingen.

20. Jacobsen, R.H., et al., *Interpretation of photocurrent correlation measurements used for ultrafast photoconductive switch characterization.* Journal of Applied Physics. 1996. **79**(5): p. 2649-2657.

21. Sartorius, B., et al., *All-fiber terahertz time-domain spectrometer operating at 1.5 μm telecom wavelengths.* Opt. Express, 2008. **16**(13): p. 9565-9570.

22. Koester, C.J. and E. Snitzer, *Amplification in a Fiber Laser.* Appl. Opt., 1964. **3**(10): p. 1182-1186.

23. Paschotta, R., et al., *Passively Q-switched 0.1-mJ fiber laser system at 1.53 μm.* Opt. Lett., 1999. **24**(6): p. 388-390.

24. Rafal, W., et al. *THz Time-Domain Spectrometer Based on LT-InGaAs Photoconductive Antennas Exited by a 1.55 μm Fibre Laser*. 2007. Optical Society of America.

25. Roman, J.D., et al. *Mesa-Structured InGaAs/InAlAs Photoconductive Antennas for THz Time Domain Systems Operated at 1.5 μm*. 2010. Optical Society of America.

26. Roehle, H., et al., *Next generation 1.5 μm terahertz antennas: mesa-structuring of InGaAs/InAlAs photoconductive layers.* Opt. Express, 2010. **18**(3): p. 2296-2301.

27. Benjamin, W., et al. *Terahertz Quantum Cascade Lasers*. 2007. Optical Society of America.

28. Walther, C., et al., *Low frequency terahertz quantum cascade laser operating from 1.6 to 1.8 THz*. Vol. 89. 2006: AIP. 231121.

29. Eisele, H., M. Naftaly, and R. Kamoua, *Generation of Submillimeter-Wave Radiation with GaAs Tunnel Diodes and InP Gunn Devices in a Second or Higher Harmonic Mode.* International Journal of Infrared and Millimeter Waves, 2005. **26**(1): p. 1-14.

30. Jae-Sung, R., et al., *SiGe heterojunction bipolar transistors and circuits toward terahertz communication applications.* Microwave Theory and Techniques, IEEE Transactions on, 2004. **52**(10): p. 2390-2408.

31. Nakajima, F., T. Furuta, and H. Ito, *High-power continuous-terahertz-wave generation using resonant-antenna-integrated uni-travelling-carrier photodiode.* Electronics Letters, 2004. **40**(20): p. 1297-1298.

32. Teich, M.C., *FIELD-THEORETICAL TREATMENT OF PHOTOMIXING.* Applied Physics Letters, 1969. **14**(6): p. 201-203.

33. McIntosh, K.A., et al., *Terahertz photomixing with diode lasers in low-temperature-grown GaAs*. Vol. 67. 1995: AIP. 3844-3846.

34. Rafal, W., *Switchable THz Reflectors*, 2007, TU Braunschweig: Braunschweig.

35. Tonouchi, M., *Cutting-edge terahertz technology.* Nat Photon, 2007. **1**(2): p. 97-105.

36. Kübler, C., et al., *Coherent Structural Dynamics and Electronic Correlations during an Ultrafast Insulator-to-Metal Phase Transition in VO2.* Physical Review Letters, 2007. **99**(11): p. 116401.

37. He, Y., et al., *Protein Dynamical Transition Does Not Require Protein Structure.* Physical Review Letters, 2008. **101**(17): p. 178103.

38. McGowan, R.W., G. Gallot, and D. Grischkowsky, *Propagation of ultrawideband short pulses of terahertz radiation through submillimeter-diameter circular waveguides.* Opt. Lett., 1999. **24**(20): p. 1431-1433.

39. Gallot, G., et al., *Terahertz waveguides.* J. Opt. Soc. Am. B, 2000. **17**(5): p. 851-863.

40. Mendis, R. and D. Grischkowsky, *Plastic ribbon THz waveguides*. Vol. 88. 2000: AIP. 4449-4451.

41. Mendis, R. and D. Grischkowsky, *THz interconnect with low-loss and low-group velocity dispersion.* Microwave and Wireless Components Letters, IEEE, 2001. **11**(11): p. 444-446.

42. Wang, K. and D.M. Mittleman, *Metal wires for terahertz wave guiding.* Nature, 2004. **432**(7015): p. 376-379.

43. Chen, L.-J., et al., *Low-loss subwavelength plastic fiber for terahertz waveguiding.* Opt. Lett., 2006. **31**(3): p. 308-310.

44. Nagel, M., A. Marchewka, and H. Kurz, *Low-index discontinuity terahertz waveguides.* Opt. Express, 2006. **14**(21): p. 9944-9954.

45. Atakaramians, S., et al., *Porous fibers: a novel approach to low loss THz waveguides.* Opt. Express, 2008. **16**(12): p. 8845-8854.

46. Nielsen, K., et al., *Bendable, low-loss Topas fibers for the terahertz frequency range.* Opt. Express, 2009. **17**(10): p. 8592-8601.

47. Atakaramians, S., et al., *Low loss, low dispersion and highly birefringent terahertz porous fibers.* Optics Communications, 2009. **282**(1): p. 36-38.

48. Hassani, A., A. Dupuis, and M. Skorobogatiy, *Porous polymer fibers for low-loss Terahertz guiding.* Opt. Express, 2008. **16**(9): p. 6340-6351.

49. Han, H., et al., *Terahertz pulse propagation in a plastic photonic crystal fiber*. Vol. 80. 2002: AIP. 2634-2636.

50. Birks, T.A., J.C. Knight, and P.S.J. Russell, *Endlessly single-mode photonic crystal fiber.* Opt. Lett., 1997. **22**(13): p. 961-963.

51. Ferrando, A., et al., *Nearly zero ultraflattened dispersion in photonic crystal fibers.* Opt. Lett., 2000. **25**(11): p. 790-792.

52. JIN, et al., *Terahertz dielectric properties of polymers*. Vol. 49. 2006, Seoul, Coree, Republique de: Korean Physical Society. 5.

53. Scherger, B., et al., *Terahertz lenses made by compression molding of micropowders.* Appl. Opt., 2011. **50**(15): p. 2256-2262.

54. Wietzke, S., *Terahertz-Zeitbereichspektroskopie: zerstörungsfreies Messverfahren zur Polymeranalytik und Kunststoffbauteilprüfung*, 2011, Technische Universität Braunschweig: Aachen.

55. Russell, P., *Photonic Crystal Fibers.* Science, 2003. **299**(5605): p. 358-362.

56. van Eijkelenborg, M., et al., *Microstructured polymer optical fibre.* Opt. Express, 2001. **9**(7): p. 319-327.

57. Nielsen, K., *Polymer fiber waveguides for terahertz radiation*, in *DTU Fotonik* 2010, Danish Technical University: Copenhagen.

58. COMSOL, *COMSOL Multiphysics User's Guide*, 2006.

59. Mortensen, N.A., et al., *Modal cutoff and the V parameter in photonic crystal fibers.* Opt. Lett., 2003. **28**(20): p. 1879-1881.

60. Koshiba, M. and K. Saitoh, *Applicability of classical optical fiber theories to holey fibers.* Opt. Lett., 2004. **29**(15): p. 1739-1741.

61. Golosovsky, M. and D. Davidov, *Novel millimeter-wave near-field resistivity microscope*. Vol. 68. 1996: AIP. 1579-1581.

62. Durig, U., D. Pohl, and F. Rohner, *Near-field optical scanning microscopy with tunnel-distance regulation.* IBM Journal of Research and Development, 1986. **30**(5): p. 478-483.

63. Paesler, M.A. and P.J. Moyer, *Near-field optics: Theory, instrumentation, and applications* 1996, New York: Wiley.

64. Ash, E.A. and G. Nicholls, *Super-resolution Aperture Scanning Microscope.* Nature, 1972. **237**(5357): p. 510-512.

65. Hunsche, S., et al., *THz near-field imaging.* Optics Communications, 1998. **150**(1-6): p. 22-26.

66. Chen, Q., et al., *Near-field terahertz imaging with a dynamic aperture.* Opt. Lett., 2000. **25**(15): p. 1122-1124.

67. Simon M. Sze and K.K. Ng, *Physics of Semiconductor Devices* 1981, New York: John Wiley and Sons.

68. Jepsen, P.U., *Generation and Applications of THz radiation*, in *Dept. of Chemistry* 1996, Aarhus University: Aarhus, Denmark.

69. Ioffe. *Electronic archive. New Semiconductor Materials. Characteristics and Properties*. Available from: http://www.ioffe.ru/SVA/NSM/.

70. Grischkowsky, D., et al., *Far-infrared time-domain spectroscopy with terahertz beams of dielectrics and semiconductors.* J. Opt. Soc. Am. B, 1990. **7**(10): p. 2006-2015.

71. Bitzer, A., A. Ortner, and M. Walther, *Terahertz near-field microscopy with subwavelength spatial resolution based on photoconductive antennas.* Appl. Opt., 2010. **49**(19): p. E1-E6.

72. Valk, N.C.J.v.d. and P.C.M. Planken, *Electro-optic detection of subwavelength terahertz spot sizes in the near field of a metal tip*. Vol. 81. 2002: AIP. 1558-1560.

73. Duling, I. and D. Zimdars, *Terahertz imaging: Revealing hidden defects.* Nat Photon, 2009. **3**(11): p. 630-632.

74. Wilmink, G.J., et al., *Development of a compact terahertz time-domain spectrometer for the measurement of the optical properties of biological tissues.* Vol. 16. 2011: SPIE. 047006.

75. Winnewisser, C., et al., *Transmission Features of Frequency-Selective Components in the Far Infrared Determined by Terahertz Time-Domain Spectroscopy.* Appl. Opt., 1999. **38**(18): p. 3961-3967.

76. Turchinovich, D., et al., *Flexible all-plastic mirrors for the THz range.* Applied Physics A: Materials Science & Processing, 2002. **74**(2): p. 291-293.

77. Kleine-Ostmann, T., et al., *Room-temperature operation of an electrically driven terahertz modulator.* Applied Physics Letters, 2004. **84**(18): p. 3555-3557.

78. Winnewisser, C., F. Lewen, and H. Helm, *Transmission characteristics of dichroic filters measured by THz time-domain spectroscopy.* Applied Physics A: Materials Science & Processing, 1998. **66**(6): p. 593-598.

79. Ulrich, R., *Far-infrared properties of metallic mesh and its complementary structure.* Infrared Physics, 1967. **7**(1): p. 37-55.

80. Timusk, T. and P.L. Richards, *Near millimeter wave bandpass filters.* Appl. Opt., 1981. **20**(8): p. 1355-1360.

81. Tomaselli, V.P., et al., *Far-infrared bandpass filters from cross-shaped grids.* Appl. Opt., 1981. **20**(8): p. 1361-1366.

82. Bozzi, M., et al., *Design, fabrication, and measurement of frequency-selective surfaces*. Vol. 39. 2000: SPIE. 2263-2269.

83. Gourley, P.L., et al., *Optical properties of two-dimensional photonic lattices fabricated as honeycomb nanostructures in compound semiconductors.* Applied Physics Letters, 1994. **64**(6): p. 687-689.

84. Bullock, D.L., C.-C. Shih, and R.S. Margulies, *Photonic band structure investigation of two-dimensional Bragg reflector mirrors for semiconductor laser mode control.* J. Opt. Soc. Am. B, 1993. **10**(2): p. 399-403.

85. Tocci, M.D., et al., *Measurement of spontaneous-emission enhancement near the one-dimensional photonic band edge of semiconductor heterostructures.* Physical Review A, 1996. **53**(4): p. 2799.

86. Chelnokov, A., et al., *An optical drill for the fabrication of photonic crystals.* Journal of Optics A: Pure and Applied Optics, 1999. **1**(5): p. L3.

87. Özbay, E., et al., *Laser-micromachined millimeter-wave photonic band-gap cavity structures*. Vol. 67. 1995: AIP. 1969-1971.

88. Wanke, M.C., et al., *Laser Rapid Prototyping of Photonic Band-Gap Microstructures.* Science, 1997. **275**(5304): p. 1284-1286.

89. Ohtaka, K., et al., *Photonic band effects in a two-dimensional array of dielectric spheres in the millimeter-wave region.* Physical Review B, 2000. **61**(8): p. 5267.

90. Ludwig, A.C., *The generalized multipole technique.* Computer Physics Communications, 1991. **68**(1-3): p. 306-314.

91. Hafner, C., *Multiple multipole program computation of periodic structures.* J. Opt. Soc. Am. A, 1995. **12**(5): p. 1057-1067.

92. Kashyap, R., *Fiber bragg gratings,* 1999: Academic Pr.

93. Ahmadi-Boroujeni, M., *Analysis of 2D Photonic Crystals by the Generalized Multipole Technique (GMT)* 2011, Philipps-Universität: Marburg.

94. Ahmadi-Boroujeni, M. and M. Shahabadi, *Application of the generalized multipole technique to the analysis of a ladder parallel-plate waveguide for terahertz guided-wave applications.* J. Opt. Soc. Am. B, 2010. **27**(10): p. 2061-2067.

95. Vieweg, N., *Eigenschaften und Anwendungen von Flüssigkristallen im Terahertzfrequenzbereich* 2011, Göttingen: Cuvillier.

96. Ferguson, B. and X.-C. Zhang, *Materials for terahertz science and technology.* Nat Mater, 2002. **1**(1): p. 26-33.

97. Wietzke, S., et al., *Terahertz time-domain spectroscopy as a tool to monitor the glass transition in polymers.* Opt. Express, 2009. **17**(21): p. 19006-19014.

98. Koch, M., et al., *THz-imaging: a new method for density mapping of wood.* Wood Science and Technology, 1998. **32**(6): p. 421-427.

99. Shibuya, K., et al., *Compact and inexpensive continuous-wave subterahertz imaging system with a fiber-coupled multimode laser diode.* Vol. 90. 2007: AIP. 161127.

100. Scheller, M., C. Jansen, and M. Koch, *Analyzing sub-100-μm samples with transmission terahertz time domain spectroscopy.* Optics Communications, 2009. **282**(7): p. 1304-1306.

101. Butz, T., *Fouriertransformation für Fussgänger* 2005: Vieweg+ Teubner.

102. Mittleman, D.M., et al., *Gas sensing using terahertz time-domain spectroscopy.* Applied Physics B: Lasers and Optics, 1998. **67**(3): p. 379-390.

103. Dorney, T.D., R.G. Baraniuk, and D.M. Mittleman, *Material parameter estimation with terahertz time-domain spectroscopy.* J. Opt. Soc. Am. A, 2001. **18**(7): p. 1562-1571.

104. Duvillaret, L., F. Garet, and J.-L. Coutaz, *Highly Precise Determination of Optical Constants and Sample Thickness in Terahertz Time-Domain Spectroscopy.* Appl. Opt., 1999. **38**(2): p. 409-415.

105. Wang, X., L. Hou, and Y. Zhang, *Continuous-wave terahertz interferometry with multiwavelength phase unwrapping.* Appl. Opt., 2010. **49**(27): p. 5095-5102.

106. Scheller, M., K. Baaske, and M. Koch, *Multifrequency continuous wave terahertz spectroscopy for absolute thickness determination*. Vol. 96. 2010: AIP. 151112.

# List of Publications

## Original Journal Papers

- "Terahertz quasi-time-domain spectroscopy imaging"
  M. Scheller, S.F. Dürrschmidt, M. Stecher and M. Koch
  Appl. Opt., OSA, 2011, 50(13), pp. 1884-1888

  Personal contribution:
  Together with the first author the QTDS system was setup and measurements were taken. I assisted in writing and proofreading of the manuscript.

- "Hybrid Continuous Wave Terahertz Spectroscopy"
  M. Scheller, M. Stecher, M. Gerhard and M. Koch
  Optics Express, 2010, 18(15), pp. 15887-15892

  Personal contribution:
  A continuous-wave THz spectrometer was setup up and combined with a multimode laser diode in cooperation with the first author. Adjustments and measurements were recorded and analyzed together. I contributed part of the result graphs and assisted writing and correcting the paper.

## Conference Contributions

- "Mode profiling of THz fibers with dynamic aperture near-field imaging"
  Matthias Stecher, Stefan F. Dürrschmidt, Kristian Nielsen, Alessio Stefani, Henrik K. Rasmussen, Peter Uhd Jepsen, Graham E. Town, Ole Bang, and Martin Koch
  36th IRMMW/THz
  Houston, United States, October 2011

- "Discrete sampling of continuous wave terahertz radiation"
  M. Schwerdtfeger, M. Scheller, M. Stecher and M. Koch
  35th IRMMW/THz
  Rome, Italy, September 2010

  Personal contribution:
  I assisted with setting up the THz system and the measurement acquisition.

- "Hybrid continuous wave terahertz system"
  M. Stecher, M. Scheller and M. Koch
  35th IRMMW/THz
  Rome, Italy, September 2010

- "Making THz systems industry compatible"
  M. Koch, M. Scheller, M. Schwerdtfeger, M. Stecher, O. Peters, B. Scherger, B. Heinen, S. Wietzke, T. Hochrein, N. Vieweg, C. Jördens, N. Krumbholz, and C. Jansen
  20th Intern. Conf. on Applied Electromagnetics and Communications
  Dubrovnik, Croatia, September 2010 (invited)

  Personal contribution:
  Parts of my project work of assembling a semi-mobile THz TDS system to determine the water status of plants have been presented at this conference.

- "Periodic refractive index modifications inscribed in polymer optical fibre by focussed IR femtosecond pulses"
  M. Stecher, R.J. Williams, O. Bang, G.D. Marshall, M.J. Withford and G.E. Town
  18th International Conference on Plastic Optical Fibers (POF)
  Sydney, Australia, 2009

- "Point-by-Point Written Sampled Fiber Bragg Gratings"
  M. Stecher, R.J. Williams, G.D. Marshall, M.J. Withford and G.E. Town
  Australian Conference on Optical Fibre Technology (ACOFT)
  Adelaide, Australia, 2009

Due to copyright laws, the following articles have been omitted from this thesis.

Please refer to the list of publications for more details.